CHAPTER V

Fracture Toughness and 3D Characterization of 4330 Steel

The need for 3D microstructural data that serves as input for models that predict macro-structural material properties motivates the development of new tomographic techniques. Using the newly developed FSLSS technique, multiple 3D steel microstructure volume elements have been sampled, for characterization of the size and spatial distribution of titanium nitride (TiN) particles. In this chapter, the influence of the size and distribution of TiN particles on fracture toughness is assessed using a methodology incorporating statistical volume elements (SVE). First, a overview of the toughness models and the role of precipitates in steel is given.

5.1 Precipitates in Steel

Precipitates in steels have been shown to be both beneficial and detrimental to toughness. Tempering of some steels can produce sub-micron precipitates that strengthen the material by obstructing dislocation motion (precipitation strengthening or hardening) [132]. At these small length scale precipitates can also nucleate micro-voids at large strains [17]. Larger precipitates generally are detrimental by serving as void nucleators at low strains [17]. Two populations of precipitates exist in

the 4330 titanium modified steel investigated. The fine-scale population of titanium carbides (TiC) have a mean size of 0.1 µm and range in size from 0.1-0.5 µm [133]. This size range is below the resolution limit of the current open-atmosphere FSLSS technique. These precipitates mostly contribute to Hall-Petch type grain boundary strengthening and precipitation strengthening, and are formed during the low temperature heat treatment after a solutionizing quench.

The larger sized population of precipitates, titanium nitride (TiN), form by precipitation from solution during the initial casting of the ingot, and can be fractured during subsequent forging steps. Statistical parameters and 3D reconstructions characterizing TiN particles were collected using the FSLSS technique. A set of three orthogonal 2-D optical images has been assembled in Figure 5.1 to schematically show the approximate size and distribution of the TiN particles. These cuboidal TiN precipitates serve as locations for void nucleation by debonding or particle fracture in high strain events.

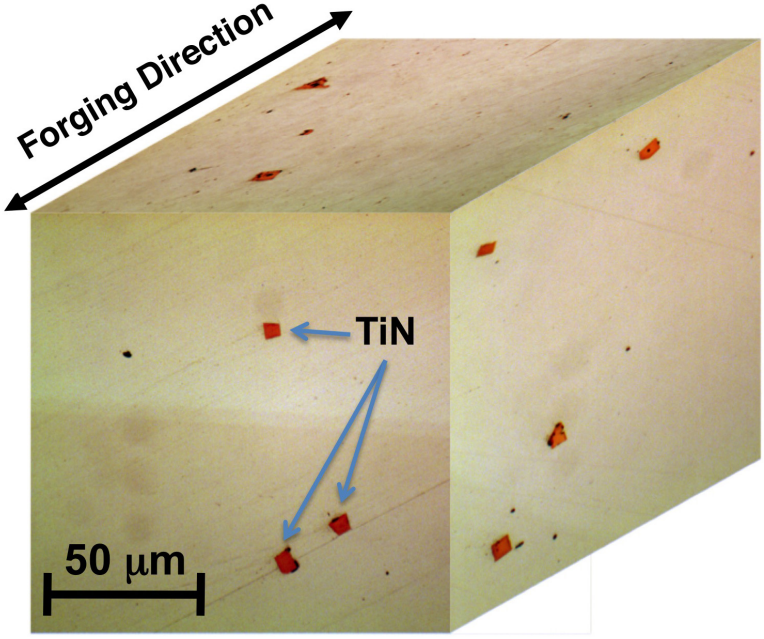

Figure 5.1: 3D block assembled schematically from optical micrographs imaged from three orthogonal surfaces of titanium modified 4330 steel. TiN inclusions appear red due to absorption contrast and are indicated with arrows.

5.2 Structure Property Modeling

An extensive body of literature has addressed the role of different oxide, carbide, and nitride precipitates, voids, and precipitate-matrix interactions in the process zone near crack tips and their influence on crack propagation and fracture toughness. Toughness models incorporate various statistical measures of void and particle geometry and dispersion, extracted by either 2D or 3D approaches, as well as particle-matrix bonding energy. Using the fracture toughness models combined with the statistical parameters available from the FSLSS experiments, a method for analyzing and improving toughness and variability of this property in UHS steels has been developed.

In the path of a crack, the energy required for propagation is lowered significantly by the existence of particles that nucleate voids and by the subsequent coalescence of voids. The reduction in area associated with high densities of voids in the crack

path as well as stress concentrations associated with their presence are important considerations for property modeling. Most engineering materials have defects present such as precipitates or inclusions phases, which have been shown to nucleate voids during loading, as discussed previously in section 2.2.2.

Voids have been shown to nucleate by debonding or cracking of second-phase particles in numerous experimental studies for materials such as: aluminum alloys, cementite in steels, sulfides, as well as nitrides, carbides, and other steel inclusions [18, 72, 134–136]. In ductile fracture, where a crack is propagating through material elements containing inclusion particles, a three step process exists in which voids are generated. These steps include [137]:

- Formation of free interfaces between inclusion particles and the matrix formed by debonding or particle fracture during plastic deformation
- Continued plastic deformation, resulting in void growth near the cracks, or enhanced debonding by hydrostatic stresses
- Shear instabilities between voids, leading to micro-void coalescence and eventually fracture

Often, these steps occur nearly simultaneously, depending on factors such as the size of the inclusions, the proximity to heightened stress fields, and localized plasticity effects. For instance, new voids can nucleate in one population of particles, while growth continues at prior nucleation sites. The rate limiting step in ductile fracture for materials with distributed inclusion particles is typically either (1) the nucleation of voids - particularly for materials with strongly bonded second phase particles, or (2) growth and coalescence - for materials that easily nucleate voids.

The sequence of events that occurs during ductile fracture of a high strength steel is schematically shown in Figure 5.2 [138], where two populations of interacting

inclusion particles exist. For a ultra high strength 4330 steel, these particles are sub-micron Ti(C,N) particles and the larger cuboidal TiN particles.

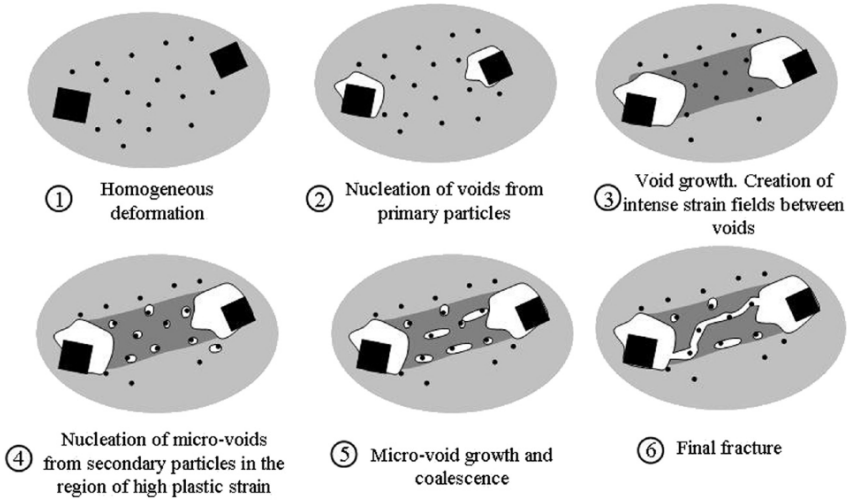

Figure 5.2: Schematic of ductile fracture and the formation of voids at primary and secondary inclusion particles with increasing strain in a high strength steel [138]. In a 4330 steel, the smaller sized population of inclusions are sub-micron sized Ti(C,N) and the larger sized population of inclusions are 1-10 µm TiN particles.

5.2.1 Void Nucleation Models

For strongly-bonded non-metallic particles, it is generally observed that cracking during plastic deformation is a primary mechanism for void initiation [72, 135]. In this case void nucleation often becomes the rate limiting step for ductile fracture [137, 139]. Particle cracking has been shown to be affected by particles size [135, 139, 140], matrix strength [141], particle shape [139, 142, 143], and cohesion strength of the matrix to the inclusion [139].

The void nucleation model developed by Argon [18] relates the stresses necessary for debonding of particles from the matrix to material properties and the imposed stress state. Argon also formulated stress-based criteria for debonding of interacting particles that have overlapping fields of plasticity. Interacting particles exist in samples where there are either: (1) high volume fractions of inclusion particles with

decreased spacing and therefore overlapping plastic zones or (2) higher stress concentrations, which extend the plastic zones surrounding the particles outward. Solutions for the particle-matrix interfacial stresses were also developed for non-hardening and linear-hardening matrix materials. Argon describes the total stress state by:

$$\sigma_c = \sigma_e + \sigma_m \tag{5.1}$$

where σ_c is the combined stress, σ_e is the effective stress, and σ_m is the mean hydrostatic tensile stress. The nucleation criteria for relatively small isolated particles ($< 100\mathring{A}$) is given when both equation 5.2 and equation 5.3 are satisfied.

$$\gamma_c = \frac{\gamma_y m}{6\sqrt{6}}(\frac{\sigma_i}{k_0} - 1)^2 \tag{5.2}$$

and

$$\frac{(\alpha - \alpha_i)\pi\rho^2}{\beta(\frac{\sigma_i^2}{2E})(\frac{2\pi\rho^3}{3})} < 1 \tag{5.3}$$

where γ_c is the critical plastic strain necessary to nucleate a void, ρ is the particle radius size, m is the Taylor factor (3.1), k_0 is the yield stress in shear, σ_i is the interfacial strength, α is the surface free energy of the cavity, α_i is the interfacial energy, and β is a coefficient of ~ 0.5. Argon combines and simplifies the expressions from 5.2 and 5.3 into:

$$\frac{\rho}{\beta} > \frac{3}{2}\frac{E}{\sigma_i} \tag{5.4}$$

by representing $(\alpha - \alpha_i)$ as $\sim \sigma_i \frac{b}{4}$.

A strain criteria above which multiple-particle interactions occur was also defined by Argon, where c is the volume fraction [76]:

$$\frac{\gamma}{\gamma_{y\,crit}} = \frac{m}{\sqrt{6}(n+1)}(\frac{\sqrt{2}}{m}(\sqrt{\frac{2\pi}{3c}} - \sqrt{\frac{8}{3}})^{n+1}). \tag{5.5}$$

The Argon model predicts that void nucleation occurs more readily in triaxial tensile stress fields, and that the nucleation strain decreases as hydrostatic stresses increase [137]. The model has been shown by Argon and Im to predict accurately in low-carbon steel [144].

Gurson [145] developed a strain controlled void nucleation criteria for elastic-plastic matrix materials. This model incorporated an existing void density into the calculation of the threshold strain necessary to nucleate voids in the following equation:

$$\Phi(\sigma_e, \sigma_m, \bar{\sigma}, f) = (\frac{\sigma_e}{\bar{\sigma}})^2 + 2f\cosh(\frac{\sigma_m}{2\bar{\sigma}}) - 1 - f^2 = 0 \tag{5.6}$$

where $\bar{\sigma}$ is the tensile flow strength f is the volume fraction of spherical voids and σ_e, σ_m are stress invariants defined in [63].

While the Argon and Gurson models describe stress states at the particle interfaces or the strain necessary for nucleation, more recently developed void nucleation models incorporate parameters that include terms to describe the initial 3D particle sizes and 3D spatial distribution of particles, information that can be provided by tomographic techniques such as the FSLSS [146–148].

Saje [63] outlines a nucleation model, with components stemming from Gurson's [145] plastic strain controlled nucleation model (equation 5.6), and an extension of Argon's [73] stress controlled nucleation models (equation 5.1).

$$(\dot{f}_{nucleation}) = A\dot{\bar{\sigma}} + \frac{1}{3}B\dot{\sigma_m} \tag{5.7}$$

where A is a flow stress dependent parameter, B has hydrostatic stress dependence described in the following strain controlled nucleation parameters, equation 5.8, and stress controlled nucleation parameters, equation 5.9.

$$A\bar{h} = \frac{\psi}{s\sqrt{2\pi}} \exp\left(-\frac{1}{2}\left(\frac{\epsilon^P - \epsilon_N}{s}\right)^2\right); B = 0 \tag{5.8}$$

$$A = B = \frac{\psi}{s\sigma_y\sqrt{2\pi}} \exp\left(-\frac{1}{2}\left(\frac{\bar{\sigma} + \frac{1}{3}\sigma_m - \sigma_N}{s\sigma_y}\right)^2\right) \tag{5.9}$$

where s is the standard deviation, ψ is the volume fraction of voids that would be nucleated if deformation continued indefinitely, and ϵ_N, σ_N are the maximum stress and maximum strain for void nucleation [63].

Butcher and Chen's nucleation model has been developed with further microstructural parameters incorporated [149]. The model is for strain related to nucleation and has the form:

$$\epsilon_N = \epsilon_{N0}\left(\frac{f_n}{f_{n-ave}}\right)^{1/3}\left(\frac{A}{A_{avg}}\right)^{1/4} \exp\left(-T(2 - \beta|\mu_L|)\right) \tag{5.10}$$

which defines the nucleation strain ϵ_N in terms of nucleation parameters β and ϵ_{N0}, the average particle area and area fraction A_{avg} and f_{n-avg}, the triaxiality stress state T, and the Lode parameter μ_L. This model can be flexibly applied to different systems of inclusion particles that have varied geometry and densities.

All of these void nucleation models require parameter inputs that describe the inclusion particle distribution. More detailed models can require additional particle description parameters that are available with 3D characterization techniques such as the FSLSS. Void nucleation models have been integrated with void growth models to predict particle decohesion and crack propagation. In the following section, void growth models will be discussed.

5.2.2 Void Growth Models

For cases where the inclusions are not well-bonded to the matrix or cases where the inclusions are easily deformable, nucleation of voids is typically not rate limiting,

and material toughness will be dictated by the energy required to grow and coalesce voids. Once voids are nucleated, the growth and eventual coalescence of said voids is modeled with growth equations. Early void growth models initially concentrated on the growth of single voids in bulk homogenous matrix material. More recent models, discussed later, have incorporated the complexities of multiple-particle interactions such as shear localization and banding.

Ashby developed a dislocation model for void growth in dispersion-hardened materials that relates the increase in volume ΔV, to the volume of the void nucleating particle V based on the shear strain on the primary slip band a, shown in equation 5.11. For the most part though, continuum modeling approaches have been more predictive for void growth. The Ashby growth model gives:

$$\frac{\Delta V}{V} \sim \frac{a}{2} \tag{5.11}$$

and the corresponding cavitation stress solution for the void-particle interface is,

$$\sigma_v \sim \alpha\beta\frac{\epsilon a}{bL} \tag{5.12}$$

where a is the nucleating particle size, b is the Burger's vector, L is the dislocation pile-up size, and α and β are constants [150]. The Ashby model predicts void growth to occur by slip of prismatic loops, which require high stresses for movement. More recently, continuum models have been used to produce more realistic void growth rates.

Two early models for continuum void growth modeling were developed by McClintock [151] and then later Rice and Tracey [78]. McClintock analyzed axisymmetrically stresses states in cylindrical voids modeled is both linear work hardening materials and rigid-nonhardening materials. This system models a deformable matrix with a series of hard, non-deformable, ceramic inclusions. A further development of the

model relates R the mean of the semiaxis of the void, α a constant, ϵ the equivalent plastic strain to the mean stress σ_m, as follows [152]:

$$\frac{1}{R}\frac{dR}{d\bar{\epsilon}} = \frac{\alpha}{1-n}\sinh[(1-n)\frac{\sigma_m}{\tau_0}] \tag{5.13}$$

The Rice-Tracey Model, 5.14, describes the relation between a single void in a matrix, with no void-void interactions and therefore no ultimate failure. Similar to 5.20, this model can be combined with failure criterion to predict ductile fracture. The Rice-Tracey model can help understand the growth rates of voids as the process zone of a crack comes into contact with them.

$$\ln\frac{\overline{R}}{R_0} = 0.283\int_0^{\varepsilon_{eq}} exp[\frac{1.5\sigma_m}{\sigma_{ys}}]\mathrm{d}\varepsilon_{eq}^P \tag{5.14}$$

Where $\overline{R} = (R_1 + R_2 + R_3)/3$ and ε_{eq}^P is the equivalent von Mises plastic strain.

Void growth in 4330 steel is limited by void nucleation. This is because the TiN inclusions in the 4330 steel are strongly bonded to the matrix, are hard and ceramic, and are not easily deformable. Therefore, once void nucleation criteria are satisfied, the void growth criteria has already been satisfied, and voids usually begin to grow and coalesce immediately.

5.2.3 Other Particle Parameters

Generally, it would appear that particle size would directly influence the toughness of a material. This relationship, however, is not straightforward. In some systems there is a strong interdependence of properties on particle size and particle spacing. The large particles can develop premature voiding in a material, which then creates local stress concentrations initiating void formation and growth at and between smaller scale particles [139].

Larger particles also require less strain for void nucleation [11, 153, 154]. Within

a distribution of particles, the larger ones will nucleate voids first [72, 73, 135]. Gurland, for instance, saw that the average size of cementite particles that had fractured during tensile testing was greater than the average cementite particle size in their spheroidized carbon tool steel samples. Horstemeyer and Gokahle developed a model that relates the particle diameter d and area A to the nucleation strain $g(d)$ in equation 5.15.

$$g(d) = \frac{1}{\sqrt{d}} = (\frac{4}{\pi}A)^{-1/4} \tag{5.15}$$

Particle size has also often been linked to particle cracking [18, 72, 155]. This is attributed either to the increased size and likelihood for surface or internal defects (as per a Griffith-type [156] explanation) of ceramic non-metallic particles failing in a brittle fashion [72], or to increased multiple interacting particle effects [18]. Especially under increased matrix plasticity in the process zone of a propagating crack, hard non-metallic particles are often assumed to deform elastically, leading to fracture from the high hydrostatic stresses. Shabrov and Needleman noticed distinct size effects in a 4330 steel alloy similar to that used in this thesis [134]. Using notched tensile bars of this steel, they experimented with different ratios of triaxiality and loading conditions, and found a narrow load range in which most Ti(C,N) inclusions simultaneously fractured and nucleated voids. The large Ti(C,N) inclusions cracked first with subsequent cracking in smaller particles requiring higher loads. Using a void-nucleation model, they also found a criteria of $\Sigma_N \sim 2.3 - 2.4\,\mathrm{GPa}$ at which voids would nucleate. Their void nucleation criteria for the model is as follows (equation 5.17), where ρ is a parameter that defines the stress state the sample is in (i.e., hydrostatic or uniaxial tension, more description in [134]), c is a term dependent on volume fraction, material properties, and morphology [157, 158].

$$\sigma_e + c\sigma_h \equiv \sigma_n = \Sigma_N \tag{5.16}$$

$$(|1-\rho| + \frac{c}{3}(1+2\rho))\sigma = \Sigma_N \tag{5.17}$$

Particle spacing, can be just as important as the size of the particles in a material. In work by Garrison [159], a relation between particle spacing, particle size, and toughness was discovered. For intra-lath carbide inclusions ranging from 8-61 µm, the highest toughness for an AF1410 steel was developed when the inclusion spacing was large and when the average inclusion size was large. Garrison therefore suggests that the volume fraction of inclusion particles is a less important measure than the void growth ratio, $\frac{R_v}{R_I}|_{R_0}$, or the interparticle spacing NN_{dist}.

The stresses state imposed on an inclusion can also influence its propensity to nucleate voids. Cox and Low [72] investigated the role of stress triaxiality by tensile testing 4340 steel specimens with MnS inclusions. They prepared 4340 steel samples and 18 nickel 200 grade maraging steel to compare fracture toughness with difference inclusion populations and stress states. By comparing the smooth and notched tensile samples, they were able to deduce that the amount of triaxiality did not influence void initiation, but did dramatically raise the void growth rates.

Shabrov and Needleman [11] also observed effects of particle size and stress state effects in their modeling. When low stress triaxiality was imposed on the system, void nucleation occurred at high nucleation strains for all inclusion sizes, with regular particle distributions requiring higher strains than normal distributions. At heightened stress triaxiality, void nucleation occurred at lower nucleation strains in systems with larger average particle sizes than for systems with smaller average particle sizes. These results show that the amount of stress triaxiality can shift the dominant nucleation strain parameter from particle clustering (defined by the type of particle distribution) to particle size. Overall, increased clustering (type of particle distribution) and decreased nucleation strains for void formation were most prominent when average particle sizes were smaller than $\frac{1}{5}$ of the bounding box size L_0 for each cell in

the simulation.

In work by Ohno and Hutchinson [160], a relation between triaxiality and void clusters was developed. They showed that single voids and particularly clusters of voids can be deleterious in regions of high triaxiality, such as the plastic zone of a crack, although these voids are significantly more benign when located in regions of low triaxiality. Since this model suggests that even small voids are potentially quite damaging to ductility in the plastic zone, all voids or void nucleators can be regarded as being troublesome, especially since crack paths in service parts are not always reliably predicted.

The orientation of particles and their geometry can be important to their role in void formation during plasticity. In work by Beremin [136], the morphology of MnS inclusions heavily influenced the type of voiding that was initiated. When the MnS stringer-like inclusions were oriented with their long axis parallel with the loading axis, the inclusions tended to fracture and nucleate voids. However, when the MnS inclusions were oriented with long axis transverse to the loading direction, the MnS particles debonded at the weaker matrix interface. Similarly, Gurland found that cementite particles cracked at preferentially lower stresses if their long axis was aligned with the loading axis [135]. In fact, cracks tended to develop perpendicular to the direction of maximum tensile strain within these particles.

5.2.4 Cohesion Models

The Rice-Johnson Model was the first traction-cohesion model to incorporate voids into fracture toughness modeling [161]. They predicted that size and spacing of inclusions would influence fracture toughness, but their model only included crack tip interactions with the next closest void, neglecting void sheet interactions and other longer range effects. Their model for crack opening displacement (δ_{IC}) is:

$$\delta_{IC} = X_0 F(\frac{X_0}{R_0}) = X_0 F(f^{-1/3}) \tag{5.18}$$

where X_0 is average 3D nearest neighbor distance and F is a function of R_0, the average inclusion radius, or f the volume fraction of inclusions. This relation was used to model the interaction of a blunting crack tip with a particle. The failure criterion is for fracture of the ligaments between the inclusion-initiated void and the crack. Failure occurs when the vertical crack size becomes equal to the vertical void size.

The Garrison-Moody Model, equation 5.19, relates the crack tip opening displacement to the void nucleating inclusion sizes and the void radii.

$$\delta_{IC} \sim X_0(\frac{R_v}{R_I})|_{R_0} \tag{5.19}$$

Here δ_{IC} is the crack tip opening displacement at fracture initiation, X_0 is the average 3D nearest neighbor distance between inclusions, R_v is the void radius, R_I is the radius of inclusion initiating the void, and R_0 is the average inclusion radius [162, 163]. In Garrison's model, he has extended the work of Rice-Johnson to include a ductility term, $\frac{R_v}{R_I}$.

The Gurson-Tvergaard Model 5.20 approximates a material with a regular distribution of voids to act as a continuum [145, 164, 165]. This model can predict average properties and ductile fracture based on applied plastic instability criteria, but it cannot predict void-void interactions, the effects of anisotropic voids, or localized heterogeneously distributed void regions. This model is useful as a starting point to determine what the ideal properties of a material with specific void distributions. Using the Gurson-Tvergaard Model, datasets sectioned using the FSLSS technique could be used to estimate the failure criteria for ideal homogeneous samples.

$$g(\sigma_e, \sigma_m, \overline{\sigma}, f) = (\frac{\sigma_e}{\overline{\sigma}}) + 2q_1 f \cosh \frac{3q_2\sigma_m}{2\overline{\sigma}} - (1 + q_3 f^2) = 0 \tag{5.20}$$

In this model σ_e is the macroscopic von Mises stress, σ_m is the macroscopic mean stress, $\overline{\sigma}$ is the flow stress for the matrix, f is the current void fraction, and q_1, q_2, q_3 are fitting parameters.

More recently, these types of models have been improved upon by Hutchinson and Tvergaard [166]. Their model now integrates aspects of Needleman's interface decohesion work [157], Griffith's crack propagation criterion [156], the finite-strain generalizations of J_2 flow theory from Hutchinson [167], the J-integral from Rice's 1968 work [168], the Rice-Johnson fracture process model [161], and the yield condition of the Gurson model [145].

To achieve realistic predictions for engineering materials, the models have become more complex, integrating void nucleation, void growth, failure, decohesion, and continuum models and criteria. An integrated model such as this will be discussed in Section 5.2.6 that has been developed for use with 3D data collected from techniques such as the FSLSS.

5.2.5 Finite Element Analysis

Finite element analysis (FEA) can be used in conjunction with a failure criteria to simulate crack propagation, and therefore fracture toughness, by modeling shear localization between the larger TiN inclusions and microvoid coalescence between the smaller TiC inclusions. An early effort to apply finite element analysis to crack tip propagation by McMeeking and Aravas [169] treated the effects of voids in high strength alloy (HSA) steels on crack growth. Aravas and McMeeking used Tvergaard and Needleman's [170] modified Gurson constitutive equations to model the matrix material. They found that the simple Gurson model produced crack opening displacement values quite close to the FEA results, possibly because that the Gurson

model has more inclusion-void information embedded in it. The McMeeking Model addresses the interactions of the crack tip with the next closest single void, but more recently, Tvergaard and Hutchinson have developed a model for the crack tip interaction with multiple voids [171]. Hutchinson and Tvergaard suggest that the complexity of multiple inclusion interactions in the proximity of a crack tip require multiple mechanisms and thereby, the integration of multiple microstructural parameters to best understand toughness and crack propagation. A drawback of finite element analysis is that it requires a detailed mesh of the microstructures being modeled, which can be very computationally intensive. Therefore, a number of models have been developed which use a hybrid structure to only compute the physics necessary to resolve the required details at the required lengthscale.

5.2.6 Multiscale Modeling with Homogenized Constitutive Relations

Void nucleation, void growth, microvoid linkup, and crack propagation occur over several length scales. Void nucleation and void growth can occur at both the 1-10 µm scale, occurring at TiN interfaces with the matrix, or at sub-µm scale in the case of TiC microvoiding. The subsequent linkup of large voids through a series of microvoid localizations also occur across these length scales, yet crack propagation occurs on the larger 10-100 µm scale. All these physical mechanisms are critical for the modeling of toughness and ductile fracture. Current computational limitations require a more adaptive form of modeling, whereby the resolution of the model is only as fine as required by the physics locally. A number of models have been developed to help relate microstructural parameters and stress or strain conditions to material behavior [172], such as ductile fracture [146, 171, 173]. The void nucleation, growth and crack propagation equations from the previous sections, 5.2, are combined to create multiscale models that adaptively incorporate these models at different length scales.

Early models intended to integrate multiscale microstructure parameters, such as the presence of voids or inclusions, into the matrix material considering it as a homogeneous continuum. These models are useful for many cases, but can fail, particularly in situations where outliers in the distributions or unfavorable heterogeneous microstructures govern the material properties, such as predicting ductile failure.

By investigating the input parameters from many ductile fracture models, one can determine which are important for toughness modeling. These parameters include:

- The rate limiting steps for ductile fracture (void nucleation or void growth/coalescence)
- The size of the plastic / process zone in front of a crack
- Average particle spacing and therefore the likely number of interacting particles within the process zone.
- Particle size: can dictate the likelihood of particle fracture vs. debonding (influence rate limiting step), can influence the stresses in the process zone.
- Spatial distribution of particles, unfavorable orientations - artifacts of forging can produce particles with long range order and increase likelihood of void sheets or easy crack propagation paths.
- Particle clustering - groups of small particles may act as a larger particle, nucleation or growth may occur simultaneously in clusters - increasing their net effect on strength.
- Interfacial adhesion of particles to the matrix

In Figure 5.3, the parameters that are influential for modeling toughness are shown schematically. The items marked with green circles are parameters that can be extracted from FSLSS datasets.

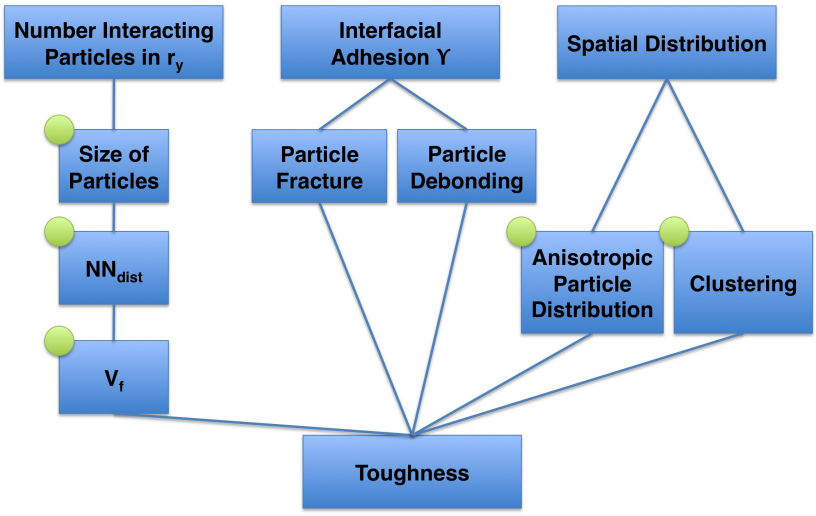

Figure 5.3: Schematic showing the parameters influencing toughness modeling. Those marked with green dots are available from the FSLSS technique. The interfacial adhesion γ can be calculated using density functional theorgy (DFT) or interface strength measurements.

The work of Vernerey *et al.* [146, 174] on multiscale modeling of ductile fracture has been developing in conjunction with the recent advancements of 3D tomographic techniques [175]. The uniquely available 3D data accessible using the FSLSS technique can be input into these ductile fracture models to develop a better understanding of the effects of different spatial particle distributions and clustering. The primary parameters captured by the FSLSS technique are: volume fraction V_f, mean particle size $\mu_{particle}$, average nearest neighbor distance NN_{dist}, and the spatial position of the particles in 3D. In Figure 5.4, the spatial distribution of particles would be input into the local description of the damage region, the NN_{dist} would be used for the spacing between inclusions, the TiN particles sizes would define l_1, and the continuum material parameters could be calculated by the v_f, $\mu_{particle}$, and NN_{dist} of TiN particles from the 3D datasets.

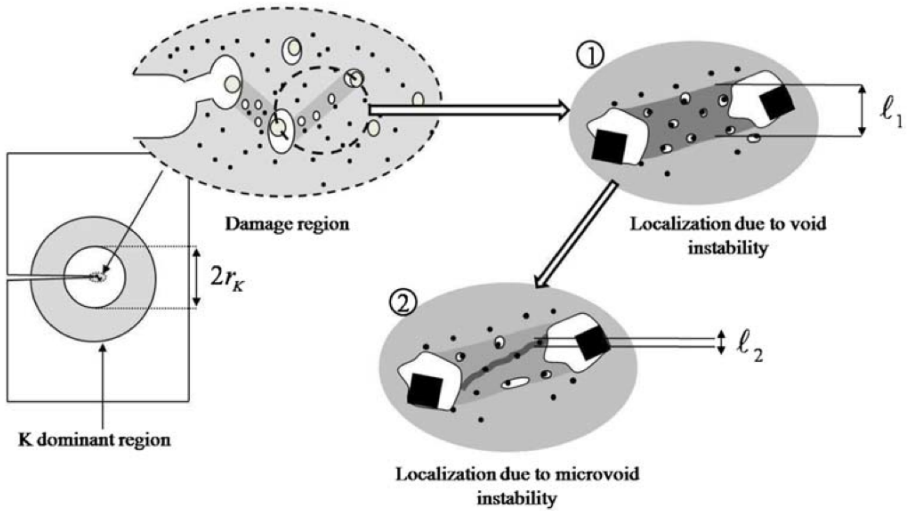

Figure 5.4: Schematic of the length scales and microstructural interactions necessary for modeling ductile fracture [146]. A representative cracked sample is shown on the (left) with an inset r_K process zone where stress concentrations and triaxiality are enhanced due to the proximity to the crack tip. The damage region shows the relevant microstructure in a steel specimen, primary TiN particles with primary voids (l_1 sized), and secondary TiC particles with secondary voids (l_2 sized).

The recent multi-length scale models constructed by Vernerey *et al.* calculate the fracture toughness K_{IC} as a function of the hardening parameter h, the interfacial strength of the Fe:TiC interface σ^s, the interfacial strength of the Fe:TiN interface σ^p, and the volume fraction of primary inclusions f^p (see equation 5.21).

$$K_{IC} = F(h, \sigma^s, \sigma^p, f^p) \tag{5.21}$$

The constitutive relation at the macro-scale is:

$$\Phi(\sigma) = (\frac{\sigma_{eq}}{\sigma_y})^2 - 1 + 2q_1(f^p + f^s)\cosh(\frac{3q_2\sigma_m}{2\sigma_y} - q_3(f^p + f^2)^2 = 0 \tag{5.22}$$

where f^p is the porosity nucleating from the primary particles, f^s is the porosity nucleating from secondary particles, and ϵ, σ_{eq}, and σ_m are the effective plastic

strain, equivalent stress, and hydrostatic stress [146]. This relation has the form of the Gurson-Tvergaard-Needleman void growth model [176, 177] for a incompressible, perfectly plastic medium with added void nucleation and void coalescence terms.

The micro-stress yield criteria for when the matrix material fails after large voids are nucleated from primary particles is:

$$\Phi^1(\bar{\beta}^1, \bar{\bar{\beta}}^1) = (\beta^1 + \alpha\beta_m^1) - \beta_y^1 = 0 \tag{5.23}$$

where β^1 and β_m^1 are the equivalent and hydrostatic modified micro-stresses and β_y^1 is the microscopic yield stress.

The inhomogeneous stress fields surrounding voids nucleated from secondary particles are defined by:

$$\Phi^2(\bar{\beta}^2, \bar{\bar{\beta}}^2) = \beta^2 - \beta_y^2 = 0 \tag{5.24}$$

where β^2 and β_y^2 are the overall equivalent micro-stress and submicro-yield stress as defined by Vernerey [138]. This equation models the ligament instabilities between adjacent voids as an incompressible plastic continuum.

Hybrid modeling structures such as Vernerey's aim to combine the detailed physics of dislocation models with broader scaled constitutive models, and bulk continuum models. For instance, the dislocation models are used to determine when the interface between inclusion particles will debond or fracture, passing that information up a level to constitutive models which relate to shear localization between particles in the process zone. For material far from the process zone, continuum models estimate the bulk response. Each of the transitions from different levels of detail is accompanied by a yield criterion. The first level details localization between primary particles, the second level details the microvoiding between the smaller secondary particles, and the third level details the rupture of ligaments between the microvoids. In Figure 5.4,

the hierarchy of mechanisms important for ductile fracture are shown [146]. In the schematic, r_k is on the order of 100's of µm, l_1 is 1-10 µms, and l_2 is less than 1 µm.

5.3 FSLSS of 4330 Steel

The newly developed FSLSS technique presents the unique opportunity to access large volumes of data at fast acquisition rates. Not only does this permit the acquisition of large continuous volume of data, but as described in this chapter, distinct samplings from many regions within a volume of material may also be made. As an explicit example, detailed analysis of laser-material interactions and FSLSS data has been collected for a titanium modified 4330 steel to support the development of models for fracture toughness. In the upcoming sections the following is discussed: (a) laser parameters optimized by single pulse laser experiments and laser machining experiments, (b) collection of 3D datasets with the FSLSS technique (c) comparison with traditional means of microstructural data collection, and (d) statistical analysis and modeling of toughness. Validation has also been a significant effort in the process of the design and operation of the new FSLSS tomographic technique. In Section 5.6, existing mechanical serial sectioning methods, 2D stereological methods, and deep etching were used to compare reconstructed TiN particle morphologies and statistical parameters for validation of the FSLSS technique.

5.4 Single Pulse Femtosecond Laser Ablation

Single pulse laser studies have been an integral part of understanding the machining characteristics and removal rates associated with femtosecond laser machining. Single pulse ablation spots were characterized using SEM and AFM to measure cross-sectional depth and equivalent ablation diameters. Figure 3.9 shows a compilation of various single pulse ablation studies taken from the literature, and the general

removal rate trends of the high and low fluence regimes of these metals, ceramics, and polymers. If ablation rates for two or more phases can be matched at the same fluence then material can be removed simultaneously by femtosecond laser ablation. Therefore, multi-phase material removal is viable for many different multi-component systems in the incident laser pulse deposition configuration.

The cumulative effects of millions of femtosecond pulse ablation events was investigated after FSLSS experiments were conducted. Surface texturing or roughness was found to be dependent on both the laser scanning patterns as well as the laser pulse fluence. A scanning electron microscope image in Figure 5.5 shows the surface of a laser machined 4330 steel with low surface roughness after material removal at a rate of $0.25 \times 10^6\,\mu m^3/min$. Laser machining in the low fluence regime produced the lowest average surface roughness (Ra = 0.1-0.2 µm), as measured by profilometry. In the low fluence regime most materials exhibit material removal with low collateral damage in the range of 30-50 nm/pulse, with less variance in ablation depths per fluence than in the high fluence regime. As a result, the uniformity of material removal in the low fluence regime enables the simultaneous two-phase removal of TiN inclusions and the steel matrix, in the Ti-modified 4330 steel system.

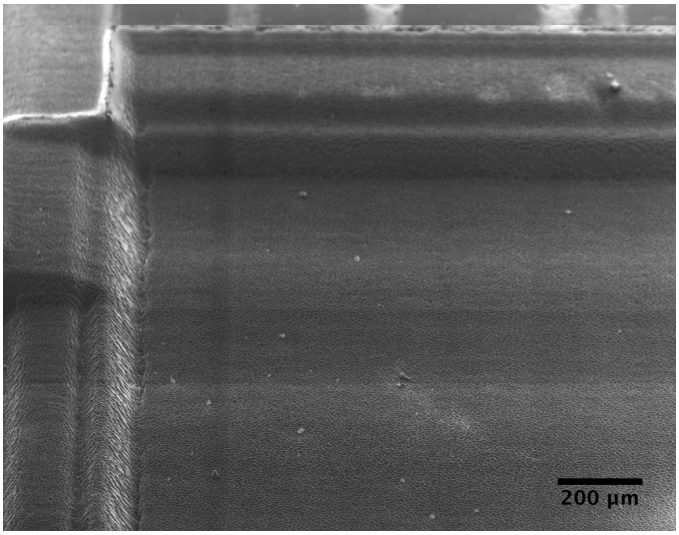

Figure 5.5: SEM image of 4330 steel after 80 slices of FSLSS machining for a cumulative removal depth of 45 µm.

5.4.1 Single Pulse Ablation of TiN and 4330 Steel

In order to establish relevant laser operating conditions for uniform ablation of layers of 4330 steel containing nanometer textured, µm-sized titanium nitride (TiN) particles, a series of single pulse studies were performed on the sample material. Laser irradiation was performed on metallographically flat polished samples for fluences ranging from 0.1-3 J/cm^2 for TiN and 0.35-10.1 J/cm^2 for 316 stainless steel. In the 316 stainless steel study, 780 nm wavelength, 150 femtosecond pulses were used for ablation. For the TiN study, 800 nm wavelength, 40 femtosecond pulses were used for ablation. Atomic force microscopy (AFM) measurements of material removal rates in both TiN [126] and a 316 stainless steel [119] are plotted in Figure 5.6 [119, 126]. The ablation depth per pulse for these two materials differs by less than 5 nm per pulse, in the low fluence regime. These AFM data predict that simultaneous and uniform ablation for steel and hard TiN phases will be possible in the low fluence regime, at approximately 2 J/cm^2 and from 0.2-0.4 J/cm^2. FSLSS experiments are performed in the range of 0.9-1.6 J/cm^2, near the low to high fluence transition for

steel. Experimentally, uniform two-phase ablation occurs below $2\,\mathrm{J/cm^2}$.

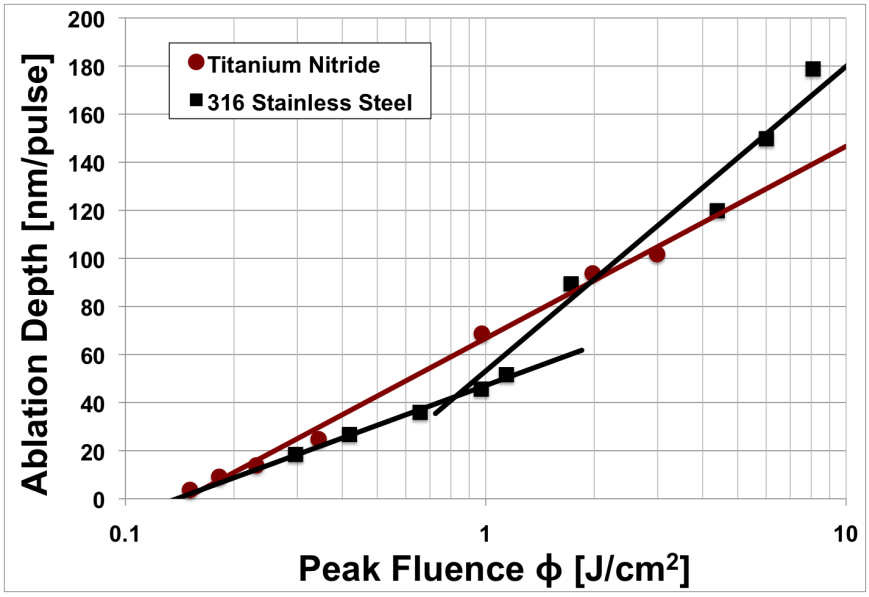

Figure 5.6: Ablation depth per pulse for 316 stainless steel and a TiN coating. The ideal FSLSS machining range is below $2\,\mathrm{J/cm^2}$. In this region the ablation rate for both materials is within 15 nm/pulse. All FSLSS experiments are performed in the fluence regime below $2\,\mathrm{J/cm^2}$.

5.5 TiN Particles Reconstructed in 4330 Matrix

The FSLSS technique was used to collect 3D datasets from 4330 steel to characterize the TiN inclusion particles. A 3D reconstructed 4330 steel dataset collected with the new 3D tomographic laser sectioning process is shown in Figure 5.7. This 3D dataset is composed of 407 slices with a sampling thickness of 0.23 µm/slice and an in-plane imaging resolution of 0.15 µm/pixel. The total volume of this reconstructed dataset is $315\times156\times89$ µm. Once parameters for the MATLAB image segmentation code were selected, approximately 30 seconds per image was required to image segment TiN particles from the 4330 steel matrix. The femtosecond-laser machining step of the serial sectioning process for a single 1.5×1.5 mm region requires approximately 7 minutes, with a slice removal depth of 0.23 µm (Figure 5.8). The total acquisition time for the reconstructed 4330 steel dataset was 41 hours, with no human supervi-

sion required beyond the initial setup. Statistical analysis of the specific dataset in Figure 5.7 was performed using IDL to calculate the volume fraction of TiN particles, 0.028 %; the particle density, 2.84×10^{13} particles/m^3; the mean particle diameter, 2.12 µm; the mean nearest-neighbor distance, 10.0 µm; and total number of particles, 112.

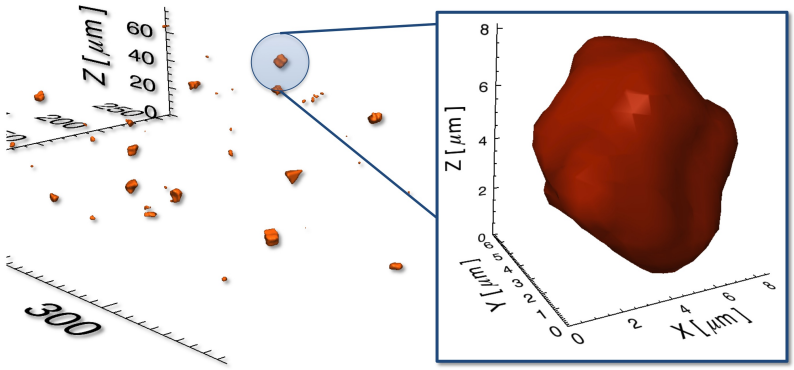

Figure 5.7: FSLSS reconstruction of TiN inclusions in 4330 titanium modified steel. 407 slice thick dataset with a 0.23 µm/slice sectioning resolution and an imaging resolution of 0.15 µm/pixel. (right) An individual TiN particle reconstructed showing the cuboidal nature of the particles and their large 8 µm diameters.

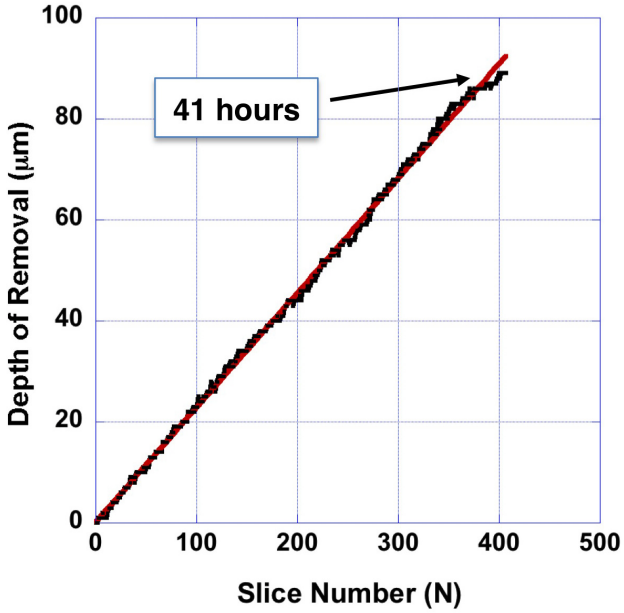

Figure 5.8: Linear material removal throughout the entire 41 hour dataset collection. Removal rate is measured using the calibrated three-axis high-precision stage coupled with the small depth of focus for the 20x objective microscope used to image the sample surface during a FSLSS experiment.

Six other datatsets were collected with a total volume of $2334\times1666\times471\,\mu m^3$ and were statistically analyzed using IDL code developed by H.J. Jou [178] at QUESTEK. These additional captured datasets have also been analyzed statistically in 3D and the corresponding local statistical information is summarized in table 5.1. The mean size of the TiN particles is $2.07 \pm 0.55\,\mu m$ as determined from the six collected FSLSS 3D datasets, or $4.83 \pm 1.61\,\mu m$ as determined from 2D stereology. The 3D TiN mean nearest neighbor spacing, as measured from the average of six FSLSS datasets is $14.8 \pm 7.8\,\mu m$. The 3D approximation, using Equation 5.25 and the 2D stereological data, of the TiN mean nearest neighbor distance is $11.64 \pm 2.66\,\mu m$

Dataset *Size (μm)*	FSL#1 *[315, 156, 89]*	FSL#2 *[404, 303, 149]*	FSL#3 *[404,302,78]*	FSL#4 *[404,302,59]*	FSL#5 *[404,302,54]*	Total /Average
# Part.	112	212	79	81	44	528
Part. ρ (#/m^3)	2.84 x 10^{13}	1.19 x 10^{13}	0.83 x 10^{13}	1.21 x 10^{13}	0.66 x 10^{13}	1.15 x 10^{13}
V_{frac} (%)	0.028	0.044	0.020	0.029	0.019	0.032
<Dia> (μm)	2.12	2.14	2.44	1.93	2.86	2.27
<NN> (μm)	10.0	6.0	18.6	14.6	23.30	12.82

Table 5.1: FSLSS 3D dataset statistics of TiN inclusions in titanium modified 4330 steel.

The six datasets were collected from different volumes within the original wrought material and their statistical parameters varied with sampling location. The 4330 steel has volume fractions ranging from 0.19-0.44 % across a 3 cm section of material. The full set of the 3D reconstructions of datasets are shown visually in appendix A. The application of the FSLSS process to this multi-phase material, containing both hard ceramic inclusion phases and a softer metallic steel matrix, shows that the technique has broad applicability to other microstructurally complex materials. The material removal rates in the low fluence regime have also been shown to be relatively consistent for both hard ceramic and softer metallic phases.

5.6 Characterization of Inclusions

The TiN particles found in 4330 steels can be highly heterogeneously distributed and vary greatly in volume fraction and size depending on the processing condition, initial chemistry, and location within the processed material. The distributions of these particles, their frequency, and their morphology influence their mechanical properties, it is important to accurately characterize them in order to better understand the most desirable microstructural configurations and the processing conditions which will yield those configurations. The FSLSS technique can be used to better

understand the 3D distribution of these TiN particles. Additionally, to assess the potential drawbacks and benefits of the 3D approach, 2D stereological microscopy and depth profiling techniques were applied.

5.7 Comparison of 2D and 3D TiN Statistics

The statistical information collected from the FSLSS 3D datasets provides new insight into ways to model material properties more accurately. All statistical measures are true 3D measurements collected over volumes that are orders of magnitude larger (when considered as the sum of the area of the total number of slices) than the information typically collected during a 2D stereological study. The 3D particle shapes are reconstructed from many 2D sections and are not approximations made from single slices. Stereology techniques rely on statistical data collected from a set of 2D slices to correlate what the mean particle sizes, nearest neighbor distances, and volume fractions are. The 2D method homogenizes the data and loses local spatial information, such as particle clustering, and outlier information which may not be characterized due to the small sampling areas. Approximations used to convert 2D slice information into 3D are shown in equation 5.25, a nearest neighbor conversion, which is dependent on the mean radius calculation in equation 5.26. A 2D to 3D volume fraction conversion is also shown in equation 5.27.

The 2D stereological conversion equation for calculating a 3D X_0 approximation from measured 2D parameters follows:

$$X_0 = 0.89 R_0 f^{-1/3} \tag{5.25}$$

where X_0 is the average nearest neighbor particle spacing, R_0 is the mean particle radius defined in 5.26, and f is the volume fraction. The mean particle radius R_0 is:

$$R_0 = \frac{1}{4}\pi H(d) \tag{5.26}$$

where $H(d)$ is the harmonic mean of the stereologically measured particle diameters. The 2D to 3D volume fraction conversion equation is:

$$f_v = N_a \pi R^2 \tag{5.27}$$

where N_a is the area number density and R is the geometric mean particle radius.

The 2D stereological approximations may not capture the tails of the distribution of particle sizes due to sampling area deficiencies. The particle size approximations rely on prior information about microstructure shape in order to estimate from a variety of random microstructure cross-sections the size distribution. For a system of equiaxed particles, this is a reasonable assumption, but with heterogeneous microstructures the estimation of 3D shape from a random 2D section is not accurate. Other heterogeneities such as particle clustering, which can have complex 3D orientation will not be captured by a 2D section or a 2D parameter such as 2D nearest neighbor distance. A 3D dataset reconstruction is required to accurately represent complex 3D structures.

5.7.1 Validation - Particle Shapes and Sizes

One goal of this research, and the development of the FSLSS technique, was to produce data that more accurately represents true 3D microstructures of materials. In the 4330 steel system, we mainly aimed to understand the spatial arrangement and size distribution of the TiN precipitates in order to predict material properties such as toughness. As such, various techniques were used to collect data about these distributions in order to compare with the FSLSS technique developed to capture 3D microstructures. One approach to capturing approximate 3D information about TiN

inclusion size was by preferentially deep etching 4330 steel, leaving the non-dissolved TiN particles exposed. This technique collects information about the size and shape of the TiN particles, but loses all information about their spatial distribution. A light electrochemical etch of 1 % tetramethylammonium chloride and 10 % acetylacetone in methanol for 1-2 minutes was used to selectively dissolve the matrix. The TiN particles were imaged with high tilt angles in a SEM to quantify precipitate morphologies and sizes, as shown in Figure 5.9. Sizes of the TiN particles range from 1-10 µm, with some particles appearing fractured or joined to other particles.

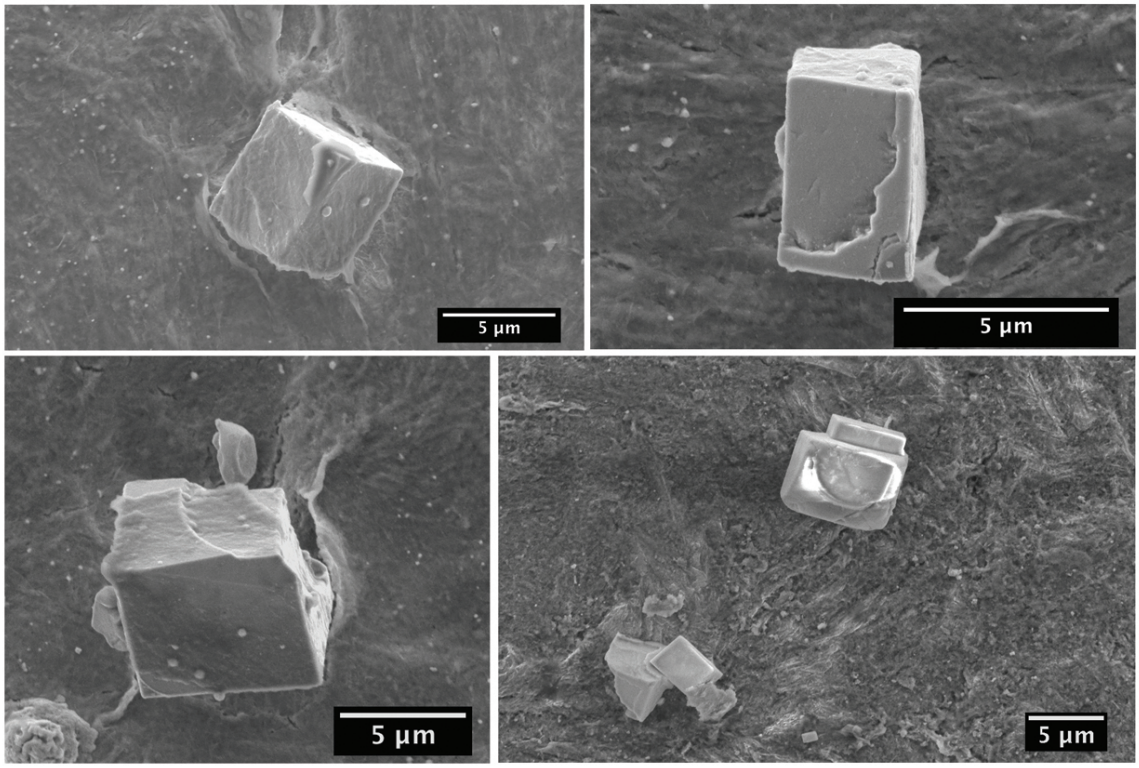

Figure 5.9: Various TiN particles deep etched out of the 4330 matrix. Their morphology is mostly cuboidal and they range in size from 1-10 µm. Some particles appear partially fractured or joined to other TiN particles.

5.7.2 Stereology

Stereology was also used to characterize the particles in 2D with a traditional metallographic approach. Stereology is useful for collecting 2D statistics about relative

location and particle size distributions, but can be misrepresentative of anisotropic 3D characteristics such as particle clustering, spatial orientation, or geometry [14]. Random sections were taken from a 4330 steel forged double-linear shear test bar end cut at various angles. A total area of $22435 \times 16826\,\mu m^2$ ($0.3775 \times 10^9\,\mu m^2$) was analyzed with 281 precipitates measured from 50 slices. A volume fraction of 0.057 and a mean particle diameter of 4.83 µm were calculated from the 2D stereology measurements. Particle statistics were collected by segmentation of the images through color-contrast and Gaussian filters, as illustrated in Figure 5.10. The stereologically measured 2D particle size measurements are listed with the 3D FSLSS measurements in Table 5.2. All techniques (mechanical serial sectioning, FSLSS, and stereology) produced particle parameters that were within a factor of 2-3 of each other. The 2D stereology measurements show a larger mean particle size and a larger mean nearest neighbor distance, suggesting that smaller particles are underrepresented. Whereas the FSLSS and mechanical serial sectioning datasets collected distributions with lower mean particle sizes and smaller average nearest neighbor distance. The larger sampling volumes characterized by the 3D techniques seems to better represent the small particles that the 2D stereological techniques. This could be verified by collecting more 2D sections, therefore collecting larger representative areas of material, with the hypothesis that mean particle sizes and nearest neighbor distances would correspondingly decrease.

Mechanical SS 1, shown in Figure 5.2, was collected with an imaging resolution of 0.95 µm/pixel and a sectioning resolution (slice depth) of 2.6 µm/pixel. Mechanical SS 2, shown in Figure 5.2, was collected with an imaging resolution of 0.13 µm/pixel and a sectioning resolution (slice depth) of 1.5 µm/pixel. The segmentation of Mechanical SS 1 was over-predictive of particle sizes and volume fraction, due to the lower datasets resolution [133]. Mechanical SS 2 shows a lower volume fraction and average particle size, which is more similar to the values collected using the FSLSS technique and 2D

stereology.

Figure 5.10: (Top Image) Photostitched collection of optical micrograph of polished 4330 steel collected from a random 2D cross-section in the bar-end of a double-linear shear test specimen. Cuboidal titanium nitrides were segmented out from thunder-represente matrix using basic thresholding algorithms and gaussian filters to create a binary image (Bottom Image).

Table 5.2: Statistical comparison of an aggregated set of FSLSS datasets, 2D stereological collected particle information, and two mechanical serial sectioning datasets. Statistical analysis was performed using IDL code courtesy H. Jou (QUESTEK).

Method	Particles Analyzed	Mean Diameter [µm]	V_f or A_f [%]	NN_{dist} [µm]
FSLSS	888	2.07	0.032	14.79
2D stereology	281	4.83	0.057	25.92
Mechanical SS 1	1092	4.86	0.176	15.8
Mechanical SS 2	33015	1.79	0.057	6.7

A significant benefit of 3D sectioning and reconstruction tools is the ability to accurately measure statistical parameters that represent microstructure in 3D. Traditionally parameters such as nearest neighbor distance are approximated from 2D stereology using equations such as 5.28, which approximates the 3D nearest neighbor

particle spacing X_0 as a function of the 2D average particle size R_0 and the 2D volume fraction of particles f.

$$X_0 = 0.89 * R_0 * f^{-1/3} \tag{5.28}$$

To summarize, mechanical and femtosecond laser serial sectioning both provide similar statistical measures of particle parameters such as average size and average nearest neighbor distances. Stereological techniques appear to under-represent the smaller particles compared with the direct 3D techniques.

5.8 Comparison to Mechanical Serially Sectioned Datasets

In collaboration with S. Chan and G.B. Olson (Northwestern University) and G. Spanos and D. Rowenhorst (Naval Research Labs), 4330 steel was analyzed using conventional mechanical serial sectioning approaches outlined in the methodology of this reference [58]. At NRL mechanical serial sectioning was used to reconstruct two 3D datasets, one of size $633 \times 516 \times 259\,\mu m$ and one of size $1000 \times 800 \times 300\,\mu m$ [133]. The larger dataset was captured with an imaging resolution of $0.13\,\mu m$/pixel and a slice resolution of $1.5\,\mu m$/pixel and the smaller dataset was captured with an imaging resolution of $0.95\,\mu m$/pixel and a slice resolution of $2.6\,\mu m$/pixel. A segmented and reconstructed image of the higher resolution dataset is shown in Figure 5.11, which required on the order of 2 to 6 months to fully reconstruct. This dataset was collected from the volume surrounding the process zone of the propagating crack in an interrupted test with a compact tension sample. Both specimens analyzed by S. Chan were of similar nominal composition as the double-linear shear bar specimens analyzed with the FSLSS technique, but of slightly different processing conditions. TiN nitrides are oriented along the reconstructed Y-axis, which was normal to the radial forging axis. Chan also used the reconstructions to measure crack tip opening

displacement (CTOD), a measure of toughness, and the void growth ratios R_v/R_i a parameter used for modeling toughness. The smaller and larger mechanical serial sectioned datasets required at least 15 to 25 days of manual labor exclusively for the collection of serial sections [133]. The 3D FSLSS measurements are listed along with the two mechanical serial sectioned datasets collected by Chan *et al* in Table 5.2. Mechanical SS dataset 1 has a significantly higher volume fraction and particle size due to the low imaging and sectioning resolution of the dataset, which resulted in a poor segmentation [133]. Mechanical SS dataset 2 has a higher imaging and sectioning resolution, and the volume fraction, particle sizes, and nearest neighbor distances are more similar to the FSLSS and 2D stereology data. The FSLSS and 2D stereology datasets were collected from the same double-linear shear bar test specimen, but from different local sampling locations. The Mechanical SS datasets were collected from a material with similar nominal composition, but with different forging conditions. The sectioning and imaging resolution have an impact on the quality of the segmentation and the smallest resolvable particle size. The variance in local nearest neighbor spacing, volume fraction, and mean particle size can be explained by (1) the local sampling area, and variation in microstructure, and (2) the quality of the segmentation, which is a function of the imaging and sectioning resolution. In Section 5.2, the variability in the FSLSS data is discussed in detail.

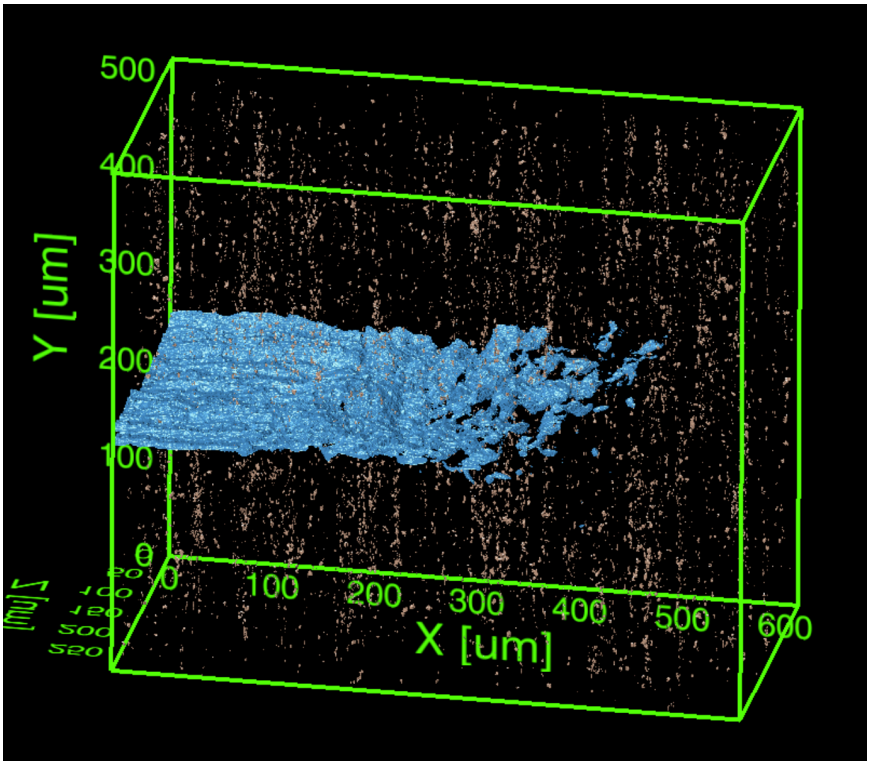

Figure 5.11: A 3D reconstruction of a mechanically serial sectioned dataset collected by S. Chan (Northwestern Univeristy) and D. Rowenhorst (NRL). The sample is taken from the process zone in a 4330 steel from an interrupted compact tension sample. The blue region is a crack propagated during the compact tension test and the yellow particles are TiN. A 4330 steel was analyzed with similar composition and processing conditions to the materials used in this thesis. The height of the plastic zone was estimated to be 112 µm, on average, while the extent of the plastic zone ahead of the crack was measured to be 73 µm.

5.9 Modeling of Toughness in 4330 Steel

The 4330 steel discussed in 2.2.2 has been used as an example system to show the capabilities of the FSLSS technique, combined with some simple toughness models and statistical analysis. The objective was to collect 3D microstructural information that is influential in the ductile fracture process. The microstructural features of most importance for crack propagation are the cuboidal TiN phases discussed in 2.2.2. As discussed in 5.2.6 the TiN particle parameters such as distribution, size, volume fracture, and nearest neighbor spacing are most important because they can

be directly input into existing toughness models.

The approach taken for modeling toughness in this steel alloy is as follows:

1. Sample 3D volumes from various locations in the material of interest using the FSLSS technique.

2. Sub-sample the FSLSS 3D datasets with equal volumes of size that is proportional to the region of plasticity ahead of a crack tip.

3. Statistically analyze sub-sampled volumes to determine the microstructural parameters relevant to ductile fracture.

4. Calculate toughness of sub-sampled volumes using existing models.

5. Perform Weibull analysis to compare the distribution of sampled toughnesses to literature toughness values and variability.

Schematically, the sub-sampling of the FSLSS datasets is shown in Figure 5.12. Six FSLSS collected datasets have been sub-sampled (eight from each dataset) into 48 volumes of $100 \times 100 \times 48\,\mu m$. In section 5.9.1, the justification for selected the size of the sampled volume will be discussed. The sub-sampled volumes are approximated to be the size of the plastic zone, the region of high stress concentration surrounding a propagating crack tip.

5.9.1 Plastic Zone

Ahead of a propagating crack tip, there is a region of highly localized stress concentrations termed the plastic zone. In plane-strain conditions, hydrostatic forces produce high triaxial stress states, particularly at the center of the specimen. Typically, in a compact tension sample, this region of high triaxially will correspond with the area surrounding the propagating crack. The hydrostatic stresses have been shown to aid in slowing void growth from inclusion particles [78, 151], this aside, the

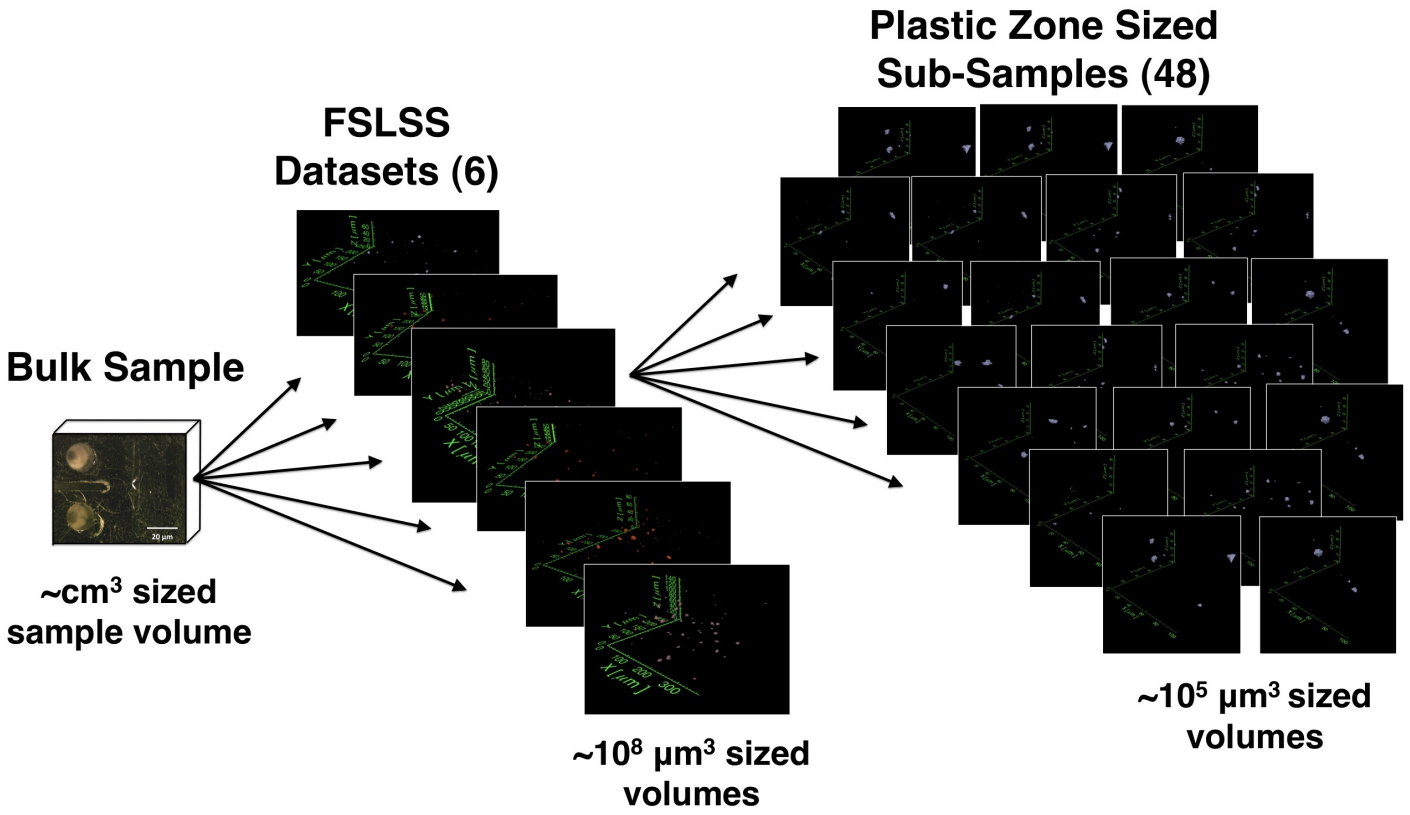

Figure 5.12: Schematic showing the method of sampling using the FSLSS technique to analyze the titanium modified 4330 steel. Six FSLSS datasets are collected each having volume in the range of $\sim 10^8\,\mu m^3$. Each of the six FSLSS datasets is sub-sampled into eight plastic zone sized regions having volumes on the order of $\sim 10^5\,\mu m^3$. These 48 sub-sampled regions have then been used as a statistical volume elements (SVE) of different representative spatial distributions of TiN particles that exist in the original bulk 4330 steel specimen. This SVE has been used to calculated toughnesses of these distributions as they would exist provided a bulk sample had a distribution of particles similar to those found in the sub-sampled SVE region.

interacting microstructure in the localized region ahead of a crack tip is the most highly stressed and influential volume for modeling toughness [137, 139, 161].

There are a number of calculations that have been made to estimate the size of the plastic zone. These estimates include the linear elastic fracture mechanics derivations for the extent of plastic yielding in both plane strain (equation 5.29) and plane stress (equation 5.30) conditions [139]. Both of these equations are evaluated for $\theta = 0$, or the extent of plasticity in front of the crack tip. For more a precise description of the full shape of the plastic zone shape in 2D, a derivation with the included θ dependence is described in [137, 139].

$$r_{p,\epsilon} = \frac{1}{6\pi}(\frac{K_{IC}}{\sigma_y})^2 \tag{5.29}$$

$$r_{p,\sigma} = \frac{1}{2\pi}(\frac{K_{IC}}{\sigma_y})^2 \tag{5.30}$$

Rice and Johnson [161] formulated a plastic zone size calculation with a maximum (at $\theta = 70°$) and minimum (at $\theta = 0°$) extent of yielding described in equations 5.32 and 5.31. Their calculations include modified stresses based on a work-hardening material that follows power law hardening of the type: $\tau = \tau_0(\frac{\gamma}{\gamma_0})^N$, where τ_0 and γ_0 are the stress and strain at yield, and N is the hardening exponent.

$$r_p^y = 0.175(\frac{K_{IC}}{\sigma_y})^2 \tag{5.31}$$

$$r_p^y = 0.032(\frac{K_{IC}}{\sigma_y})^2 \tag{5.32}$$

Another method for estimating the plastic zone size is to directly measure it from a mechanically tested specimen. In Figure 5.11, a mechanically serial sectioned 3D reconstruction of an interrupted compact tension 4330 steel sample collected by Chan

et al is shown [133]. The process zone was serially sectioned in order to capture the curvature of the propagating crack, the relative size of the plastic zone, and void-inclusion particle relations (the void-growth ratio: $\frac{V_c}{V_I}$). Chan estimates the plastic zone, for mode I testing, to be $\sim 112\,\mu m$ vertically and to extend $\sim 73\,\mu m$ ahead of the crack tip.

The number of interacting particles near a propagating crack tip can be estimated by comparing the plastic zone size with the geometric parameters characterizing inclusion spacing and size. Figure 5.13 shows a schematic of the parameters available by the FSLSS technique and how they can be compared with the plastic zone size.

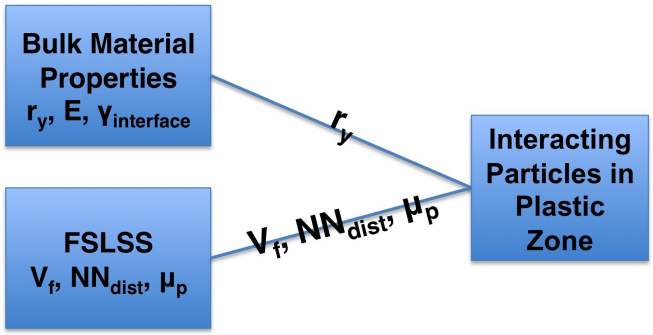

Figure 5.13: Variables available from the FSLSS technique that dictate the number of interacting particles in the plastic zone. The plastic zone size is calculated from material properties. Indicators of particles size, spacing, and density will define roughly how many interacting particles can fit within the plastic zone.

The calculations and measurements of the plastic zone size provide reasonable estimates for the size of the interacting volume ahead of the crack tip. In the next section 5.9.2 and 5.9.3, the calculated volumes will be considered to determine the sampling volumes necessary to accurately model the fundamental microstructural interactions for predicting toughness and for acquisition of 3D datasets.

5.9.2 Representative Volume Elements

A common problem with tomography is developing an understanding of how large of a dataset is necessary to accurately represent specific properties of a material. The idea of a representative volume element (RVE) was developed by Hill [179]. An RVE defines the size of a subset of microstructure which will on average represent the material and properties of interest. The RVE can often fluctuate in size depending on the structural properties being modeled. For instance, if one were interested in properties that are mostly affected by microstructure with a µm-sized features, then the RVE would most likely need to include enough of these features to statistically represent the bulk material. Yin *et al* [147] characterize an RVE as satisfying the relation in equation 5.33:

$$L >> l >> d \tag{5.33}$$

Where L is the characterization length of the macroscale, l is the size of the RVE at the intermediate mesoscale, and d is the characteristic lengthscale of the microstructure necessary for modeling the material property of interest. Often, it is difficult to determine just how large an RVE needs to be. Iteratively, the size of the RVE can be increased and a measures of material properties can be modeled until the RVE's properties match with the bulk material properties.

Computationally, many 3D datasets become too complex to model at their full volumetric sizes. Furthermore, properties that strongly depend on extreme values or statistical outliers, such as fatigue crack initiation or ductile fracture can require extremely large volume RVEs. In these cases, alternate representative volume element approaches have been developed for models and acquisition size estimation. Therefore, smaller sub-sampled volumes are extracted from larger 3D datasets to build groups of statistically relevant samples that, when collectively analyzed, correctly

predict bulk material properties.

Such samples are referred to as a statistical volume elements (SVE), and require that an amount of these SVE's are collected with the microstructurally pertinent features represented so that the aggregated collection will correctly model bulk material properties. SVE's are required to have size scaling that is described by equation 5.34:

$$\rho = \frac{l}{d} \tag{5.34}$$

Where ρ is the ratio of l, the size of the mesoscale RVE and d, the characteristic length scale of the microstructure. McDowell *et al* [180] and Groeber *et al* [181–183], have analyzed SVE and statistically equivalent representative volume elements (SERVE). They have developed sampling software for generation of statistically equivalent SVEs from calibrated RVEs, allowing them to generate synthetic representative datasets.

Using the definition of SVE presented by [184], for the example of 4330 titanium modified steel, the relevant lengthscale d for toughness modeling is 1-10 µm, so for a ρ value of 10, an SVE size of l should be ~ 100 µm. In other words the SVE has a characteristic lengthscale of 10-100 times the lengthscale of the TiN particles important for modeling toughness.

There are a number of tools used to evaluate the degree to which a tomographically acquired 3D dataset represents the analyzed material. There are a number of one-point numerical indicators which can be evaluated for similitude with other acquisition techniques. For instance, specific volume fractions of phases can be compared for numerous methods (ie. FSLSS, mechanical serial sectioning, 2D stereology). More rigorous approaches have been developed such as two-point statistics [185]. An example of two-point correlation functions would be the distribution of particle-to-particle distances. Statistical analysis of both FSLSS datasets and the mechanically serial sectioned datasets were performed using IDL software developed by H. Jou

(QUESTEK) [178].

5.9.3 FSLSS Modeling Analysis

A set of six FSLSS datasets were collected as a representative volume of the bulk 4330 steel, the statistical measurements and datasets information is contained in Table 5.3.

Table 5.3: Table of size and statistical information related to datasets collected using the FSLSS technique. Smaller sample volumes (SVEs) were extracted from these datasets.

Dataset	X_{size} (µm)	Y_{size} (µm)	Z_{size} (µm)	N_{TiN}	δ_{TiN} (#/m^3)	μ_{TiN} (µm)	NN_{dist} (µm)	$V_{f,TiN}$ (%)
1	404	302	78	101	1.09E+13	2.06	18.08	0.022
2	404	302	54	44	7.02E+12	2.78	25.17	0.019
3	404	302	149	466	2.01E+13	1.21	3.11	0.044
4	314	156	89	124	2.85E+13	2.12	9.97	0.028
5	404	302	55	88	1.43E+13	1.74	13.04	0.029
6	404	302	46	65	1.19E+13	2.49	19.37	0.052

A set of 48 (8 from each of 6 datasets) SVE's were extracted from the 4330 steel datasets collected using the FSLSS technique, shown schematically in Figure 5.12. The size of these SVE's was determined using the following steps. First, the plastic zone was estimated using equations that follow the relation described by 5.35 [186]. Depending on the calculation used, r_p values range from 75-385 µm. The plastic zone was experimentally measured to have a average height of 112 µm and a plastic zone ahead of the crack tip of 73 µm, in a mechanically sectioned 3D dataset of a differently processes 4330 material, shown in Figure 5.11 [133]. The plastic zone size gives a measure of the size of the area experiencing the highest levels of triaxiality and stress concentrations in the path of a propagating crack. Therefore, the interaction volume of the plastic zone dictates the number of TiN particles likely to be directly interacting in local void formation and linkup, critical steps in ductile fracture and

crack propagation. The calculations of r_p (section 5.9.1) from plastic zone equations and the 3D plastic zone size measurements suggest the size of SVE's necessary to accurately model toughness parameters in the vicinity of a crack tip.

$$r_y \approx K_c^2 \pi \sigma_y^2 \tag{5.35}$$

The 6 primary FSLSS samples were collected from a $1 \times 1 \times 3\,\text{cm}$ double-linear shear bar test specimen grip section, as shown in Figure 5.12. The 6 FSLSS datasets collectively are representative of a volume of size $\sim 10^8\,\mu\text{m}^3$, which has the aggregate sampling of 6 different local microstructral volumes. The 48 subsampled regions are representative of $\sim 10^5\,\mu\text{m}^3$, which is the approximate size of the crack-tip plasticity zone, r_p.

A total of 48 SVEs of size $100 \times 100 \times 46\,\mu\text{m}$ were sampled from unique regions within the datasets shown in Table 5.3. These volumes were analyzed statistically, reconstructed, and visualized. Statistical measures were made using the same code applied to the full size datasets collected using the FSLSS technique [178]. The mean-particle size, the volume fraction, and the 3D nearest neighbor particle spacings have been extracted from the sampled datasets in order to model their interactions and influence on toughness in the plastic zone sized volumes.

Two different models were used to calculate K_{IC} and J_{IC} toughness parameters from the 48 sub-sampled datasets, these are the Wang-Olson toughness model [133] and the Garrison-Moody toughness model [187].

The Garrison-Moody model is a relates K_{IC} to void fraction parameter R_v/R_I, the 3D nearest neighbor spacing X_0, and the yield stress σ_{ys}, and Young's Modulus E, shown here:

$$K_{IC} = \sqrt{\frac{\pi}{4} E \sigma_{ys} X_0 (\frac{R_v}{R_I})} \tag{5.36}$$

The Wang-Olson phenomenological model relates J_{IC} normalized by the yield stress σ_{ys} and the 3D nearest neighbor distance X_0 to a constant J_p, the void growth ratio $\frac{V_c}{V_0}$, and a hardening exponent n_v, shown here:

$$\frac{J_{IC}}{\sigma_{ys} X_0} = J_p (\frac{V_c}{V_0})^{n_v} \tag{5.37}$$

The Garrison-Moody and the Wang-Olson models both relate nearest neighbor spacing and the void growth ratio to toughness, but each model has been calibrated with different steel inclusion data, resulting in different hardening exponents and constants (such as J_p).

Both of the toughness values calculated by these equations can be converted from J_{IC} to K_{IC} by using the following relation:

$$K_{IC}^2 = \frac{J_{IC} E}{(1 - v^2)} \tag{5.38}$$

where v is Poisson's ratio. The toughness values can then be fit to a two-parameter Weibull distribution, where the probability density function (PDF) is defined by the following equation:

$$PDF = (\frac{m}{J_0})(\frac{J_{IC}}{J_0})^{m-1} exp(-(\frac{J_{IC}}{J_0})^m) \tag{5.39}$$

and cumulative density functions equation (CDF) is:

$$CDF = 1 - exp(-(\frac{J_{IC}}{J_0})^m) \tag{5.40}$$

where J_0 (or K_{IC} for the Garrison-Moody model) is the scale parameter of the distribution and m is the Weibull shape parameter. The probability of occurrence F of a specific toughness values is defined as:

$$F = \frac{n - 0.5}{N} \tag{5.41}$$

where n is the sorted rank of the sampling out of N the total number of samples. By plotting $log(log(1-F))$ by the log(toughness(J_{IC} or K_{IC}) we can directly calculate the Weibull slope m and obtain a visual inspection of the goodness of fit.

Using the Wang-Olson toughness model, the CDF and PDF of the data is plotted in Figure 5.14 and Figure 5.15. In Figure 5.14, the closed circles represent the modeled toughness values and the solid line is the Weibull CDF fit. The mean J_{IC} value is 0.089 MPa(m) and the median is 0.064 MPa(m), which can be converted, respectively, to K_{IC} values of 139.9 MPa(m)$^{1/2}$ and 118.6 MPa(m)$^{1/2}$.

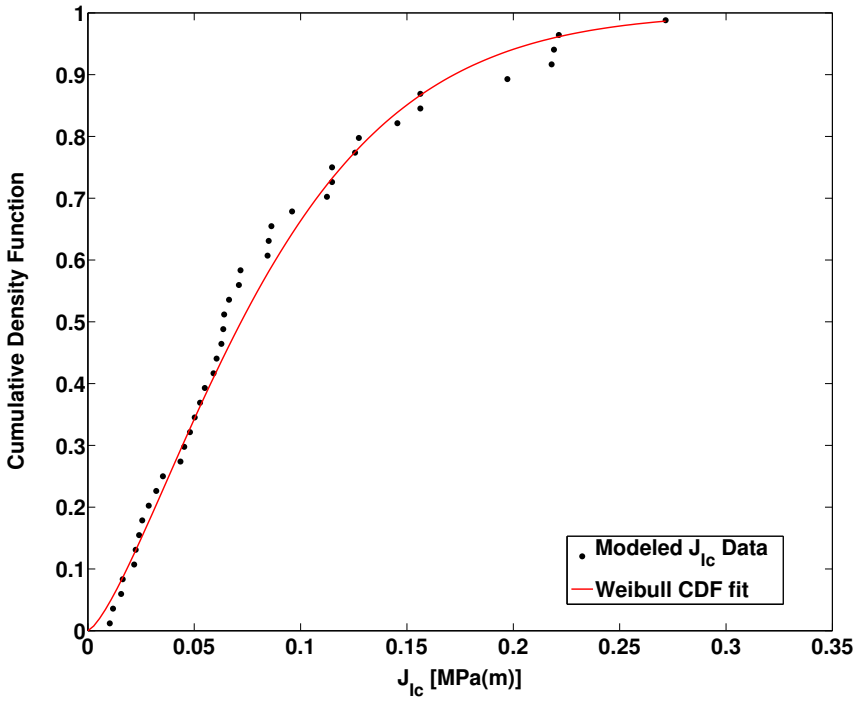

Figure 5.14: J_{IC} values predicted using the Olson-Wang toughness model (closed circles) plotted versus their relative cumulative density. A two-parameter Weibull fit is also shown (solid line). The mean J_{IC} value is 0.089 MPa(m), the median is 0.064 MPa(m).

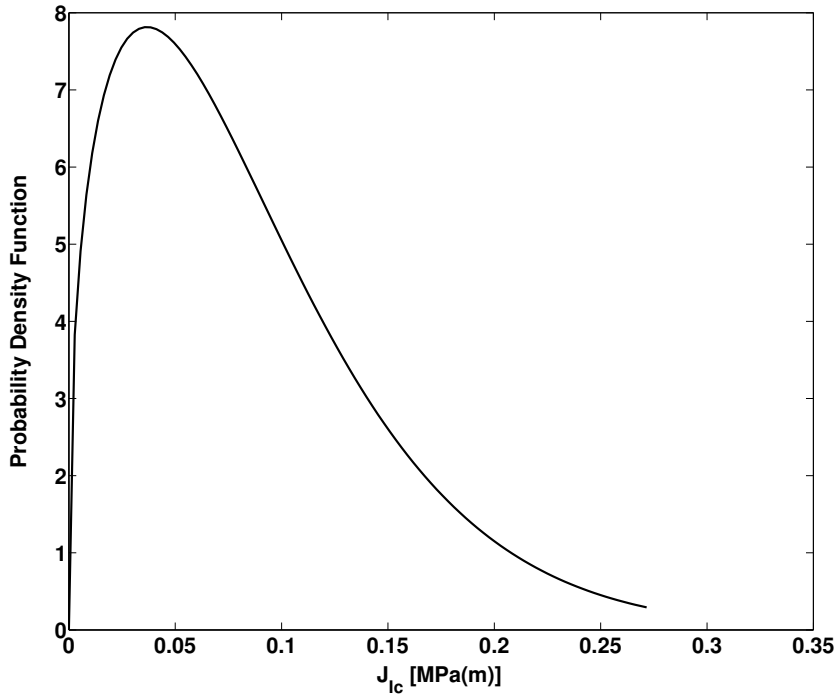

Figure 5.15: J_{IC} values plotted against their relative probability densities according to the two-parameter Weibull fit.

The Weibull distribution plot, Figure 5.16, shows the J_{IC} toughness model value data plotted against the probability of occurrence. The distribution has a Weibull modulus m of 1.4 and J_0 scale parameter of 0.094 MPa(m). The modulus is a measure of variability for the material parameter plotted, in this case, the toughness.

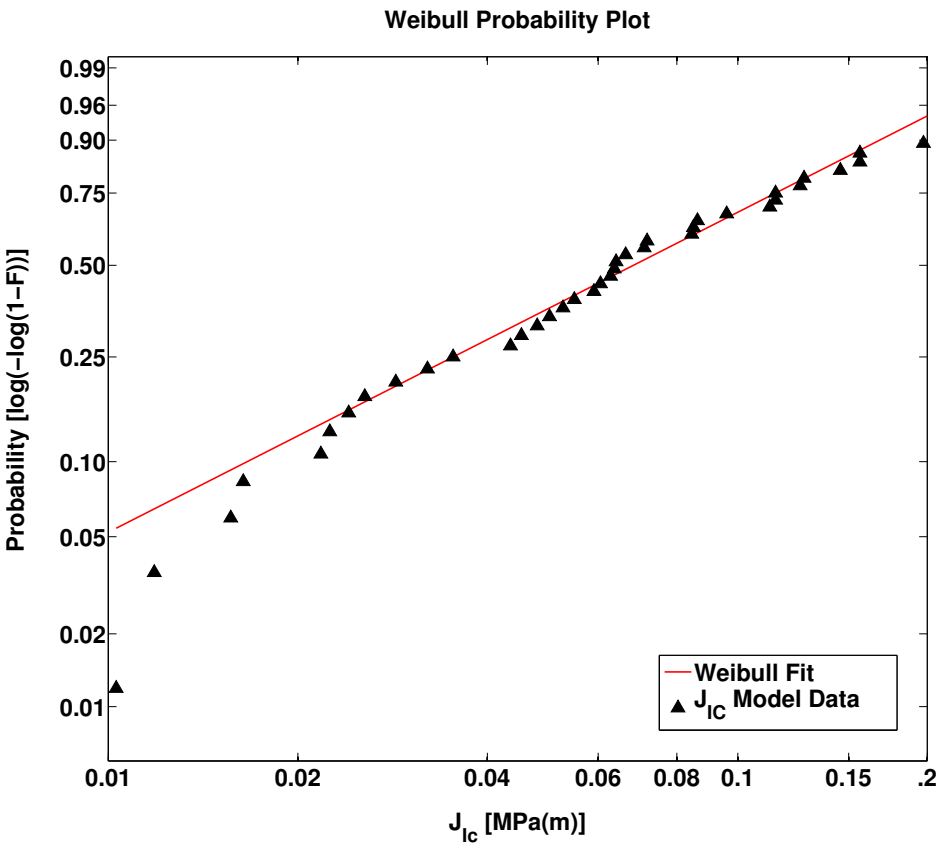

Figure 5.16: Weibull plot of J_{IC} values and their relative probability of occurrence. A Weibull modulus, the slope or shape parameter, of the fit is 1.4 and the J_0 fitting value, or scale parameter, is 0.094 MPa(m). The variance of the data is indicated by the Weibull modulus and is in good agreement with toughness measurements made in bulk specimens by Ruggieri [188].

Using the Garrison toughness model, the CDF and PDF of the data is plotted in Figure 5.17 and Figure 5.18. In Figure 5.17, the closed circles represent the modeled toughness values and the solid line is the Weibull CDF fit. The mean K_{IC} value is 64.7 MPa($m^{1/2}$), the median is 59.4 MPa($m^{1/2}$).

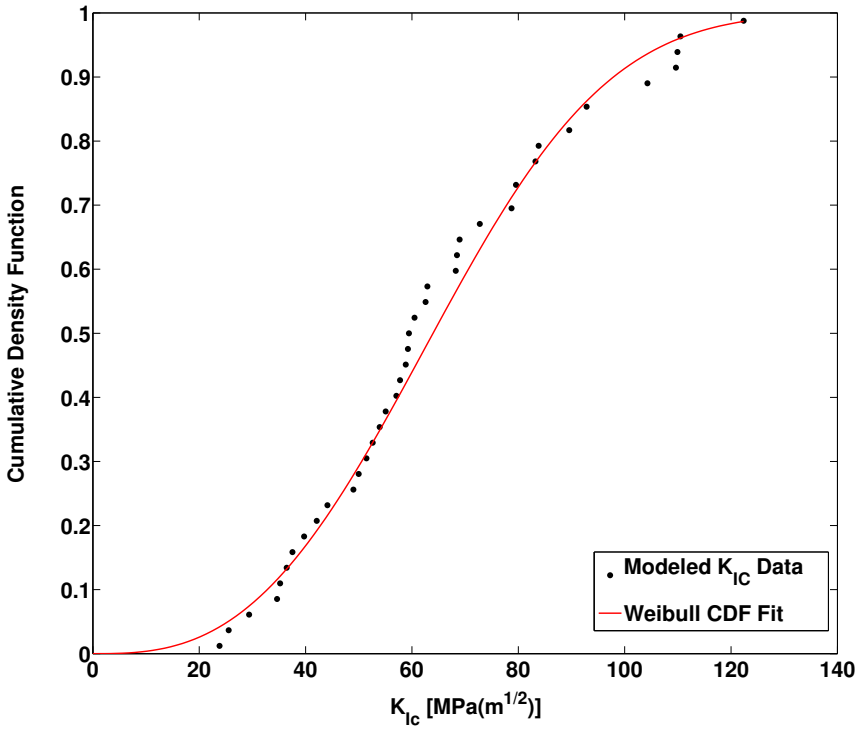

Figure 5.17: K_{IC} values predicted using the toughness model (closed circles) plotted versus their relative cumulative density. A two-parameter Weibull fit for the cumulative density function is also shown (solid line). The mean K_{IC} value is 64.7 MPa($m^{1/2}$), the median is 59.4 MPa($m^{1/2}$).

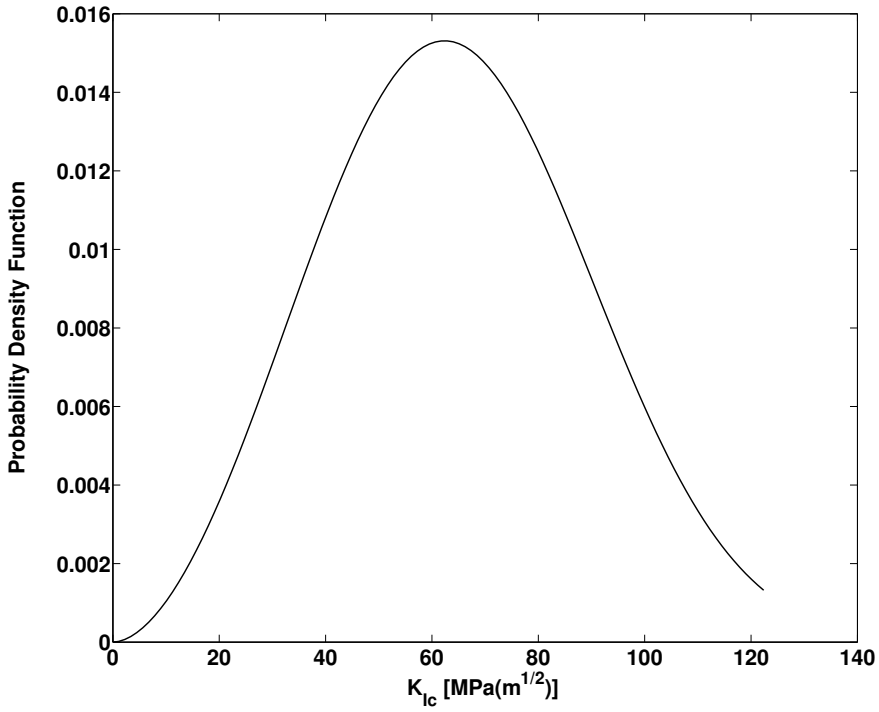

Figure 5.18: K_{IC} values plotted against their relative probability densities according to the two-parameter Weibull fit.

The Weibull distribution plot, Figure 5.19, shows the J_{IC} toughness model value data plotted against the probability of occurrence. The distribution has a Weibull modulus m of 2.8 and J_0 scale parameter of 72.8 MPa($m^{1/2}$). The modulus is a measure of variability for the material parameter plotted, in this case, the toughness.

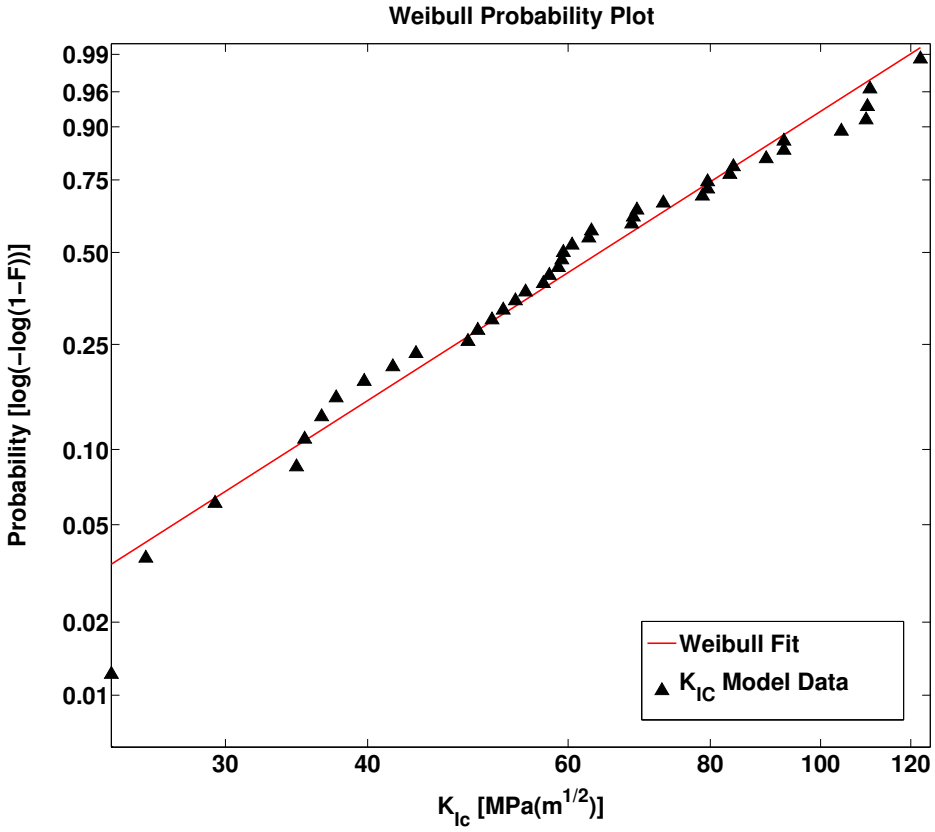

Figure 5.19: Weibull plot of K_{IC} values and their relative probability of occurrence. A Weibull modulus, the slope or shape parameter, of the fit is 2.82 and the K_0 fitting value, or scale parameter, is 72.8 MPa($m^{1/2}$). The variance of the data is indicated by the Weibull modulus and is in close agreement with works by Ruggieri [188].

The results of the Weibull statistical analysis are significant because of the following. The modulus m, or slope, of a Weibull plot represents the degree of variability in the material property (toughness) related to the probability of its occurrence. The J_{IC} values calculated using the Wang-Olson model showed a variability, in m, the Weibull Modulus, very similar to those measured in 22 bulk sample toughness experiments performed by Wiesner [189] and analyzed by Ruggieri [188]. Ruggieri measured m values of 1.4 and 1.5 for two sets of 11 ferritic C-Mn steel specimens. The m values from Ruggieri are very close to the m of 1.4 measured using the FSLSS technique and J_{IC} toughness modeling. A similar Weibull analysis was used for the 48 sub-sampled

datasets collected using the FSLSS technique. J_{IC} toughness values were calculated from both the Wang-Olson model and the Garrison-Moody model and plotted with the toughness data from Ruggieri [188] in Figure 5.21. The K_{IC} toughness modeled using the Garrison-Moody equations have a Weibull modulus m of 2.82 . Since K_{IC} is related to J_{IC} by $K_{IC}^2 = \frac{J_{IC}E}{(1-\nu^2)}$, it seems logical that the modulus will have roughly a power of two dependent on the J_{IC} modulus (or $\sim 1.5^2$). The Ruggieri bulk toughness specimens were measured below the ductile to brittle transition temperature, in the brittle regime, suggesting that there may be less variability in the data then if toughnesses were measured at higher temperatures.

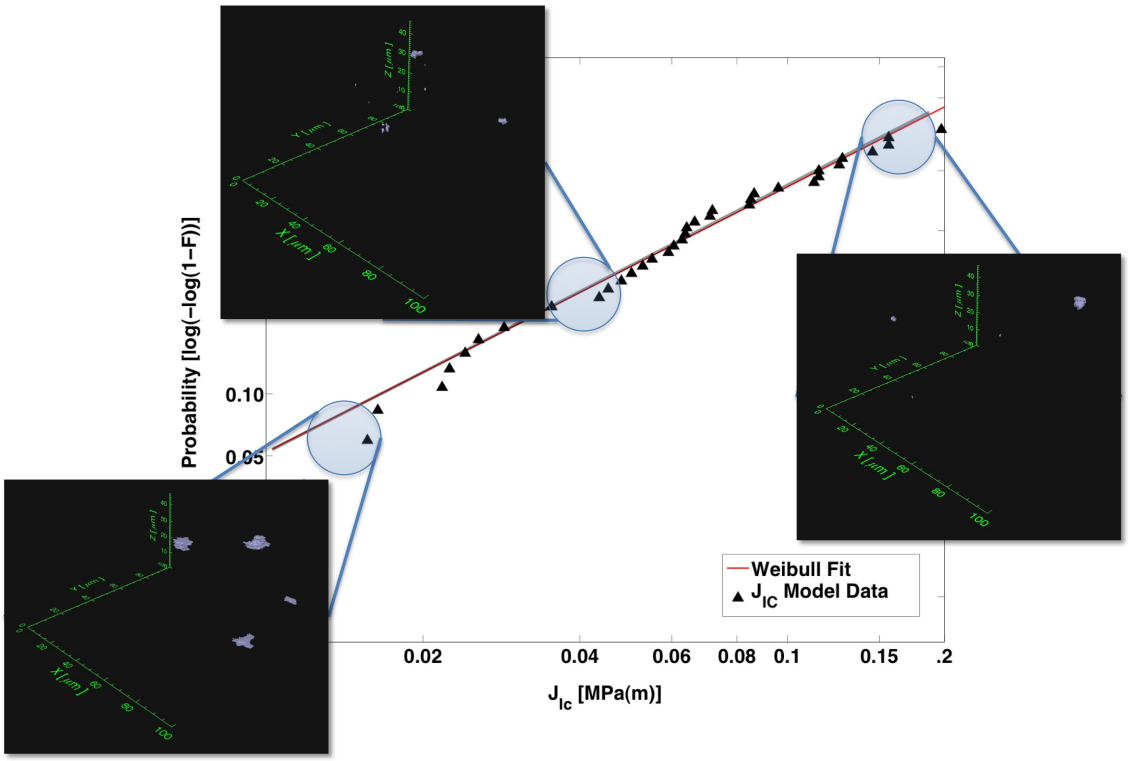

Figure 5.20: Weibull plot of J_{IC} values and their relative probability of occurrence. 3D reconstructions of sub-sampled regions corresponding to the blue circled regions are shown relative to their toughness values. The minimum and average toughness values are important for modeling failure criteria in bulk structural material, suggesting that detailed toughness models for these sub-samples would help understand why these regions are limiting the overall toughness of the material.

In modes of failure such as fatigue and ductile fracture, the extreme distribution values are of most importance for design. This is because the weakest local volumes or the single largest flaw tend to dictate the overall property of the bulk material. In a 4330 steel a high concentration of defects, such as a cluster of TiN particles, will significantly enhance crack propagation and lower the toughness of the bulk specimen. Therefore, when characterizing fracture toughnesses, it is important to sample the material in a way to obtain a representative RVE. In Figure 5.20, a Weibull distribution showing toughness related to the relative probability has 3D reconstructions overlaid corresponding to the toughness minimum, average, and maximum values. In the case of ductile fracture, the average and minimum values dictate the macroscopic toughness of the material. For this reason, detailed finite element modeling of the minimum and average subsamples would be useful to characterize local microstructures that are favorable or unfavorable for toughness.

The methodology used to investigate the 4330 steel using the FSLSS technique to collect 3D microstructural data proves to be useful for the following reasons. (1) The FSLSS technique allowed the sampling from a relatively small volume of material ($1 \times 1 \times 3\,\mathrm{cm}$) and correctly capture the variation in toughness using the Weibull distribution and a simple toughness model. (2) Since volumes can be collected from numerous locations at high throughput, macroscopic variations in microstructure due to processing conditions are more likely to be characterized. (3) The toughness distribution obtained by collection of many SVEs, in this case, is equivalent to the mechanical testing efforts of 22 bulk specimens. Further validation of this approach in other materials systems is needed.

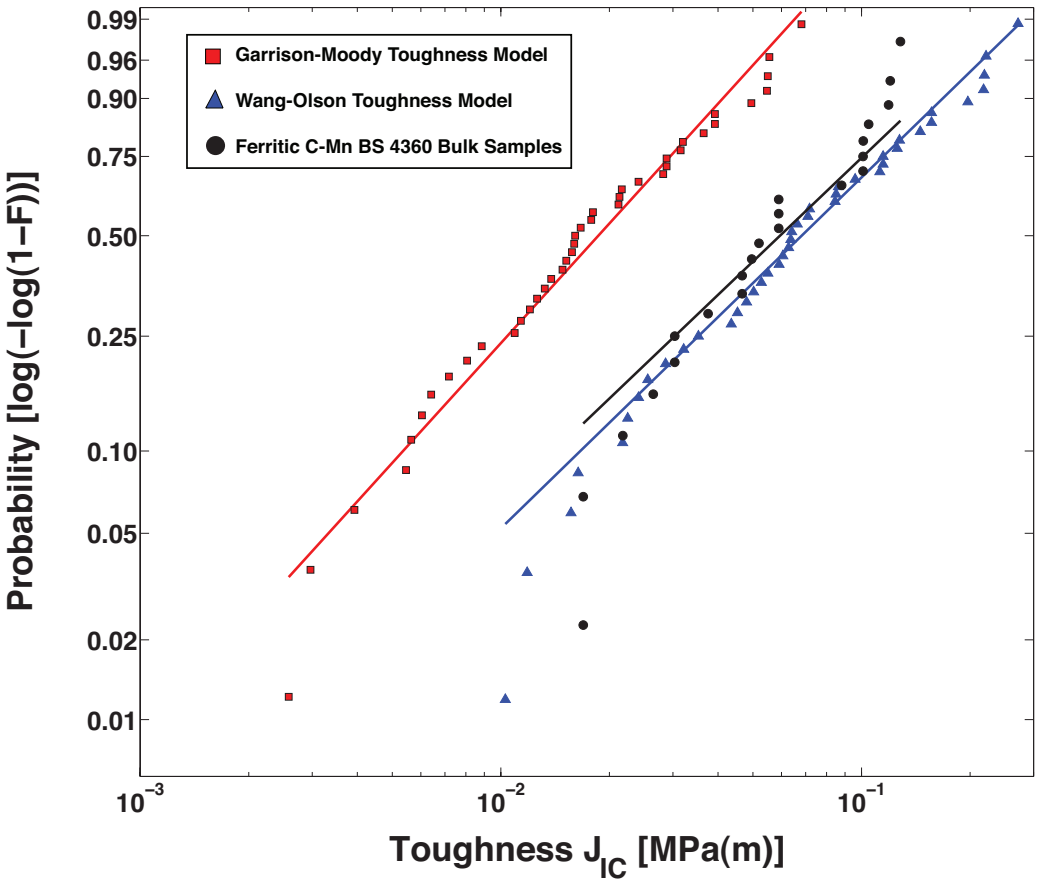

Figure 5.21: Weibull plot of J_{IC} values and their relative probability of occurrence extracted from the Wang-Olson and Garrison-Moody models, as well as bulk ferritic C-Mn steel toughness data from Ruggieri [188]. Weibull modulus m values for the three datasets are respectively: 1.4 , 1.41 , and 1.4-1.5 .

5.10 Multimodal Data Collection

FSLSS is a destructive technique, meaning that material is consumed as it is quantified, and therefore is motivation for the collection of as much information as possible or multi-modal data for each section. Additionally, multimodal data can increase the fidelity of the image segmentation process. The femtosecond laser produces a large amount of ionized particles (plasma) during the ablation event and in turn these decaying particles emit photons with characteristic wavelengths at their related

energies. The characteristic wavelengths emitted are analyzed using a spectrometer to identify the elemental constituents of the ablated material. The incorporation of the spectroscopic data into FSLSS is currently being explored. In Figure 5.22, high intensity ionization peaks for iron and titanium are identified for their K1 shell electrons. There are redundant strong peaks for titanium, of which one is selected and monitored for intensity change. Much greater concentrations of titanium are found in the TiN particles than in the matrix, providing a mechanism for contrast in relative intensity between the two phases. The resolution of this technique is equal to the spot size of the laser, which is currently 57 µm. In order to incorporate additional imaging mode into the current technique, the spot size of the laser would have to be adjusted, using different optics, to be of a similar size to the microstructural chemical features of interest.

Multimodal data collection is beneficial because it can provide more information about microstructure, for instance local chemistry can be collected using X-ray techniques, grain orientation can provide structural information using backscattered electrons, and optical images or scanning electron images can provide topological information. Since most sectioning methods are destructive, there is a strong motivation to collect as many types of information as possible so that a more detailed analysis can be performed later. Datasets collected with multiple types of information (mutual information) for each slice improves the accuracy of image segmentation and image registration by using the joint histograms method [190]. New approaches for the collection of multimodal datasets are discussed in Chapter VI.

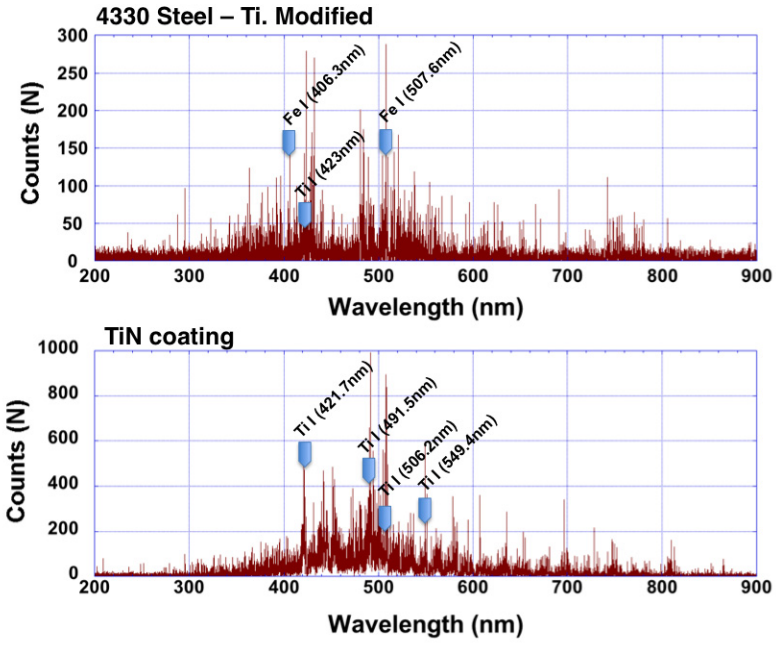

Figure 5.22: Spectroscopic data for titanium modified 4330 steel and a TiN coating. Ionization states with high relative intensity for elements of pertinence are demarcated with arrows and labeled with their wavelength.

CHAPTER VI

TriBeam System - High Resolution, Multimodal FSLSS

The next step in laser based serial sectioning was to integrate the system into an electron microscope for higher resolution and for implementation of advanced detectors for multi-modal data acquisition. Modern electron imaging and X-ray imaging techniques require a vacuum for efficient transmission of waves and particles without signal degradation, therefore the femtosecond laser beam needed to be delivered inside a vacuum chamber. In this chapter, the system components will first be described in detail, then calibration, setup, and methodology will be discussed, followed by preliminary in-situ laser machining examples and sectioned data.

6.1 Tri-Beam System

During the course of the development of the FSLSS technique, it became clear that using a femtosecond laser as a material removal tool could be advantageous for the collection of 3D data using many different types of detectors or imaging techniques. The femtosecond laser has proved to be a unique tool for the µm-scale modification of materials due to its low peripheral damage and impressive material removal rates, leaving room for improvements and variety in the types of image collected. The

Tri-Beam system was primarily designed as a tool for combined laser and FIB serial sectioning with multiple detectors for advanced imaging capabilities. The FIB and laser beam remove material at well-characterized rates in evacuated environments. Under vacuum, radiation propagation is enhanced compared to open-atmosphere, enabling the use of chemical imaging, grain orientation detectors, scanning electron, and ion detectors. Furthermore, the Tri-Beam system can be used for micromachining with removal rates 4 to 6 orders of magnitude faster than a FIB. The Tri-Beam is an collection of several components which have been fully integrated to augment the capabilities of a DualBeam FIB/SEM. A schematic of the instrument is provided in Figure 6.1. In the proceeding sections a brief overview of the tool, its components, and its operation is reviewed.

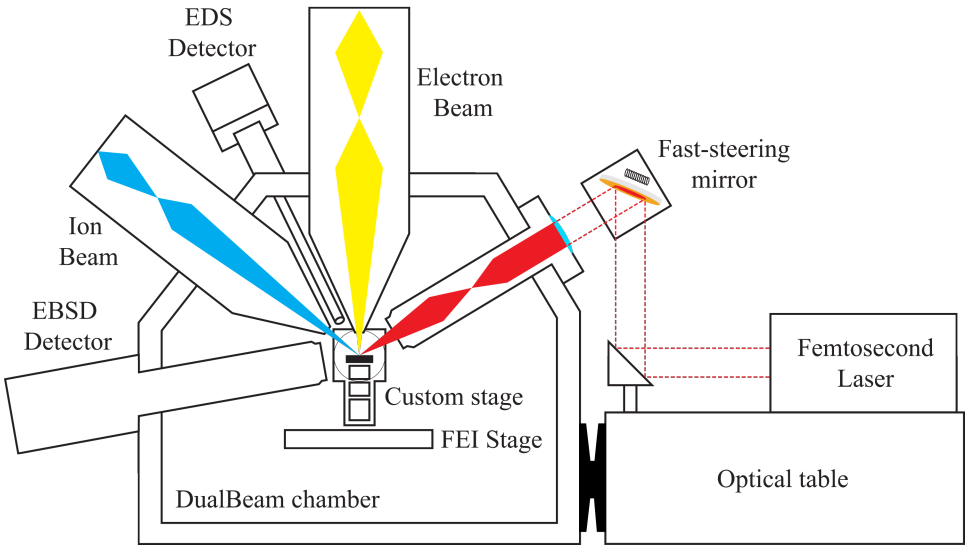

Figure 6.1: Schematic of the Tri-Beam system.

6.2 Hardware Components

Integration of the femtosecond laser into the existing Dualbeam FIB chamber required a number of engineering steps necessary to provide beam control, beam delivery, beam stability, sample tilt control, and three beam convergence or eucentricity.

The individual components and their function are described in the following sections

6.2.1 DualBeam FIB/SEM

A DualBeam™ FIB/SEM is a tool that combines a scanning electron microscope (SEM) with a focused ion beam (FIB). This tool has the capability to image with both electrons and ions at resolutions as low as 3 nm and 7 nm, respectively [191]. Additionally, the FIB can be operated at higher currents in order to remove material from the sample surface. Therefore, DualBeam™ instruments have already been shown to be apt for the collection of 3D data via a serial sectioning approach [3, 29, 39, 44, 192]. However, the application of DualBeam™ instruments to collect 3D data is limited by the material removal rate of the FIB. The DualBeam™ used for this work is a FEI Strata™ DB 235. The electron column is equipped with both through-lens secondary electron and backscatter electron detectors and out-of-lens secondary electron and secondary ion detectors. The center of tilt of the Strata DB 235 stage (eucentric height) and the intersection point of the two beams coincide at a 5 mm working distance from the pole piece of the SEM column. The Strata DB 235 has a five-axis positioning stage (x, y, z, rotation and tilt). The tilt range is restricted to the range between -15° to 52° and the other four axes (x, y, z and rotation) move with the tilt plane. Furthermore, the tilt axis diverges from the exact eucentric height between 25° and 40°.

6.2.2 Femtosecond Laser

A Clark-MXR™ CPA-2110 femtosecond laser is the source of the third beam in the TriBeam instrument. This is a similar updated model laser as was used in open-atmosphere tomography described as the FSLSS technique [175]. The CPA-2110 has an average power of 1.2 W, 1 kHz repetition rate, 780 nm wavelength, and uses a Ti-sapphire crystal as the primary gain medium. Femtosecond lasers are used to ablate

material with low amounts of collateral damage [99] and a negligible heat affected zone [193]. These impressive ablation characteristics are attributable to the ultra-short pulse widths (120 fs) and high focused intensity ($> 10^{18} W/cm^2$). Femtosecond lasers have been used for low-damage micro-machining in a number of materials system [82, 89, 95, 104, 109, 117, 123, 126, 193, 194] with well-characterized material removal rates from single pulse laser studies [88, 99, 101, 102, 114, 120]. The unfocused output beam measures 10 mm in diameter.

6.2.3 Optical Setup

A stable platform is necessary to accurately deliver the laser beam into the chamber and to obtain high resolution images. The Strata™ DB 235 chamber is mounted on top of an active air suspension system to isolate it from vibrations. When the chamber is vented, the air suspension is deflated and it comes to rest on stationary stops. With the chamber under vacuum to operate beams and detectors, the active air suspension system inflates for vibration isolation. The laser and beamline are mounted on an optical table, which has active air suspension vibration isolators. A rigid bracket bolted between the edge of the table and the largest flange on the side of the chamber structurally ties the two together. Separate air suspension systems for the vacuum chamber and optical table work in unison to automatically raise and lower the system via software control. A pressure adjustable pilot actuated 3-way valve connects the two pressurized air circuits of the optics table and vacuum chamber. The chamber air suspension pressure is connected to the pilot actuator of the valve. A separate regulated pressurized air source is connected to the supply port of the 3-way valve with the output port delivering pressurized air to the suspension system of the optical table. To coordinate movement of the chamber and table suspensions, adjustments of the two independent pressure regulators and the trigger pressure of the pilot operated valve were performed. Therefore, the chamber and optical table are

physically and pneumatically connected, raising and lowering together as a unit each time the DualBeam™ chamber is evacuated and vented.

6.2.4 Optical feed-through port

The optical feed-through assembly is a laser-transparent window that maintains a hermetic seal with the DualBeam™ chamber while allowing translational and axial movement (see Figure 6.2). Translational movement is necessary for laser beam alignment to the intersection point of the electron beam and focused ion beam. This is achieved by pressing a preloaded sliding plate onto an o-ring, preventing leakages and deflections at all possible vacuum pressures. Axial movement (normal to the plane of the feed through port) is necessary for focusing the laser onto the surface of the sample. This is achieved by sliding the inner optical tube inside the outer guide tube, using an o-ring to maintain a tight seal. One end of the objective tube is inside the chamber and has a thread-mounted objective lens. The opposite end of the objective tube is outside the chamber and has a sealed fused quartz window attached to it to maintain vacuum. This end also has a threaded adjustment nut that may be used for fine axial adjustments to the objective tube and therefore adjustment of the beam focus from outside the chamber.

The femtosecond laser beam is delivered to the optical feed-through port using a series of dielectric mirrors positioned to reflect at 45 ° angles. Beam attenuators include neutral density filters and a half-order waveplate coupled to a polarizer cube. A Newport periscope is used to translate the laser beam to the height of the optical feed-through platform. The laser is focused using two separate optics: a 1000 mm plano-convex lens used to pre-focus the beam to a size that can pass through the rear input-aperture on the Mitutoyo NIR 10x microscope objective mounted at the far end of the feed-through port. The laser beam at maximum focus in the DB 235 chamber is roughly 5 µm in diameter. A Newport Fast-Steering Mirror (FSM) is mounted with

a 45° bracket to the outer end of the laser feed-through port. The FSM is a two-axis voice-coil deflected mirror with a resolution of less than 2 µradians and closed-loop control up to 800 Hz. The response time of the FSM is adequately short for individual pulse deposition with mm's of spacing between pulses.

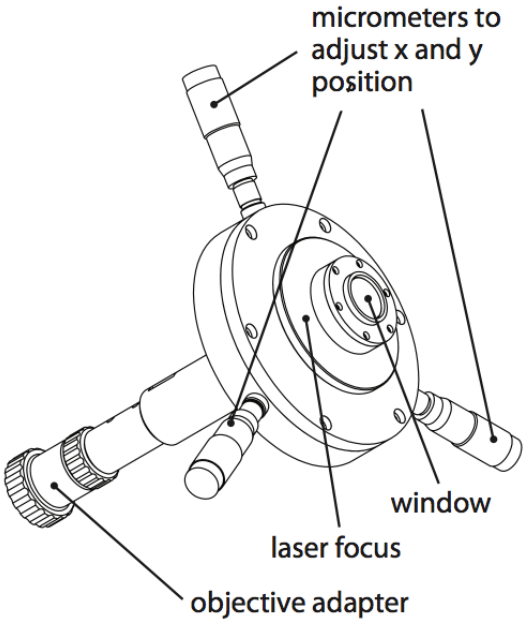

Figure 6.2: Schematic showing the laser interface port. The micrometers are used to translate and position the beam laterally. The depth of the microscope objective adapter tube can be adjusted externally to change the focal point inside the chamber. The translational and focal plane adjustments can be made while the system is under vacuum.

6.2.5 Micro-Stage

The existing FEI stage has a repeatability and a resolution in the µm-range and a tilt range of -15° to +52°. This is further limited to -5° to +40° once the EBSD detector and optical feed-through are installed. The tilt range required for the Tri-Beam setup is -60° to +70°, shown in Figure 6.3. Therefore, a smaller stage with a greater tilt range and a stable eucentric height at all tilt angles was engineered. This was achieved by incorporating Attocube™ piezoelectric driven positioners into the custom stage shown in Figure 6.3. This smaller, more versatile stage can be

installed on top of the existing stage permitting the simultaneous operation of both sets of stages for coarse and fine positioning. The linear Attocube™ micropositioners have sub 1 nm resolution and the piezoelectric rotator has a resolution of $\sim 1\,\mu^{\circ}$. The additional space occupied by the custom stage means that the maximum sample size is restricted to 9×9×5 mm. The stage can achieve all the required tilt positions for the EBSD, FIB, Electron beam, and laser which are 70°, 52°, 0°, and -60°, respectively.

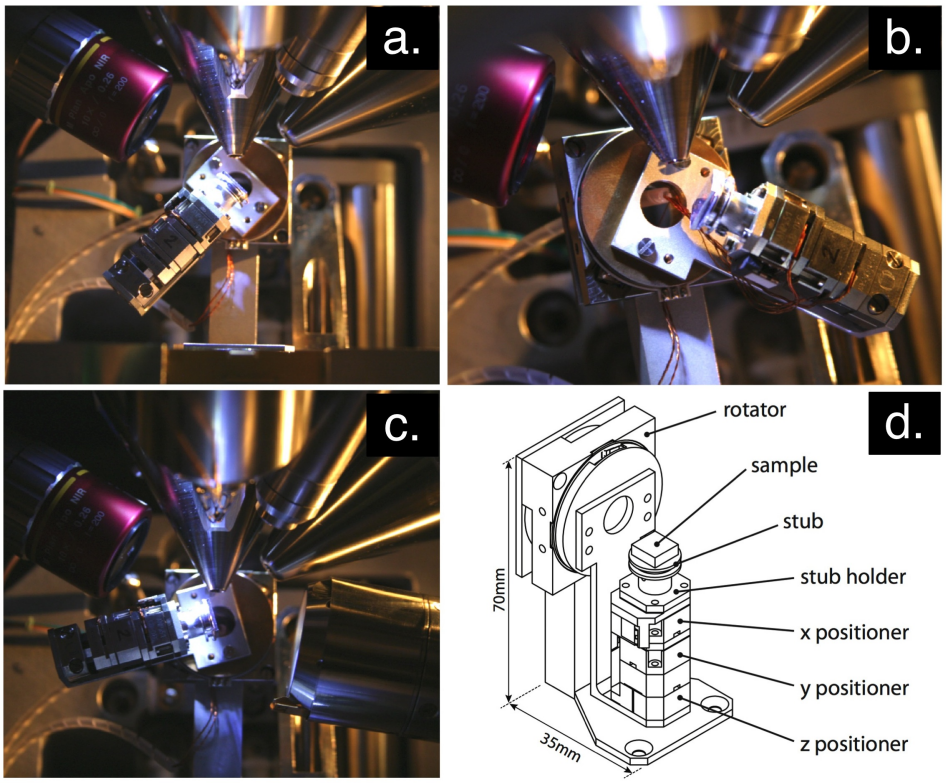

Figure 6.3: Micropositioner stage rotated to (a.) 52° for FIB machining and imaging. (b.) Micropositioner stage rotated to -60° for femtosecond laser machining. (c.) Micropositioner stage rotated to 70° for EBSD data collection. (d.) Schematic showing the custom microstage components necessary for access to all detectors and beams within the DB-235 vacuum chamber. The EBSD detector is automatically extracted for all other imaging or machining steps.

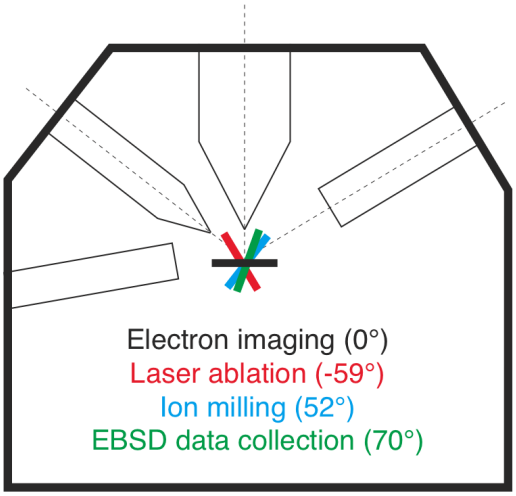

Figure 6.4: Schematic showing the stage angles necessary for access to all detectors and beams within the DB-235 vacuum chamber.

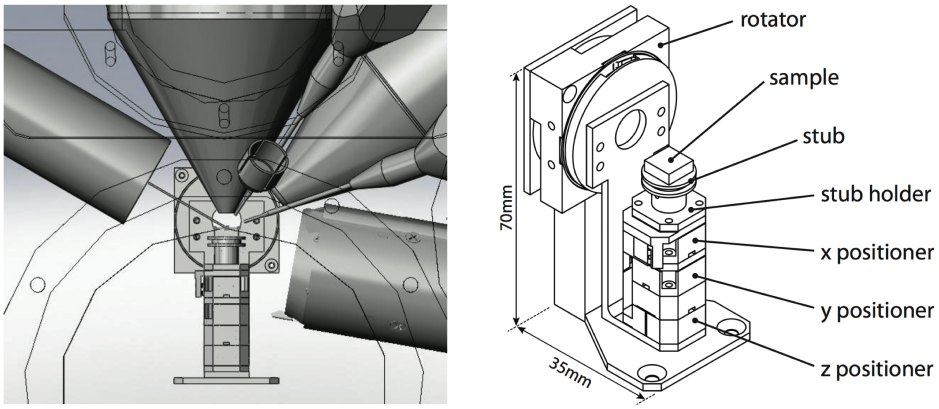

Figure 6.5: Micropositioner stage schematic and rotator.

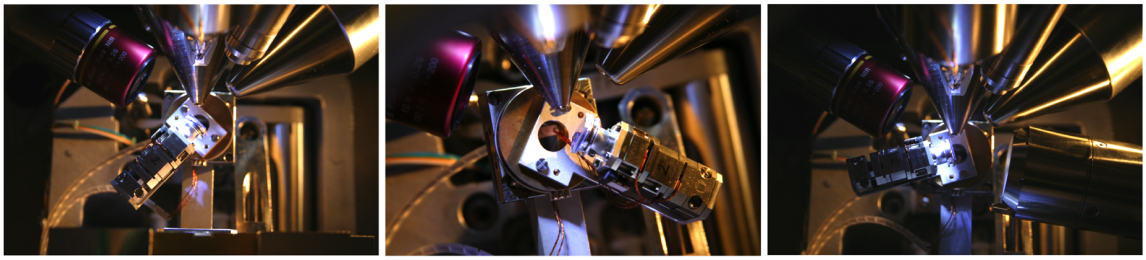

Figure 6.6: (left) Micropositioner stage rotated to 52° for FIB machining and imaging. (center) Micropositioner stage rotated to -59° for femtosecond laser machining. (right) Micropositioner stage rotated to 70° for EBSD data collection.

6.2.6 Energy Dispersive Spectroscopy Detector - EDS

The Strata DB 235 is equipped with an EDAX Apollo X energy dispersive spectrometer (EDS) detector for chemical analysis. The detector uses a $10\,mm^2$ Peltier-cooled silicon drift detector (SDD) capable of collecting spectra at a much higher rate than older N_2-cooled SiLi detector. The EDS detector can measure the energy of secondary x-rays emitted during beam/sample interaction. The energy of each x-ray is correlated to the possible electronic transition responsible for the emission event [191]. Therefore, EDS spectra can be interpreted to provide a qualitative chemical analysis of the sample [191].

6.2.7 Electron Backscatter Diffraction Detector - EBSD

The Strata DB 235 is also equipped with an EDAX OIM-Hikary XM4 electron back-scatter diffraction (EBSD) detector in order to collect data on crystallographic orientation. The interaction between a non-incident electron beam and the first few atomic layers of the sample results in diffraction patterns arising from back-scattering events. The diffraction pattern is captured by a CCD camera located behind a phosphor-coated screen. Patterns can be interpreted (indexed) to provide a crystal structure identity and orientation of the first few atomic layers at the point where the electron beam interacts with the sample [191].

6.3 Calibration and Integration

Routines were developed to control the stage motion, detectors, and beam steering mirrors. Protocol were also developed to determine eucentric sample height and to coordinate focus of the laser beam with the ion and electron beams.

6.3.1 Stage Control

A multi-step process has been developed to do the following: (1) bring the sample surface into the eucentric position for all three beams and (2) find the line-axis of rotation for the micropositioner. The following process achieves these goals:

1. Sample mounted on microstage
2. Sample surface is brought into focus with a working distance of $> 5\,\text{mm}$ in the electron beam using the z-positioner on the SEM stage
3. Sample is rotated using the SEM stage and the center point of rotation is positioned in the center of the SEM viewing area using the X and Y SEM stage positioners
4. Sample is iteratively tilted using the micropositioner tilt rotator while the Z-micropositioner is adjusted, until the sample surface is level with the center of the micropositioner tilt rotator.
5. The SEM Z-positioner is raised to bring the sample surface to $5\,\text{mm}$ working distance

In order to align the eucentric focus position for the ion, electron, and laser beams with the sample surface - the Z micropositioner must be raised until the sample surface is at the center of rotational axis for the microstage piezoelectric rotator. Once the sample is at eucentric focus for the micropositioner, the X,Y, and tilt positioners of the microstage may be freely moved without changing eucentric focusing conditions, all other SEM stage and microstage positioner values must not be modified after the initial calibration.

6.3.2 Laser Beam Alignment

Calibration and alignment of the SEM and FIB in the DualBeam™ system is regularly performed during service visits for the DB 235 tool. The Ion beam is calibrated to be in focus at the same point with the electron beam, therefore the electron beam is the reference for the system. The laser beam is focused and positioned to be at the same focusing set of conditions as the other two beams. The point of intersection is defined as the eucentric point because the beam focus, at any sample tilt position, is the same for all of the beams. Using the optical feed through port, the laser beam can be shifted in the X and Y planes (the entrance plane of the feed through port) and beam focus can be changed by inserting or withdrawing the optics tube that protrudes into the vacuum chamber.

The TriBeam system requires the additional alignment of the femtosecond laser to the eucentric point of the other two beams. Since the laser spot saturates the electron image detector, the alignment process is performed in reverse. A light emitting diode is centered on the sample mount within the chamber so that it may be viewed through the optical feed-through port. The battery powered LED assembly is small enough that it fits on the sample pedestal and approximates the typical size of an actual sample. With the illuminated marker loaded into the chamber for imaging, physical features of the LED surface are imaged with the SEM and used to center it at the eucentric position. The light source, now at the eucentric height, is used to visually align the objective attached to the optical feed-through in the chamber wall.

After the optical feed-through tube is aligned with the eucentric position, a diode laser tracer used to guide placement of optical components. With the SEM chamber door open, the laser pointer is inserted in the end of the optical feed-through tube and carefully aligned to the longitudinal axis of the tube. With this visible and safe laser source, systematically working upstream to place each optical component all the way to the femtosecond laser source is easily done. The last step is to turn on the

femtosecond laser source and systematically work back downstream. Beam location is checked at each optical component making minor adjustments as necessary through to the objective inside the SEM chamber.

6.3.3 Beam Control

The laser is scanned upon the sample surface using a Newport Fast Steering Mirror (FSM). This mirror is deflected in the X and Y directions using electromagnetic coils. The position of the mirror is electronically encoded for positioning feedback. The FSM is used to steer the laser beam in through the pass-through-port and raster across the sample surface. Currently, scanning protocols are similar to those used in the FSLSS technique, described in Section 4.2. The pulse overlap in the propagation direction and the line spacing is calibrated to have 50% overlap, from pulse-to-pulse. The focused beam size, with a 10X microscope objective and a lightly focusing 1000 mm plano convex lens, is $\sim 10\,\mu m$. For sectioning experiments, multiple scan patterns may be performed between imaging steps, in order to remove the required amount of material.

6.3.4 Ablation Parameters

The laser fluence determines, in conjunction with the laser spot size, the laser interaction volume. Material damage and roughening increases at fluences that are greater than 10 times the ablation threshold for the material. Ablation fluence is calculated indirectly, using the measurements of average power and minimum focused beam size, defined by:

$$\phi_{peak} = \frac{2P}{(RR)(\pi w_0^2)} \tag{6.1}$$

where ϕ_{peak} is the peak fluence, RR is the laser repetition rate, P is the average laser power, and w_0 is the $\frac{1}{e^2}$ focused beam diameter. The average laser power was

measured using a Ophir thermopile 3 Watt power meter. The laser spot size was measured using a Dataray Beam Profiler CCD camera.

6.4 Preliminary Data

EBSD was collected from area that had been laser machined using the FSLSS technique in standard atmosphere with a serpentine laser ablation scanning pattern with 50 % beam overlap. Laser machining was performed at fluences of 0.12 J/cm^2, 0.25 J/cm^2, and 0.37 J/cm^2 with the number of ablation pattern passes ranging from 5 to 15, see Figure 6.7. EBSD patterns were collected from all the laser machined areas, but with higher fidelity in areas that used lower laser fluences for machining. The EBSD pattern quality degraded with higher fluence laser irradiation, but stabilizes with a few laser machining patterns. In other words, the steady-state sample surface roughness is dependent on the laser fluence, which stabilizes after a few laser irradiation steps.

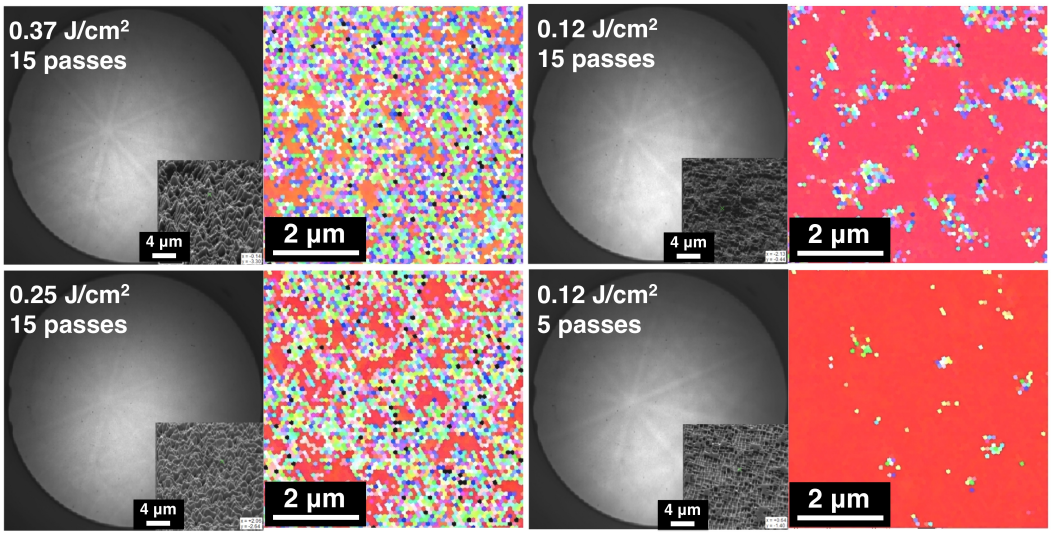

Figure 6.7: Femtosecond laser serial sectioning was performed with 5 or 15 passes of the standard ablation pattern, see Figure 4.2, at laser fluences of either 0.12 J/cm^2, 0.25 J/cm^2, or 0.37 J/cm^2. EBSD pattern were collected from all laser ablated regions, but with higher quality maps accessibly at lower fluences and lower numbers of passes.

The TriBeam system was used to collect five preliminary serial sections of polycrystalline nickel in vacuum. The material was machined at $1\,\mathrm{J/cm^2}$ with two machining patterning steps made for each imaging step. EBSD and secondary electron SEM images were collected for each slice. EBSD scan parameters were $0.7\,\mu\mathrm{m}$ step size. A total volume of $750\times750\times0.1\,\mu\mathrm{m}$ was laser machined for each step, although a small inset of the machined surface area was actually imaged due to collection time constraints. SEM images, image quality maps, and inverse pole figure maps are shown in Figure 6.10. The sample surface was slightly tilted during the experiment so that laser machining would preferentially ablate one side of the sample first. As the number of laser passes increased, the brightness in the image quality map figures decreased, indicating that lower quality EBSD information was collected. Although the image quality decreases, indexable EBSD patterns are still able to be collected from some areas. For a given fluence, the image quality map intensities decrease to a steady state value, which is most likely a function of sample roughness and dislocation injection. With increased number of laser passes at a given laser fluence, roughness is not observed to increase past the steady state value.

To summarize, laser based serial sectioning in the TriBeam system has been demonstrated to work by sectioning a polycrystalline nickel sample. Multi-modal SEM and EBSD data was collected for the nickel sample. EBSD data quality was shown to degrade to a steady state that still produced indexable patterns. Methodologies for finding the eucentric beam conditions and calibration routines for consistent sample positioning were also developed.

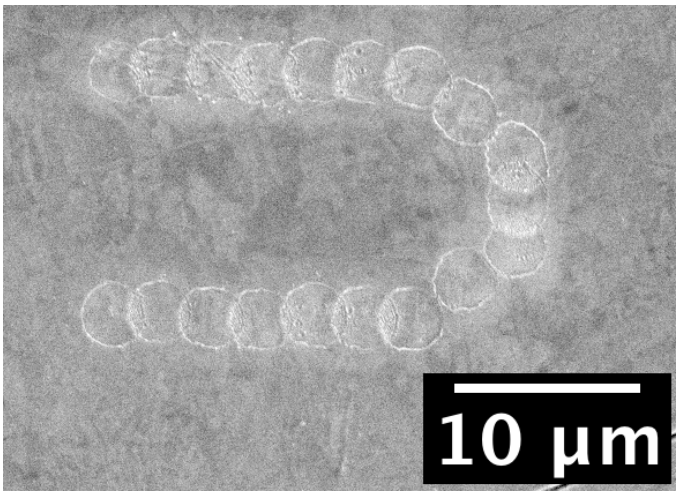

Figure 6.8: SEM image of a laser machined area of polycrystalline nickel made using the femtosecond laser in the Tri-Beam system. Single laser pulses were deposited in succession to scribe the letter "U". Each 10 µm spot is a single laser pulse.

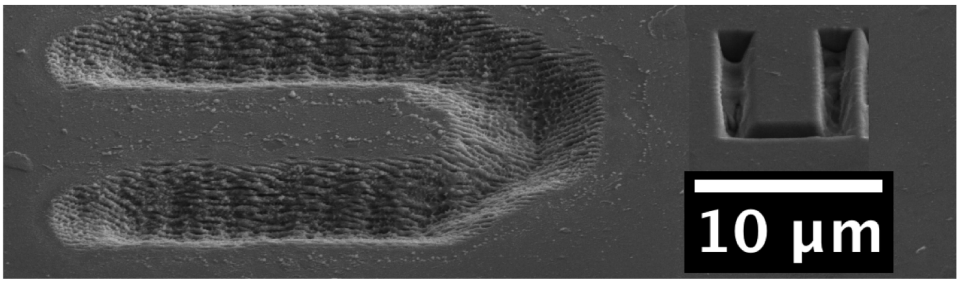

Figure 6.9: SEM image of a laser machined region of polycrystalline nickel and a smaller FIB machined area. Machining was done in vacuum. Laser machining required less than 60 seconds, while the FIB machining required 1.5 hours.

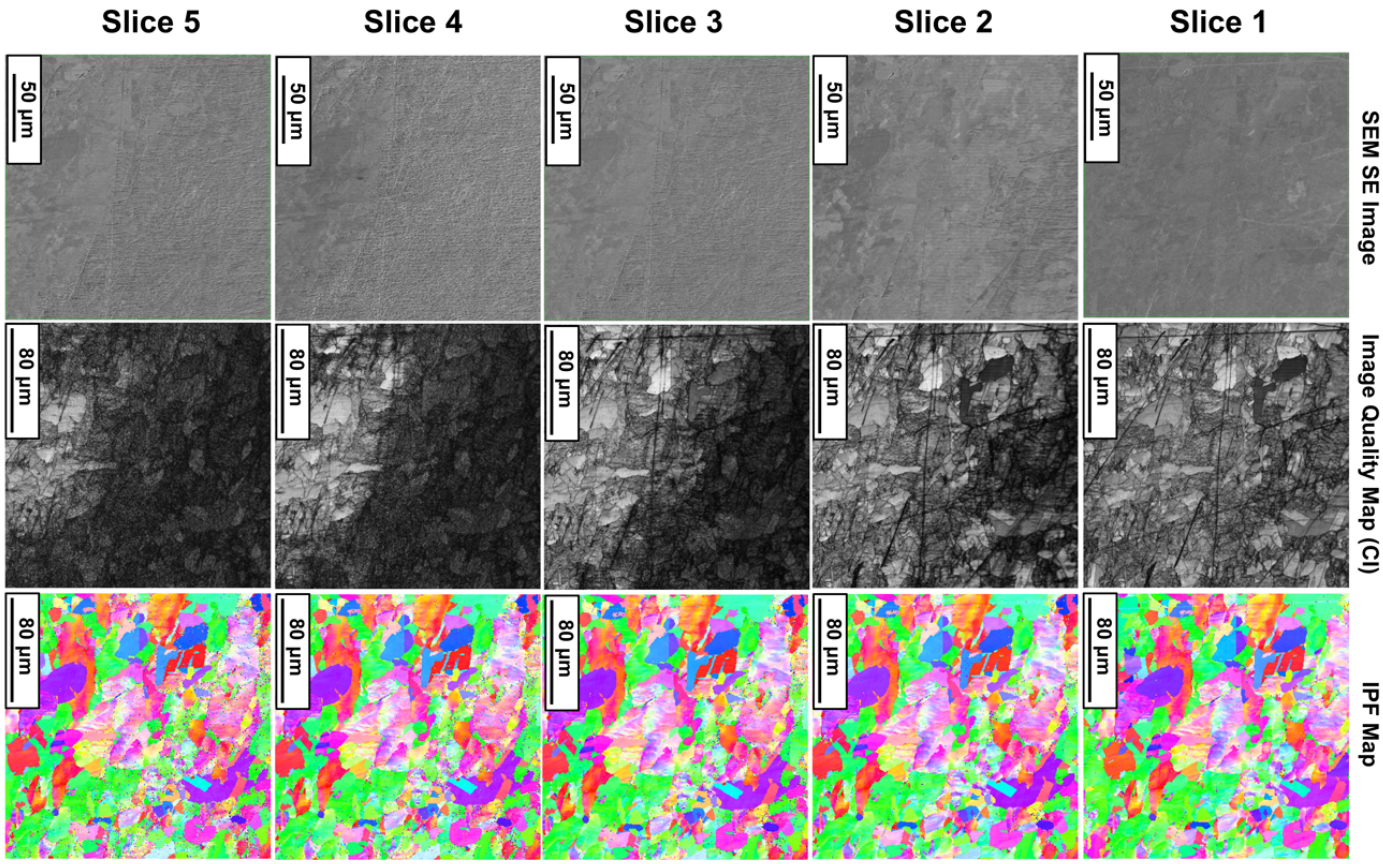

Figure 6.10: Using the Tri-Beam system, five slices were collected by laser machining polycrystalline nickel at a fluence of 1-4 J/cm^2. EBSD and secondary electron SEM images were collected for each slice. The sample was tilted, selectively machining part of the sample preferentially first. The EBSD imaging quality can be seen to decrease until the entire area is laser machined, at which point the surface quality reaches a steady state. By combining EBSD pattern collection with SEM imaging, segmentation of grains can be performed much more easily by comparing the boundaries in the two images. Furthermore, the EBSD information can be used to evaluate the effect of grain orientation texture, due to processing conditions, on mechanical properties.

CHAPTER VII

Summary, Conclusions & Future Work

This thesis has addressed fundamental aspects of multiphase material ablation, developed the technique and demonstrated its utility for statistical predictions of fracture toughness. The current and future capabilities of this new tomography approach are discussed in this chapter. Additionally, materials problems that could benefit from the extended TriBeam technique for high resolution multi-modal data collected in vacuum will be discussed, and future work is proposed.

7.1 FSLSS

The femtosecond laser based serial sectioning technique has been developed and validated as a fast, fully automated, and versatile sectioning technique. The femtosecond laser ablates material at 4-5 orders of magnitude faster than any other current used sectioning techniques for 3D tomography, see Table 7.1 and Figure 7.1. Once laser fluence parameters are defined, datasets are collected in less than 24 hours, particularly with laser beam scanning instead of sample scanning. The laser removal of a volume of material $750 \times 750 \times 0.5\,\mu m$ in size, with the galvometric scanning mirrors, takes less than 30 seconds with surface quality good enough for segmentation of microstructure down to $\sim 1\,\mu m$. Laser machining of 4330 steel was performed at fluences of $2\,J/cm^2$ or below, typically between 0.9-1.1 J/cm^2. Laser material interac-

tions were investigated using single pulse ablation to characterize the ablation rates and morphology. The application of laser sectioning to multiphase materials using the results of single pulse laser studies was also studied and then used for laser machining parameter selection. Laser scanning protocols have been developed using a serpentine scan pattern with pulse-to-pulse overlap of $\sim 50\,\%$ in both the direction of scanning and between scan lines.

We have demonstrated that femtosecond laser aided serial sectioning setup is a fast, volumetrically versatile, and automated tomographic technique able to reconstruct multiphase material systems. Other multiphase materials examined during the development of this technique include the following: nickel alloys with carbide constituents, layered zirconia intermetallic NiAl systems, and fibrous Mg alloy alumina composites (shown in Appendix A). Material removal rates of $10^5\,\mu m^3/s$ have been demonstrated, which is approximately 5 orders of magnitude faster than recently developed focused ion beam tomography techniques [3]. Further improvements in material removal rates are possible with laser improvements such as higher pulse repetition rates, increased power, different focusing conditions, and improved scanning protocols. This new tomography technique will be particularly useful for imaging multiphase systems containing phases with similar densities, which are difficult to image with other fast tomographic techniques such as X-ray imaging. In Table 7.1, a comparison of the removal rate, slice thickness, resolution, and addressable sample volumes are given for some common serial sectioning techniques. The presented sectioning techniques span a range of addressable material and microstructural length-scales. Major limitations of the various techniques include the speed and precision with which material can be removed. The femtosecond laser-based technique has a removal rate many orders of magnitude faster than the other techniques with a resolution that permits the analysis of sub-micron scale features. Finally, the inherent non-contact mode of laser machining also gives ample opportunity to section mate-

rials in vacuum and take advantage of other analysis techniques designed to operate in that environment, such as electron backscattered diffraction (EBSD) and energy dispersive X-ray spectroscopy (EDS).

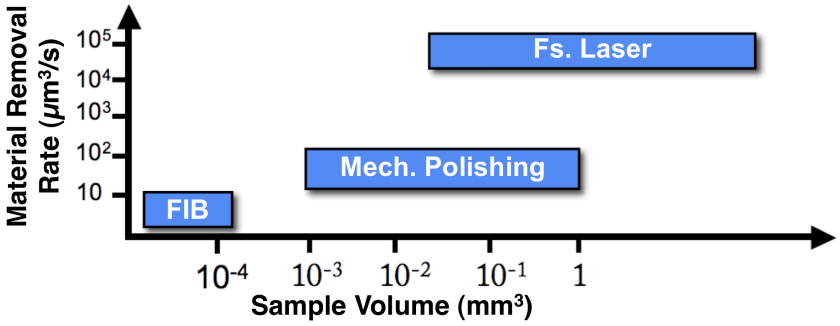

Figure 7.1: Maximum addressable sample volumes and material removal rates plotted for FIB, mechanical, and femtosecond laser machining.

Table 7.1: Comparison of various sectioning techniques: Atom Probe Tomography (APT), Focused Ion Beam Serial Sectioning (FIB-SS), Mechanical Serial Sectioning (Mech-SS), Femtosecond Laser Serial Sectioning (FSL-SS)

	Removal rate [$\mu m^3\ s^{-1}$]	Slice thickness [nm]	Resolution [nm]	Addressable volume [μm^3]
APT	10^{-8}	10^{-1}	0.5	10^{-3} - 10^{-4}
FIB-SS	0.5	5-100	10-30	10^{4} - 10^{5}
Mech-SS	200	100-2700	250	10^{7} - 10^{10}
FSL-SS	10^{4} - 10^{5}	20-150	250 (10-30)[a]	10^{7} - 10^{10}

[a] SEM assisted FSL-SS

In summary, the FSLSS system has produced the following main results:

- Development of a serial sectioning technique that utilizes a femtosecond laser (FSLSS)
    - Determination of laser fluence parameter, laser machining parameters, and methodology for sectioning with the FSLSS
    - Acquisition of near mm^3 volumes of material with µm-scaled resolution

- Removal rates 4-5 orders of magnitude faster than existing serial sectioning techniques

- Aquisition of 3D datasets of TiN precipitates in a 4330 steel with the FSLSS technique
  - Statistical information about the size, spatial distribution, and frequency of the TiN precipitates was measured
  - New 3D material sampling protocols that permit fracture toughness and its variability to be predicted without large-scale testing of many mechanical samples

7.2 Toughness Modeling of a 4330 Steel

The FSLSS technique was used as a means to extract parameters that characterize TiN particles in 4330 steel. TiN particles in steel are particularly deleterious to toughness, because they nucleate voids, which grow, coalesce, create stress concentrations, and reduce failure load. Statistical parameters, such as mean particle size, mean nearest neighbor distance, particle density, and volume fraction of particles were collected from eight FSLSS 3D datasets and compared with the same parameters from 2D stereological analysis, SEM imaging of deep-etched particles, and from other serial sectioning experiments. Direct statistical comparisons of individual TiN particle parameters showed that the local volumes of material sampled varied between techniques and samplings locations. Eight sub-samplings of each of six FSLSS 4330 steel datasets were made with equal volumes of $100 \times 100 \times 48\,\mu m$. These 48 samples were statistically analyzed to determine the same parameters describing TiN particles as discussed for the entire FSLSS datasets. The statistical parameters from the 48 sub-samples were used as input for two validated toughness models, the Wang-Olson Model and the Garrison-Moody Model. The J_{IC} and K_{IC} toughnesses calculated by

these models were fit to Weibull distributions to determine the relative variability (Weibull Modulus m) in the data. The Weibull modulus was calculated as 1.4 and 1.41, respectively, for the Wang-Olson and Garrison -Moody models. Ruggieri [188] statistically analyzed data from Wiesner [189] and found that toughness variability in two separate sets of ferritic C-Mn steel was characterized by Weibull Moduli of 1.4 and 1.5 , nearly identical to that of the 48 sub-sampled volumes collected with the FSLSS technique. Therefore, a major benefit of the methodology from Section 5.9, discussed briefly here, is that a small number of FSLSS datasets (6 FSLSS samples; 48 sub-samples) may be sampled from a small bulk volume of material ($1 \times 1 \times 3$ cm) to produce the same statistical representation characterized by 22 bulk toughness experiments. Failure modes, such as ductile fracture, tend to be characterized by their extreme and average values, which can be extracted from the collected distribution of modeled toughness values. The sub-sampled volumes that are representative of the extreme and average values have been reconstructed to show the local distribution of TiN particles resulting in the modeled toughness. For the extreme and average cases, a detailed finite element analysis of the volumes would be beneficial and recommended for understanding unfavorable particle spacing, clustering, size, volume fraction, and to determine the local stress and strain states that develop locally to the particles. This methodology then not only serves as an approach for predicting and validating toughness variability but also as a way of identifying detrimental particle volumes and their characteristics.

The toughness modeling in 4330 steel produced the following main results:

- A methodology for equal volume sampling FSLSS datasets
- Toughness modeling of sub-sampled volumes using locally sampled TiN particle parameters sampled from FSLSS datasets
- Weibull statistical analysis of the variation in modeled toughness values

- Comparison with bulk toughness experimental test specimens

7.3 The TriBeam System

The TriBeam system is the next developmental step in femtosecond laser based serial sectioning. The femtosecond laser is used to section material, still orders of magnitude faster than existing techniques, but now in vacuum. By femtosecond laser machining in a vacuum chamber, the options for methods of quantitative data collection become numerous. In the current configuration, chemical (EDS and BSE), grain orientation (EBSD), and topological (SE) can be collected during a sectioning experiment. The laser beam is passed into the vacuum chamber using a custom designed port, which has micrometer adjustments for shifting the beam location, and an adjustable objective lens positioner for focusing the laser beam spot on the sample surface. The beam is scanned on the sample surface using a fast-steering-mirror with µ-degree precision. The focused laser spot size is less than 10 µm as is evident in the in-situ laser ablation markings visible in Figure 6.8. Preliminary sectioning datasets have been collected for polycrystalline nickel with individual slices showing indexable EBSD patterns for $2\,\mathrm{J/cm^2}$ to $5\,\mathrm{J/cm^2}$ laser machined surfaces as well as SEM topological data.

The TriBeam project has produced the following main results:

- Multi-modal data collection
    - Energy Dispersive X-ray Spectroscopy (EDS): Quantitative chemical infomation
    - Electron Backscatter Diffraction (EBSD): Grain orientation and texture information
    - Secondary Electron (SE), Backscatter Electron (BSE): Topology, chemical info

- Tunable material removal rates
    - FIB smaller beam size (<10 nm) slower material removal
    - FSL larger beam size (>1 µm) faster material removal
- In-situ femtosecond laser machining
- Preliminary serial sectioning
    - Polycrystalline nickel serial sections with EBSD and SEM images
    - Qualitative damage evaluation for laser machined areas

7.4 Future Work

There are a number of materials problems that could benefit from the new tomography capabilities described in this thesis.

Future work pertaining to the FSLSS technique could include:

- Demonstration of the SVE FSLSS approach for predicting toughness in other material systems
- Assessment of TiN particle clustering in reconstructed 4330 steel sub-sampled regions and evaluation of the influence of clustering on toughness and toughness variability
- Laser machining studies outside of the bounds of laser fluence for multiphase material removal for improved of preferential etching, re-deposition, and surface roughening

Future research that could benefit from the capabilities of the TriBeam system includes, for example, some of the following problems:

- Sectioning and reconstruction of large datasets, with multi-modal data, for material systems listed below could provide new insights to their properties and guide development of new systems; this is discussed in more detail in sections 7.4.1 through 7.4.5:

    Layered metal/ceramic systems

    Accumulative roll-bonded Cu-Nb nano-laminates

    Co-Al-W metallic systems

    Polycrystalline Ti systems with processing induced grain orientation texture

    Semiconductor circuitry decomposition

    Polycrystalline Mg Alloys

- Development of programming framework for completely automated TriBeam sectioning

- Segmentation algorithms and registration algorithms utilizing mutual information techniques [190]

In the following section, some materials systems that could benefit are from the acquisition of 3D datasets with multi-modal information using the TriBeam system are discussed.

7.4.1 Layered Metallic/Ceramics

High temperature mechanical stability is a requirement for blades in the turbine stages just after the fuel combustion zone. Current blade technology uses a hybrid system of metal and ceramics for high temperature stability. A typical blade will be composed of a Ni-base superalloy, that contain a two-phase precipitation strengthened microstructure. Often, Ni-base superalloys used in blades possess microstructures composed of the matrix phase, γ, and the ordered L_{12} strengthening precipitates,

γ'[195]. They can be directionally solidified to reduce (columnar grains) or eliminate (single crystal) grain boundaries, which has been shown to increase creep resistance in superalloys [196]. A thermal barrier coating system can be used to reduce the temperature of internally cooled metallic blades and raise the overall operating temperature of the blade. The thermal barrier coating system is a layered system composed of, from the metal blade outward: (1) a aluminum rich bond coat, (2) a thermally grown oxide (TGO), (3) a ceramic top coat. Generally, an aluminum rich bond coating is deposited on the surface of the blade and then is diffused inward into the blade. A thermally grown oxide, usually Al_2O_3 is grown out of the aluminum rich bond coat to protect the blade from further oxidation. On top of the TGO is deposited a ceramic topcoat which provides most of the thermal insulating for the blade. TBCs can reduce the temperature experience by the metallic substrate by $\sim 100\,^{\circ}\mathrm{C}$, significantly increasing the operating temperature of the blade system. In Figure 7.3, a backscatter electron (BSE) image is shown of a Rene N5 superalloy substrate with a platinum aluminide bond coat and a yttria stabilized zirconia (7YSZ) top coat.

Failure mechanisms for TBC systems include [197]: rumpling or wrinkling of the bond coat or TGO (due to residual stresses), foreign object damage, and non-uniform oxidation imperfections [198], and aluminum or nickel diffusion and spinel formation. In this complex multilayer system, understanding the geometry of the interface between the layers and the presence of porosity can help predict where failure initiates and point to improvements in the processing steps. Using the TriBeam system, 3D datasets can be collected on the order of $400 \times 400 \times 400\,\mu\mathrm{m}^3$, which would capture all of the thermal barrier coating layers, a portion of the superalloy substrate, and a statistical sampling of the 20-50 µm top coat columns and the roughness of the thermally growth oxide (10-30 µms).

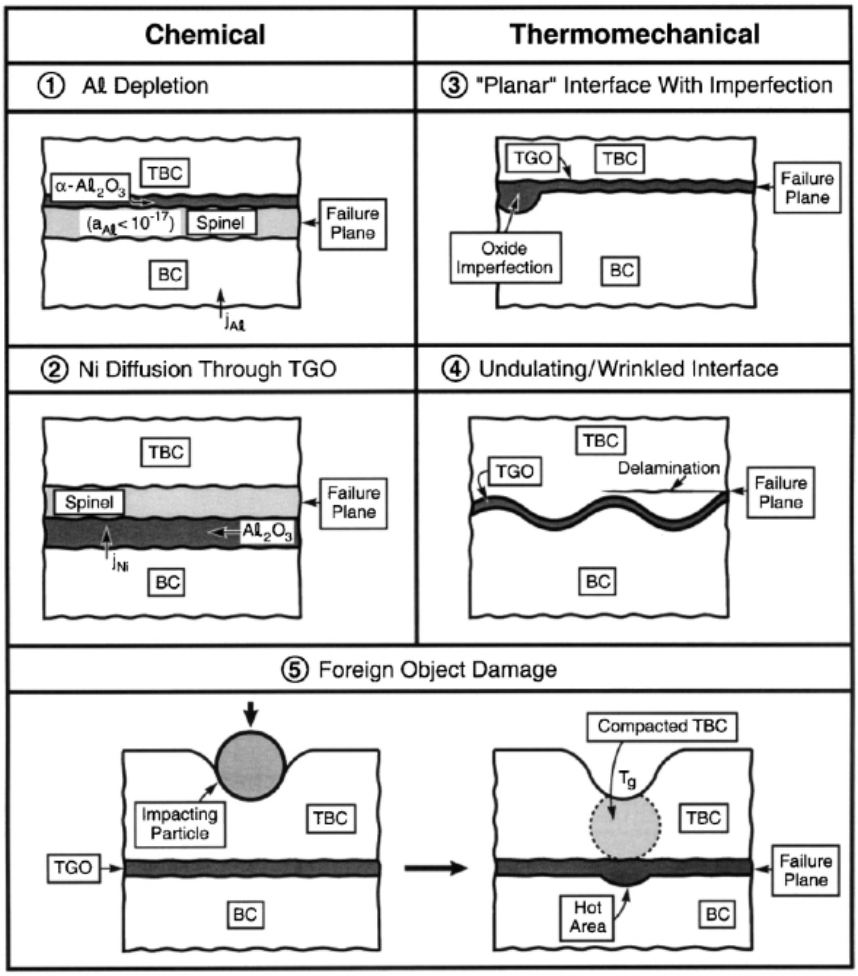

Figure 7.2: A schematic showing the five major failure mechanisms of thermal barrier coatings [197]. Datasets collected using the TriBeam system will identify the geometry of the interfaces between the layered systems and will characterize the porosity between the top coat, which allows the columns of ceramic to expand and contract upon thermal cycling without generating high residual stresses.

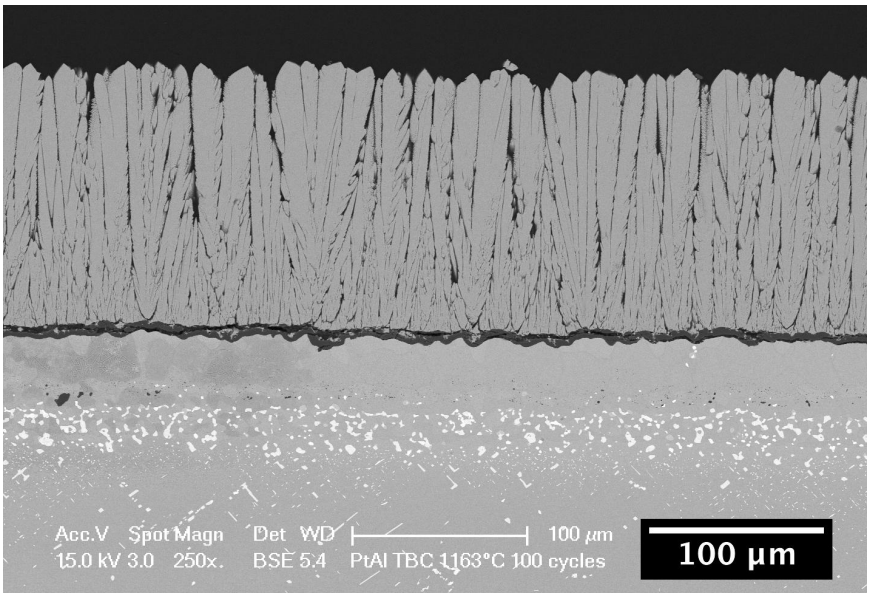

Figure 7.3: BSE images of TBC on a Rene N5 superalloy substrate with a Pt-aluminide bond coat after 100 thermal cycles to 1163°C (micrographs from R.W. Jackson [199]).

7.4.2 Co-Al-W Alloy

Recently, Sato identified cobalt base superalloys with greater high temperature strength than conventional nickel base superalloys [200]. This discovery is particularly useful because it could result in higher temperature turbine blade materials for the first and hottest stages of aero or land based turbine engines. The Co-base superalloys derive their strength from a γ-γ'precipitation strengthened microstructure similar to those of traditional Ni-base superalloys. There are a number of deleterious phases (with different structure) that can form if the chemistry of these cobalt base alloys is outside of the desired γ-γ'(ordered L_{12}) phase field, such as μ ($D8_5$), β (B2), and Co_3W ($D0_{19}$). In order to understand the formation (nucleation, growth, and morphology) of these phases, 3D datasets could be collected using the TriBeam system of alloys with slightly different chemistry and heat-treatments. These datasets would include multi-modal information. The chemistry of the phases present would be mapped using energy dispersive x-ray spectroscopy (EDS), which will be useful for image

segmentation of the various phases present. Also, electron backscatter diffraction (EBSD) will be used to collect grain orientation information and also aid in image segmentation of phases by making use of their different crystallographic orientation and structure. The 3D connectivity of the major phase constituents of the Co-base alloys may provide insight to the nucleation and growth of undesired phases. In Figure 7.4, an SEM image of a Co-base alloy containing a Co_3W phase and the μ phase shows their 2D morphology, particularly the interpenetrating lath structure.

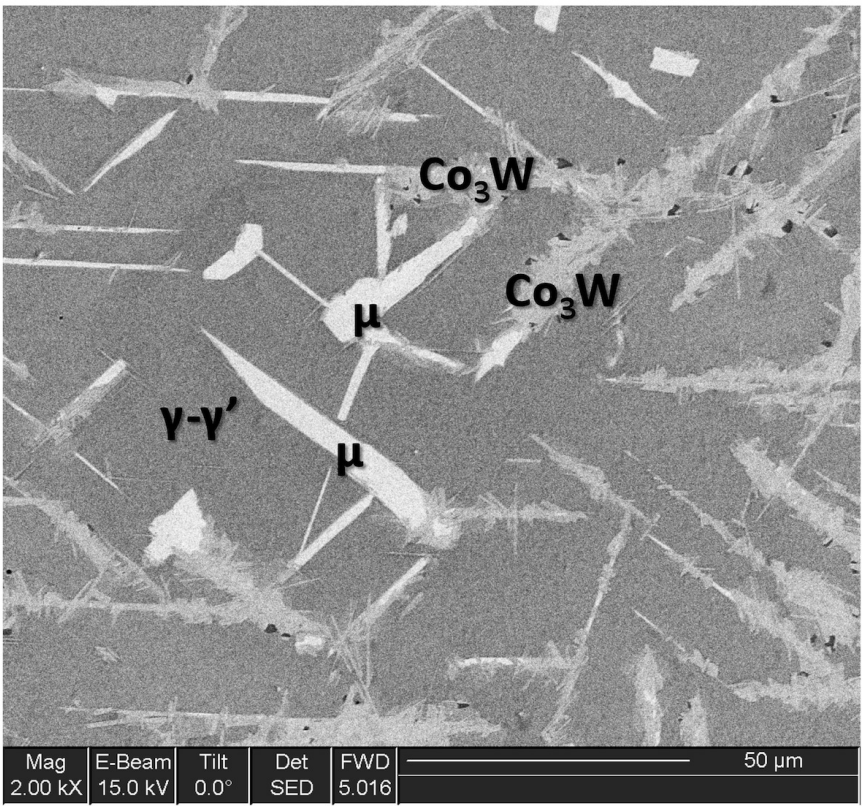

Figure 7.4: SEM micrograph showing a Co-base alloy heat treated at 900°C with μ and Co_3W phases. The μ phase has composition of 50W-47Co-2Al atomic%, the γ-γ'phase has composition 78Co-15W-9Al atomic%, and the Co_3W phase has composition 67Co-31W-2Al atomic% (micrographs from M. Titus [201]).

7.4.3 Accumulative Roll Bonded Cu-Nb Nanolaminates

It has been shown that Cu-Nb materials with high interface densities can have high strengths [202], good irradiation tolerance [203], and are thermally stable up

temperatures of 800°C [204]. The Cu-Nb nanolaminate system has mechanical properties that are substantially improved compared to the properties of the individual composite elements. This is because of the high density of layers and the immiscibility of the two alloying components, leading to a bulk material which has interface dominated properties. For high layer purity and the consistent layer thickness, physical vapor deposition is used to fabricate small Cu-Nb samples. In order to scale up sample sizes, the accumulative roll bonding (ARB) process has been used to fabricate larger nano-layered samples. The ARB process uses a rolling mill to iteratively fold and compress a layered sample onto itself. During the ARB process defects have been shown to occur, which could substantially reduce the mechanical properties of the composite. In Figure 7.5, optical micrographs of a Cu-Nb nanolaminate is shown with two different types of defect structures. Using the TriBeam system, 3D grain orientation of the nanolaminates and the spatial arrangement of the defects in Figure 7.5 can be identified. EBSD patterns in 2D have already been collected from CuNb nanolaminates, shown in Figure 7.6. The TriBeam system can be used to resolve smaller volume FIB 3D EBSD maps to determine grain orientation texturing present, along with larger 3D volumes composed of SEM images to determine the arrangement of rolling defects and to guide development of roll bonded processing parameters.

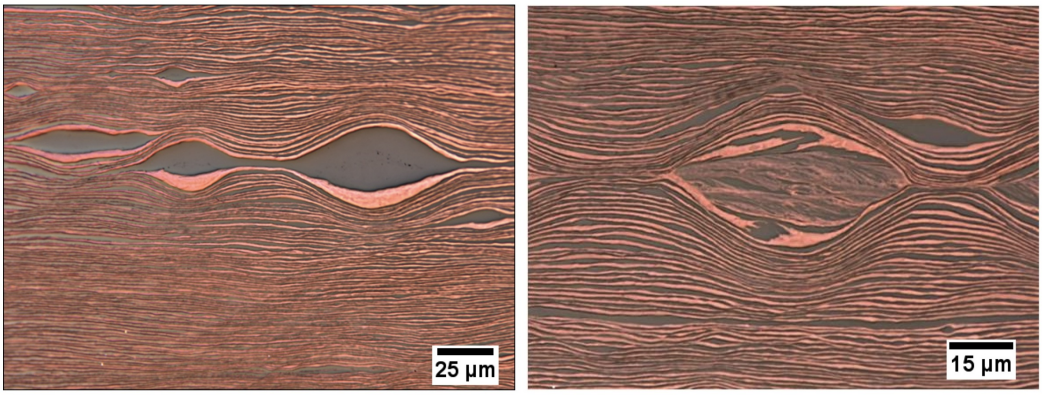

Figure 7.5: Optical micrograph of Cu-Nb nanolaminate material. Accumulative roll bonding is used to create thing layers of alternating Cu and Nb. (left) Elipsoidal Nb defects are visible between layers. (right) Intermixed elipsoidal Cu-Nb defects are present between layers. (micrographs from T. Nizolek [205]).

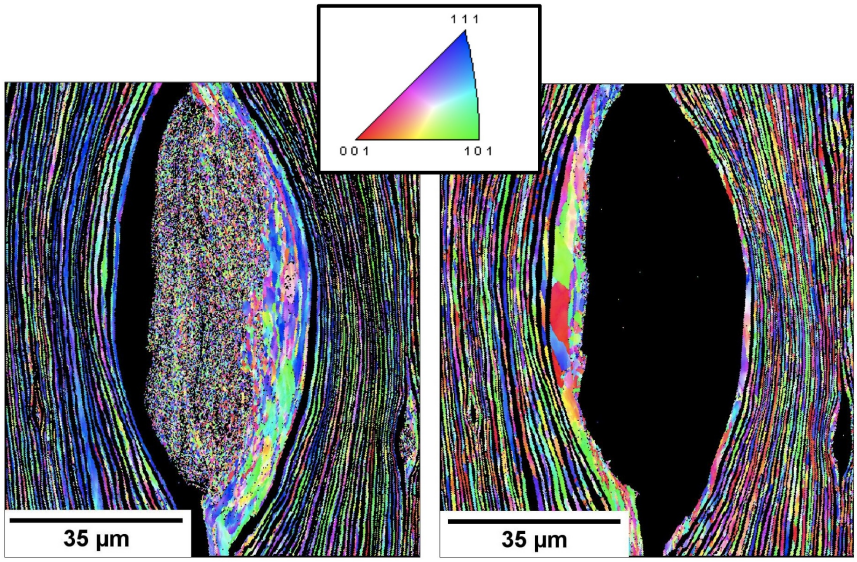

Figure 7.6: EBSD micrographs of Cu-Nb nanolaminate material. EBSD step size (micrographs from T. Nizolek [205]).

7.4.4 Polycrystalline Titanium

Titanium alloys and their material properties are particularly sensitive to their processing history [206]. By precisely controlling these thermo-mechanical processing conditions, titanium alloys can be tailored to have desired properties based on the

stable phases (α, β, $\alpha - \beta$), grain size, and grain orientation. In Szczepanski's dissertation work [207], local α grain orientation texturing in $\alpha + \beta$ titanium alloys was shown to be important to the fatigue crack initiation process. Following 3D serial sectioning, reconstruction, and analysis of titanium β grains by Rowenhorst [58], the TriBeam system could be used to analyze the grain orientation texture and the role it plays in fatigue initiation. Mechanical serial sectioning techniques have been applied to gather grain orientation information in 3D in the past, such as in Rowenhorst's 3D dataset shown in Figure 2.4. The TriBeam system can gather 3D EBSD datasets with fully scripted automation and with more simple segmentation and alignment routines due to the precision of the custom nanopositioner stages.

7.4.5 Semiconductor Device Decomposition and Characterization

Many electronic devices require micro-scale patterning of interconnects and multi-layered semiconductor structures. The process of developing patterning and processing conditions necessary to fabricate an electronic device requires techniques to characterize the prototype device structures. The TriBeam system could be used to section electronic devices to reveal their structure and composition. Datasets on the order of mm^3 would be gathered with EDS chemical information to segment and differentiate the thin semiconductor layers. Segmentation of electronic devices should be straightforward due to the high phase contrast between lighter polymeric materials used for the casing and the semiconductors and metals used for the device itself.

APPENDICES

APPENDIX A

FSLSS Dataset Reconstructions

The following datasets were collected from a double-linear shear bar specimen of titanium modified 4330 steel using the FSLSS technique. TiN particles were segmented from the matrix and then reconstructed. Statistical measures from the datasets are outlined in Chapter V and the FSLSS collection parameters are listed in the datasets figure captions.

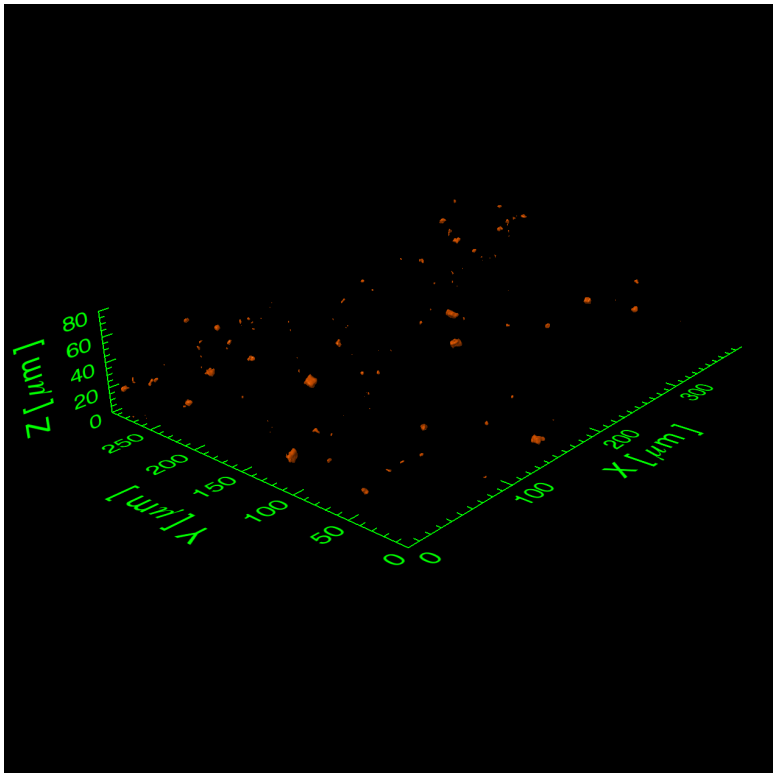

Figure A.1: FSLSS dataset of size $404.4 \times 301.7 \times 82.9\,\mu\text{m}$, with imaging resolution of $0.16\,\mu\text{m}$/pixel and slice resolution of $0.56\,\mu\text{m}$/pixel. TiN volume fraction is $0.041\,\%$, particle density is 3.6×10^{14} particles/m^3, mean particle size is $0.80\,\mu\text{m}$, and nearest neighbor spacing is $4.98\,\mu\text{m}$.

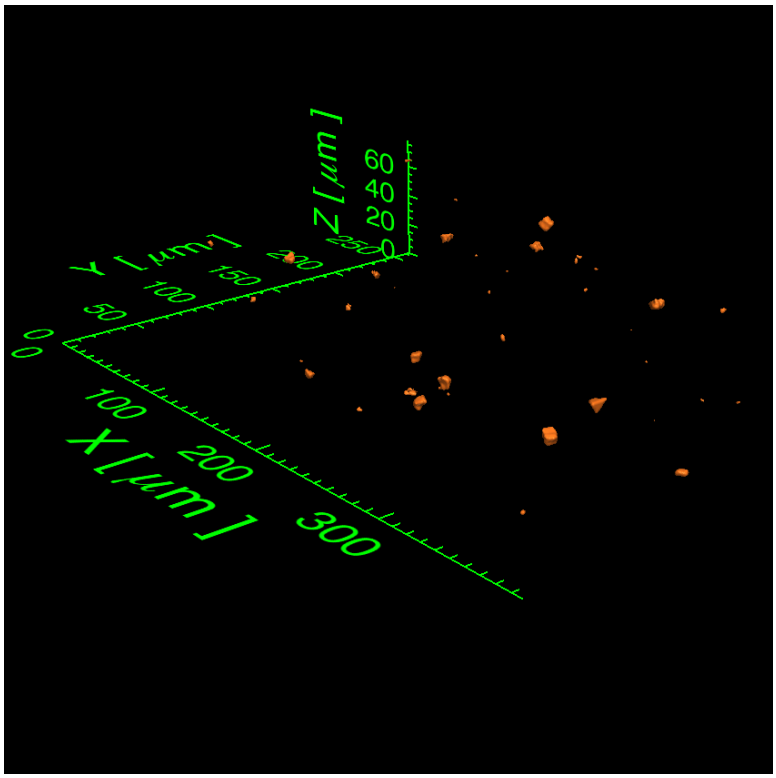

Figure A.2: FSLSS dataset of size $404.4 \times 301.7 \times 77.9\,\mu\text{m}$, with imaging resolution of $0.16\,\mu\text{m}$/pixel and slice resolution of $0.56\,\mu\text{m}$/pixel. TiN volume fraction is $0.021\,\%$, particle density is 1.1×10^{13} particles/m^3, mean particle size is $2.06\,\mu\text{m}$, and nearest neighbor spacing is $18.08\,\mu\text{m}$.

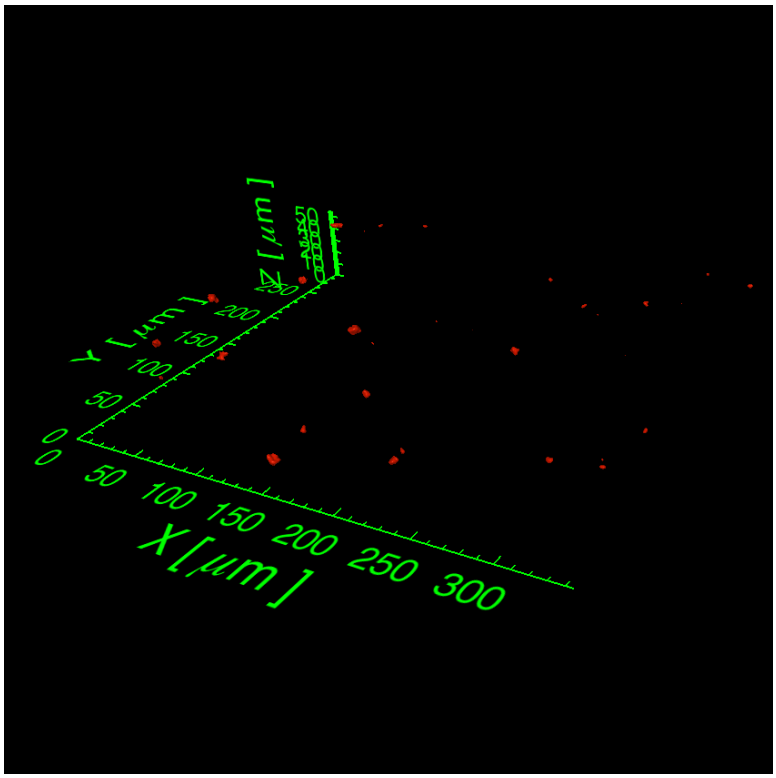

Figure A.3: FSLSS dataset of size $404.4 \times 301.7 \times 54.4\,\mu m$, with imaging resolution of $0.16\,\mu m$/pixel and slice resolution of $0.56\,\mu m$/pixel. TiN volume fraction is $0.019\,\%$, particle density is 7.0×10^{12} particles/m^3, mean particle size is $2.78\,\mu m$, and nearest neighbor spacing is $25.17\,\mu m$.

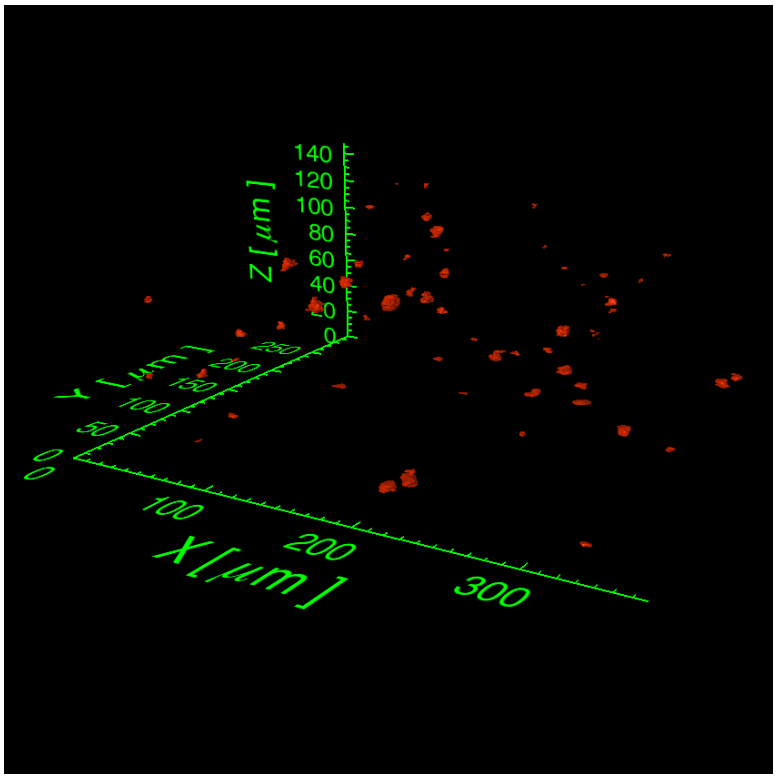

Figure A.4: FSLSS dataset of size $404.4 \times 301.7 \times 149\,\mu\text{m}$, with imaging resolution of $0.17\,\mu\text{m}$/pixel and slice resolution of $0.43\,\mu\text{m}$/pixel. TiN volume fraction is $0.044\,\%$, particle density is 2.0×10^{13} particles/m^3, mean particle size is $1.21\,\mu\text{m}$, and nearest neighbor spacing is $3.10\,\mu\text{m}$.

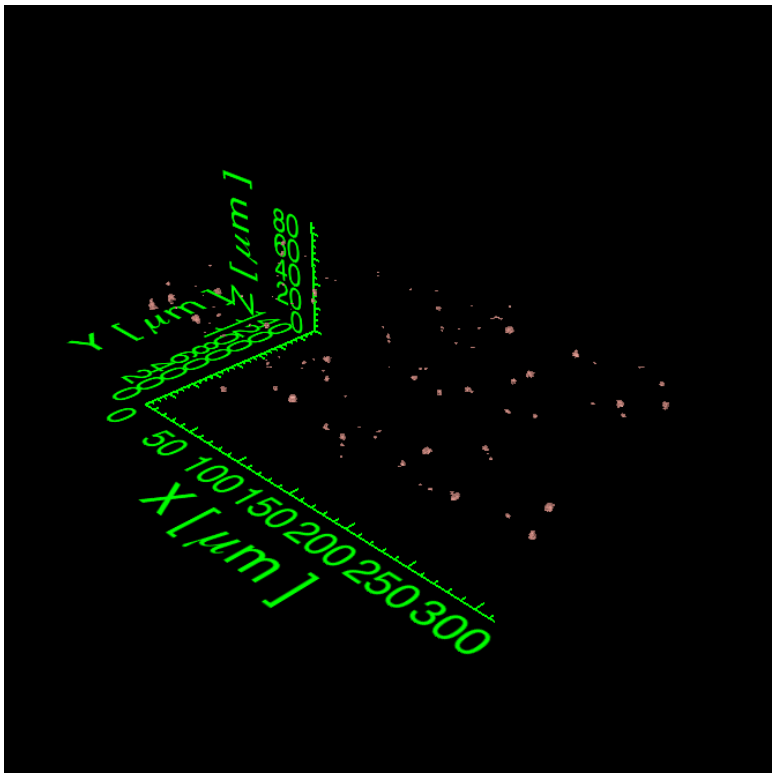

Figure A.5: FSLSS dataset of size $314.1 \times 156.0 \times 89\,\mu m$, with imaging resolution of $0.15\,\mu m$/pixel and slice resolution of $0.22\,\mu m$/pixel. TiN volume fraction is $0.028\,\%$, particle density is 2.9×10^{13} particles/m^3, mean particle size is $2.12\,\mu m$, and nearest neighbor spacing is $9.97\,\mu m$.

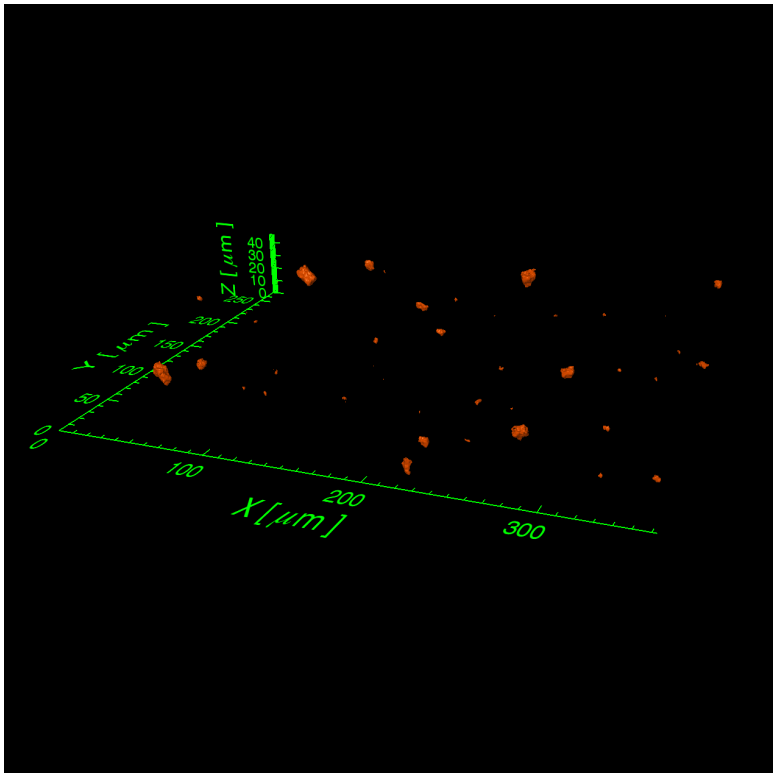

Figure A.6: FSLSS dataset of size $404.4 \times 301.7 \times 46\,\mu\text{m}$, with imaging resolution of $0.16\,\mu\text{m}$/pixel and slice resolution of $0.50\,\mu\text{m}$/pixel. TiN volume fraction is $0.052\,\%$, particle density is 1.9×10^{13} particles/m^3, mean particle size is $2.49\,\mu\text{m}$, and nearest neighbor spacing is $19.37\,\mu\text{m}$.

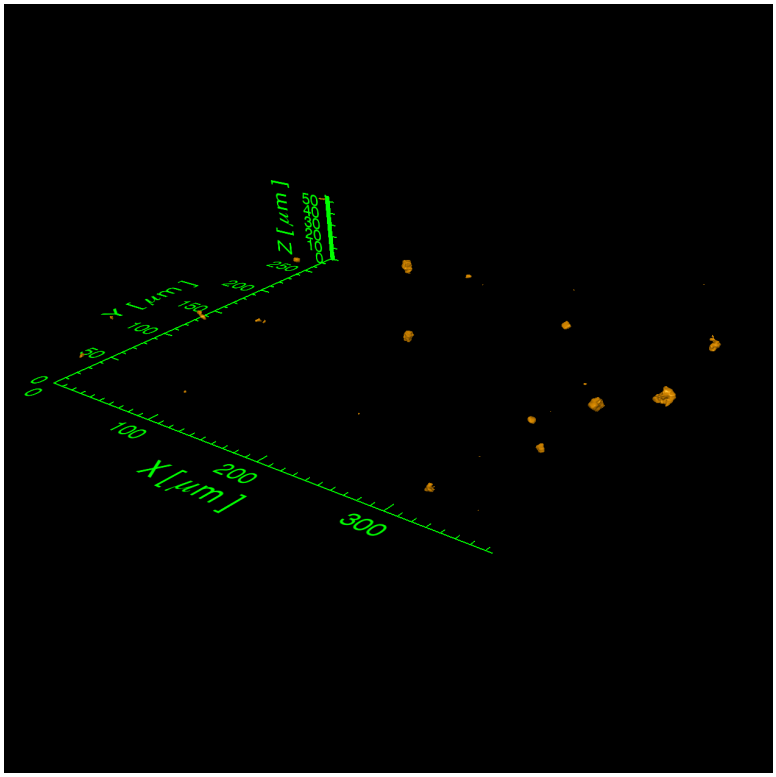

Figure A.7: FSLSS dataset of size $404.4 \times 301.7 \times 55\,\mu m$, with imaging resolution of $0.16\,\mu m$/pixel and slice resolution of $0.42\,\mu m$/pixel. TiN volume fraction is $0.029\,\%$, particle density is 1.4×10^{13} particles/m^3, mean particle size is $1.74\,\mu m$, and nearest neighbor spacing is $13.04\,\mu m$.

APPENDIX B

Matlab Image Processing Segmentation Code

```
% % % % % % % % % % % % % % % % % % % % % % % % % % % % % % % % % % % % % % % % % % % % % % % % %
% % %  Image Segmentation Code written for use with the FSLSS technique
% % %  Designed to segment TiN particles from 4330 steel matrix and create a binary image
% % %
% % %  Code written by: Naji S. Husseini in Matlab Proframming Language
% % %
% % % % % % % % % % % % % % % % % % % % % % % % % % % % % % % % % % % % % % % % % % % % % % % % %

% % % % % % % % % % % % % % % % % % % % % % % % % % % % % % % % % % % % % % % % % % % % % % % % %
% % %  Step one -- finding the center of the image
% % % % % % % % % % % % % % % % % % % % % % % % % % % % % % % % % % % % % % % % % % % % % % % % %

% This script corrects for chromatic aberations in the optics

img=imread([IM_PATH num2str(IMAGE_MIN) '.tiff']);
imgbw=rgb2gray(img);
red=img; green=img; blue=img;

% Separates the original image into the three RGB components
red(:,:,[2 3])=0;
green(:,:,[1 3])=0;
blue(:,:,[1 2])=0;

% Finds the red-to-green/blue ratios and the product of the two ratios
rg_ratio=double(red(:,:,1))./double(green(:,:,2));
```

```
rb_ratio=double(red(:,:,1))./double(blue(:,:,3));
z=rb_ratio.*rg_ratio;

% Use imshow to visually determine the center.  Look for the center where the least distortion occurs.
imshow(z,[])
% Use ginput to select the location

% % % % % % % % % % % % % % % % % % % % % % % % % % % % % % % % % % % % % % % % % % % % % % % % % %
% % % Step two -- finding the expansion once you know the center (XC YC)
% % % % % % % % % % % % % % % % % % % % % % % % % % % % % % % % % % % % % % % % % % % % % % % % % %

img=imread([IM_PATH num2str(45) '.tiff']);
[xsize ysize zsize]=size(img);

% Since imresize works from the center of the image, need to make the original image into a square.
% It is padded with the mean intensity.
newXC=XC; newYC=YC;
if XC<xsize/2, newXC=xsize-XC; end
if YC<ysize/2, newYC=ysize-YC; end
% Determines the offset in the centers of the various colors
offset=round(newXC*(SF-1));

% Need to rotate center of chromatic expansion into the bottom right quad
if newXC==XC && newYC==YC
    % Bottom right corner
    tempimg=mean2(img)*ones(newXC*2,newYC*2,3,'uint8');
    ang=0;
    tempimg(1:xsize,1:ysize,:)=imrotate(img,ang);
elseif newXC~=XC && newYC~=YC
    % Top left corner
    tempimg=mean2(img)*ones(newXC*2,newYC*2,3,'uint8');
    ang=180;
    tempimg(1:xsize,1:ysize,:)=imrotate(img,ang);
elseif newXC==XC && newYC~=YC
    % Bottom left corner
    tempimg=mean2(img)*ones(newYC*2,newXC*2,3,'uint8');
    ang=90;
    tempimg(1:ysize,1:xsize,:)=imrotate(img,ang);
elseif newXC~=XC && newYC==YC
    % Top right corner
    tempimg=mean2(img)*ones(newYC*2,newXC*2,3,'uint8');
```

```
    ang=270;
    tempimg(1:ysize,1:xsize,:)=imrotate(img,ang);
end



% Expands and offsets the different colors by the scaling factor
newgreen=imresize(tempimg(:,:,2),(1+SF)/2);
newgreen=offsetter(newgreen,[-round(offset/2) -round(offset/2)]);
newred=imresize(tempimg(:,:,1),SF);
newred=offsetter(newred,[-offset -offset]);

% Crops out the black borders created by offsetting
if ang==0 || ang==180
    newred=newred(1:xsize,1:ysize);
    newgreen=newgreen(1:xsize,1:ysize);
    newblue=tempimg(1:xsize,1:ysize,3);
else
    newred=newred(1:ysize,1:xsize);
    newgreen=newgreen(1:ysize,1:xsize);
    newblue=tempimg(1:ysize,1:xsize,3);
end

% Combines the new colors into one image and rotates it back to the original position
finalimg(:,:,1)=newred; finalimg(:,:,2)=newgreen; finalimg(:,:,3)=newblue;
finalimg=imrotate(finalimg,(-1)*ang);

% Play with this command below to see how the images scale.
figure(1), imshow(finalimg(:,:,3)), figure(2), imshow(finalimg(:,:,1))

% % % % % % % % % % % % % % % % % % % % % % % % % % % % % % % % % % % % % % % % % % % % % % % % %
% % % Init_var file contains the variable for segmentation
% % % User should change these as necessary
% % % Adjust Init_var File based on Step1 and Step2 output
% % % % % % % % % % % % % % % % % % % % % % % % % % % % % % % % % % % % % % % % % % % % % % % % %

% Defines the first image and last image to be analyzed. Note that the FIB
% files run from IMAGE_MIN-1:IMAGE_MAX-1 since they are incremented
% starting at 0. Thus IMAGE_MAX ends up being the total number of images
IMAGE_MIN=25; IMAGE_MAX=50;

% Original file name without increment.
```

```
IM_PATH='4-7-2011c_';

% Defines size of disk filter after binary image has been created in
% cleaner.m.
DISK_SIZE=5;

% Defines the sensitivity between 1 and 255 of the peak-finding routine.
% Lowering this may find more carbides, but it will also find more
% false-positive images. Used in asdf.m.
THRESHOLD=90;

% Defines the threshold for the red-to-green and red-to-blue ratio.
% Increase this to decrease sensitivity to red. used in coloranalyzer.m
RG_RATIO=1.4;
RB_RATIO=1.4;

% Defines parameters for gauss filter in bkgdsubtract.m. Change these to
% reduce blurring.
GAUSS_SIZE=15; GAUSS_STD=5;

% Defines threshold for identifying peaks in smoother.m. Increasing this
% value will have fewer false positives, but may miss weaker spots.
CRIT_INT=30;

% % % % % % % % % % % % % % % % % % % % % % % % % % % % % % % % % % % % % % % % % % % % % % % % %
% % %  Must be changed manually after color correction
% % % % % % % % % % % % % % % % % % % % % % % % % % % % % % % % % % % % % % % % % % % % % % % % %

% Defines the center from which the chromatic blurring occurs.
% NOTE: SWITCH ORDER OF THE OUTPUT OF GINPUT!! GINPUT REVERSES ORDER OF
% COORDINATES
XC=780; YC=1760;

% Defines the scaling factor. This should be greater than 1 because blue is
% more expanded than red.
SF=1.0075;

% Gets image dimensions
[XSIZE YSIZE ZSIZE]=size(imread([IM_PATH num2str(IMAGE_MIN) '.tiff']));

% % % % % % % % % % % % % % % % % % % % % % % % % % % % % % % % % % % % % % % % % % % % % % % % %
```

```
% % % Colorcenterer
% % % This program corrects for the blurring of colors. When separated into
% % % red, green, and blue, the colors do not overlap: green is stretched
% % % beyond red, and blue is stretched doubley as much. The stretching occurs
% % % from a random point near the bottom right, which must be determined.
% % %
% % % The output is a cropped color image with significantly less chromatic blurring
% % % % % % % % % % % % % % % % % % % % % % % % % % % % % % % % % % % % % % % % % % % % % % % % % %

init_var

% Size of the images, based on the size of the initial image.

img=imread([IM_PATH num2str(IMAGE_MIN) '.tiff']);
[xsize ysize junk]=size(img);
clear img junk

for k=IMAGE_MIN:IMAGE_MAX
    img=imread([IM_PATH num2str(k) '.tiff']);

    % Since imresize works from the center of the image, need to make the
    % original image into a square. It is padded with the mean intensity.

    newXC=XC; newYC=YC;
    if XC<xsize/2, newXC=xsize-XC; end
    if YC<ysize/2, newYC=ysize-YC; end

    % Determines the offset in the centers of the various colors
    offset=round(newXC*(SF-1));

    % Need to rotate center of chromatic expansion into the bottom right quad
    if newXC==XC && newYC==YC
        % Bottom right corner
        tempimg=mean2(img)*ones(newXC*2,newYC*2,3,'uint8');
        ang=0;
        tempimg(1:xsize,1:ysize,:)=imrotate(img,ang);
    elseif newXC~=XC && newYC~=YC
        % Top left corner
        tempimg=mean2(img)*ones(newXC*2,newYC*2,3,'uint8');
        ang=180;
        tempimg(1:xsize,1:ysize,:)=imrotate(img,ang);
```

```
    elseif newXC==XC && newYC~=YC
        % Bottom left corner
        tempimg=mean2(img)*ones(newYC*2,newXC*2,3,'uint8');
        ang=90;
        tempimg(1:ysize,1:xsize,:)=imrotate(img,ang);
    elseif newXC~=XC && newYC==YC
        % Top right corner
        tempimg=mean2(img)*ones(newYC*2,newXC*2,3,'uint8');
        ang=270;
        tempimg(1:ysize,1:xsize,:)=imrotate(img,ang);
    end

    % Expands and offsets the different colors by the scaling factor
    newgreen=imresize(tempimg(:,:,2),(1+SF)/2);
    newgreen=offsetter(newgreen,[-round(offset/2) -round(offset/2)]);
    newred=imresize(tempimg(:,:,1),SF);
    newred=offsetter(newred,[-offset -offset]);

    % Crops out the black borders created by offsetting
    if ang==0 || ang==180
        newred=newred(1:xsize,1:ysize);
        newgreen=newgreen(1:xsize,1:ysize);
        newblue=tempimg(1:xsize,1:ysize,3);
    else
        newred=newred(1:ysize,1:xsize);
        newgreen=newgreen(1:ysize,1:xsize);
        newblue=tempimg(1:ysize,1:xsize,3);
    end

    % Combines the new colors into one image and rotates it back to the original position
    finalimg(:,:,1)=newred; finalimg(:,:,2)=newgreen; finalimg(:,:,3)=newblue;
    finalimg=imrotate(finalimg,(-1)*ang);

    % Writes the corrected images into centered###.tif
    imwrite(finalimg,imgnumberer('centered',k,IMAGE_MAX,'.tif'),'TIF',...
        'WriteMode','OverWrite');
    disp([num2str(k-IMAGE_MIN+1) ' of ' num2str(IMAGE_MAX-IMAGE_MIN+1) ' iterations']);

    clear finalimg

end
```

```
%%%%%%%%%%%%%%%%%%%%%%%%%%%%%%%%%%%%%%%%%%%%%%%%%%%%%%%%%%%%%%%%%%%
%%% Locates peaks
%%%
%%% Finds peaks by locating the top and rolling down the sides until it comes
%%% to about 20 intensity values above the images' means.
%%% Output images are in "cleaned###.tif"
%%%%%%%%%%%%%%%%%%%%%%%%%%%%%%%%%%%%%%%%%%%%%%%%%%%%%%%%%%%%%%%%%%%

init_var

for k=IMAGE_MIN:IMAGE_MAX
    img=imread(imgnumberer('centered',k,IMAGE_MAX,'.tif') );
    img=img(:,:,3);
%     load(imgnumberer('bkgdsub',k,IMAGE_MAX,'.mat'));
%     bkgdsub=255-imread(imgnumberer('picked',k,IMAGE_MAX,'.tif'));
    bin=smoother(img,THRESHOLD,XSIZE,YSIZE,CRIT_INT);
    imwrite(bin*255,imgnumberer('cleaned',k,IMAGE_MAX,'.tif'),'TIF',...
        'WriteMode','OverWrite','compression','none');
    disp([num2str(k-IMAGE_MIN+1) ' of ' num2str(IMAGE_MAX-IMAGE_MIN+1) ' iterations']);
end
clear bkgd bin
disp('Peaks have been located');

%%%%%%%%%%%%%%%%%%%%%%%%%%%%%%%%%%%%%%%%%%%%%%%%%%%%%%%%%%%%%%%%%%%
%%% Cleans up binary images
%%%
%%% Runs through images and removes anomalous blips that only last for one
%%% image. Also filters the data with a disk to smooth edges.
%%% Output files are in "cleanest###.tif"
%%%%%%%%%%%%%%%%%%%%%%%%%%%%%%%%%%%%%%%%%%%%%%%%%%%%%%%%%%%%%%%%%%%

for k=IMAGE_MIN+1:IMAGE_MAX-1
    imgprev=imread(imgnumberer('cleaned',k-1,IMAGE_MAX,'.tif'));
    img=imread(imgnumberer('cleaned',k,IMAGE_MAX,'.tif'));
    imgpost=imread(imgnumberer('cleaned',k+1,IMAGE_MAX,'.tif'));
    img=cleaner(imgprev,img,imgpost,XSIZE,YSIZE,DISK_SIZE);
    imwrite(img,imgnumberer('cleanest',k,IMAGE_MAX,'.tif'),'TIF',...
        'WriteMode','OverWrite','compression','none');
    disp([num2str(k-IMAGE_MIN) ' of ' num2str(IMAGE_MAX-IMAGE_MIN-1) ' iterations']);
end
```

```
clear all
disp('Images have been tidied up somewhat');



% % % % % % % % % % % % % % % % % % % % % % % % % % % % % % % % % % % % % % % % % % % % % % % % % %
% % % Coloranalyzer
% % %
% % % This program identifies red spots in a color .tif file. The red, green,
% % % and blue levels are extracted, and the amount of red in a given pixel is
% % % compared to the amount of green and blue. Using this ratio method
% % % prevents white pixels, which have high intensities of all colors, from
% % % being flagged inadvertantly, and prevents dark red pixels from being
% % % lost.
% % %
% % % The output is a black-and-white image with white where red was and black
% % % everywhere else.
% % % % % % % % % % % % % % % % % % % % % % % % % % % % % % % % % % % % % % % % % % % % % % % % % %

init_var

% Size of the images, based on the size of the initial image.
img=imread(imgnumberer('centered',IMAGE_MIN,IMAGE_MAX,'.tif'));
[XSIZE YSIZE junk]=size(img);
clear img junk

for k=IMAGE_MIN:IMAGE_MAX

    img=imread(imgnumberer('centered',k,IMAGE_MAX,'.tif'));
 %    img=imread([IM_PATH num2str(k) '.tiff']);
    imgbw=rgb2gray(img);
    red=img; green=img; blue=img;

    % Separates the original image into the three RGB components
    red(:,:,[2 3])=0;
    green(:,:,[1 3])=0;
    blue(:,:,[1 2])=0;

    % Finds the red-to-green/blue ratios and the product of the two ratios
    rg_ratio=double(red(:,:,1))./double(green(:,:,2));
    rb_ratio=double(red(:,:,1))./double(blue(:,:,3));
    z=rb_ratio.*rg_ratio;
```

```
    % Constructs a binary matrix with 255 for red points and 0 for others
    bin=zeros(XSIZE,YSIZE);
    for x=1:XSIZE
        for y=1:YSIZE
            % Flags a point if it has a high red/green and red/blue ratio.
            % Can add lots of other conditions here as needed
            if z(x,y)>RB_RATIO*RG_RATIO && red(x,y)>75
                bin(x,y)=255;
            end
        end
    end

    imwrite(bin,imgnumberer('redded',k,IMAGE_MAX,'.tif'),'TIF',...
        'WriteMode','OverWrite');
    disp([num2str(k-IMAGE_MIN+1) ' of ' num2str(IMAGE_MAX-IMAGE_MIN+1) ' iterations']);

end

% % % % % % % % % % % % % % % % % % % % % % % % % % % % % % % % % % % % % % % % % % % % % % % % %
% % % Colorcleaner
% % %
% % % Cleans up binary images
% % % Runs through images and removes anomalous pixels that only last for one
% % % image. Also filters the data with a disk to smooth edges.
% % % % % % % % % % % % % % % % % % % % % % % % % % % % % % % % % % % % % % % % % % % % % % % % %

init_var

% Size of the images, based on the size of the initial image.
img=imread(imgnumberer('redded',IMAGE_MIN,IMAGE_MAX,'.tif'));
[XSIZE YSIZE junk]=size(img);
clear img junk
% Output files are in "bin#####.tif"

for k=IMAGE_MIN+1:IMAGE_MAX-1
    imgprev=imread(imgnumberer('redded',k-1,IMAGE_MAX,'.tif'));
    img=imread(imgnumberer('redded',k,IMAGE_MAX,'.tif'));
    imgpost=imread(imgnumberer('redded',k+1,IMAGE_MAX,'.tif'));
    img=cleaner(imgprev,img,imgpost,XSIZE,YSIZE,DISK_SIZE);
    imwrite(img,imgnumberer('redclean',k,IMAGE_MAX,'.tif'),'TIF',...
```

```
        'WriteMode','OverWrite');
    disp([num2str(k-IMAGE_MIN) ' of ' num2str(IMAGE_MAX-IMAGE_MIN-1) ' iterations']);
end
clear all
disp('Images have been tidied up');

%%%%%%%%%%%%%%%%%%%%%%%%%%%%%%%%%%%%%%%%%%%%%%%%%%%%%%%%%%%%%
%%% Redmarker
%%%
%%% Tags pixels with high red/other color intensitiy
%%%%%%%%%%%%%%%%%%%%%%%%%%%%%%%%%%%%%%%%%%%%%%%%%%%%%%%%%%%%%
init_var

for k=IMAGE_MIN+1:IMAGE_MAX-1
    %%% NOTE: IF USER RAN handpicker.m, THEN 'cleanest' IN THE LINE
    %%% BELOW MUST BE CHANGED TO 'picked', OTHERWISE THIS PROGRAM WILL
    %%% IGNORE THE RESULTS OF handpicker.m
    bw=imread(imgnumberer('cleanest',k,IMAGE_MAX,'.tif'));
    red=imread(imgnumberer('redclean',k,IMAGE_MAX,'.tif'));

    % bin contains three values: 0 for no spot, 128 for a spot with no red,
    % and 255 for a red pixel in a spot
    bin=uint8((uint16(bw)+uint16(red))/2);
    mask=bw/255;

    % Flags points adjacent to a valid peak point if their intensity is
    % less than the current point. Will not change points unless mask = 1
    change=true; % used to terminate loop when no changes are made
    while change==true
        change=false;
        for x=2:XSIZE-1
            for y=2:YSIZE-1
                % Only runs if point is valid peak point and has not yet been
                % processed
                if bin(x,y)==255 && mask(x,y)==1
                    % Compares adjacent and diagonal points
                    if bin(x-1,y)<bin(x,y) && mask(x-1,y)==1
                        bin(x-1,y)=255; change=true; end
                    if bin(x+1,y)<bin(x,y) && mask(x+1,y)==1
                        bin(x+1,y)=255; change=true; end
                    if bin(x,y-1)<bin(x,y) && mask(x,y-1)==1
```

```
                    bin(x,y-1)=255; change=true; end
                if bin(x,y+1)<bin(x,y) && mask(x,y+1)==1
                    bin(x,y+1)=255; change=true; end
                if bin(x-1,y-1)<bin(x,y) && mask(x-1,y-1)==1
                    bin(x-1,y-1)=255; change=true; end
                if bin(x+1,y-1)<bin(x,y) && mask(x+1,y-1)==1
                    bin(x+1,y-1)=255; change=true; end
                if bin(x-1,y+1)<bin(x,y) && mask(x-1,y+1)==1
                    bin(x-1,y+1)=255; change=true; end
                if bin(x+1,y+1)<bin(x,y) && mask(x+1,y+1)==1
                    bin(x+1,y+1)=255; change=true; end
                mask(x,y)=0;
            end
        end
    end
end

% Changes values in bin to 0 if there was indeed no spot.
for x=1:XSIZE
    for y=1:YSIZE
        if bw(x,y)==0 && bin(x,y)>0
            bin(x,y)=0;
        end
    end
end

% For color images that don't save properly...
final=zeros(XSIZE,YSIZE,3,'uint8');
for x=1:XSIZE
    for y=1:YSIZE
        if bin(x,y)==128
            final(x,y,1:3)=255;
        elseif bin(x,y)==255
            final(x,y,1)=255;
        end
    end
end

disp([num2str(k-IMAGE_MIN) ' of ' num2str(IMAGE_MAX-IMAGE_MIN-1) ' iterations']);
imwrite(final,imgnumberer('zzz',k,IMAGE_MAX,'.tif'),'TIF',...
    'WriteMode','OverWrite','compression','none');
```

```
    clear final;
end


% Converts white regions that have one red pixel in them entirely to red
% for images BEYOND the current image.
for i=IMAGE_MIN+1:IMAGE_MAX-2
    img=imread(imgnumberer('zzz',i,IMAGE_MAX-1,'.tif'));
    nextimg=rgb2gray(imread(imgnumberer('zzz',i+1,IMAGE_MAX-1,'.tif')));

    % 76 is the value for red when converting a color image into rgb
    for x=1:XSIZE
        for y=1:YSIZE
            if img(x,y)==76 && nextimg(x,y)==255
                nextimg(x,y)=76;
            end
        end
    end

    bin=nextimg;
    mask=bin>0;

    % Flags points adjacent to a valid peak point if their intensity is
    % less than the current point. Will not change points unless mask = 1
    change=true; % used to terminate loop when no changes are made
    while change==true
        change=false;
        for x=2:XSIZE-1
            for y=2:YSIZE-1
                % Only runs if point is valid peak point and has not yet been
                % processed
                if bin(x,y)==76 && mask(x,y)==1
                    % Compares adjacent and diagonal points
                    if bin(x-1,y)==255 && mask(x-1,y)==1
                        bin(x-1,y)=76; change=true; end
                    if bin(x+1,y)==255 && mask(x+1,y)==1
                        bin(x+1,y)=76; change=true; end
                    if bin(x,y-1)==255 && mask(x,y-1)==1
                        bin(x,y-1)=76; change=true; end
                    if bin(x,y+1)==255 && mask(x,y+1)==1
                        bin(x,y+1)=76; change=true; end
```

```
                    if bin(x-1,y-1)==255 && mask(x-1,y-1)==1
                        bin(x-1,y-1)=76; change=true; end
                    if bin(x+1,y-1)==255 && mask(x+1,y-1)==1
                        bin(x+1,y-1)=76; change=true; end
                    if bin(x-1,y+1)==255 && mask(x-1,y+1)==1
                        bin(x-1,y+1)=76; change=true; end
                    if bin(x+1,y+1)==255 && mask(x+1,y+1)==1
                        bin(x+1,y+1)=76; change=true; end
                    mask(x,y)=0;
                end
            end
        end
    end

    imwrite(bin,imgnumberer('zzz',i+1,IMAGE_MAX,'.tif'),'TIF',...
        'WriteMode','OverWrite','compression','none');
    disp(['up ' num2str(i+1)])
end


%Converts white regions that have one red pixel in them entirely to red
%for images BEFORE the current image.
for i=IMAGE_MAX-1:-1:IMAGE_MIN+3
    img=imread(imgnumberer('zzz',i,IMAGE_MAX-1,'.tif'));
    nextimg=imread(imgnumberer('zzz',i-1,IMAGE_MAX-1,'.tif'));

    for x=1:XSIZE
        for y=1:YSIZE
            if img(x,y)==76 && nextimg(x,y)==255
                nextimg(x,y)=76;
            end
        end
    end


    bin=nextimg;
    mask=bin>0;

    % Flags points adjacent to a valid peak point if their intensity is
    % less than the current point. Will not change points unless mask = 1
    change=true; % used to terminate loop when no changes are made
```

```
    while change==true
        change=false;
        for x=2:XSIZE-1
            for y=2:YSIZE-1
                % Only runs if point is valid peak point and has not yet been
                % processed
                if bin(x,y)==76 && mask(x,y)==1
                    % Compares adjacent and diagonal points
                    if bin(x-1,y)==255 && mask(x-1,y)==1
                        bin(x-1,y)=76; change=true; end
                    if bin(x+1,y)==255 && mask(x+1,y)==1
                        bin(x+1,y)=76; change=true; end
                    if bin(x,y-1)==255 && mask(x,y-1)==1
                        bin(x,y-1)=76; change=true; end
                    if bin(x,y+1)==255 && mask(x,y+1)==1
                        bin(x,y+1)=76; change=true; end
                    if bin(x-1,y-1)==255 && mask(x-1,y-1)==1
                        bin(x-1,y-1)=76; change=true; end
                    if bin(x+1,y-1)==255 && mask(x+1,y-1)==1
                        bin(x+1,y-1)=76; change=true; end
                    if bin(x-1,y+1)==255 && mask(x-1,y+1)==1
                        bin(x-1,y+1)=76; change=true; end
                    if bin(x+1,y+1)==255 && mask(x+1,y+1)==1
                        bin(x+1,y+1)=76; change=true; end
                    mask(x,y)=0;
                end
            end
        end
    end

    imwrite(bin,imgnumberer('zzz',i-1,IMAGE_MAX,'.tif'),'TIF',...
        'WriteMode','OverWrite','compression','none');
    disp(['down ' num2str(i-1)])
end


% Converts the bin file into colors and a final binary file.
for k=IMAGE_MIN+1:IMAGE_MAX-1
    img=imread(imgnumberer('zzz',k,IMAGE_MAX,'.tif'));
    finalimg=zeros(XSIZE,YSIZE,3,'uint8');
    finalbin=zeros(XSIZE,YSIZE,'uint8');
```

```
    for x=1:XSIZE
        for y=1:YSIZE
            if img(x,y)==76
                finalbin(x,y)=1;
                finalimg(x,y,1)=255;
            end
        end
    end

    imwrite(finalimg,imgnumberer('finalimg',k,IMAGE_MAX,'.tif'),'TIF',...
        'WriteMode','OverWrite','compression','none');
    imwrite(finalbin,imgnumberer('finalbin',k,IMAGE_MAX,'.tif'),'TIF',...
        'WriteMode','OverWrite','compression','none');
    disp([num2str(k-IMAGE_MIN) ' of ' num2str(IMAGE_MAX-IMAGE_MIN-1) ' iterations']);
end

%%%%%%%%%%%%%%%%%%%%%%%%%%%%%%%%%%%%%%%%%%%%%%%%%%%%%
%%%  Imgnumberer
%%% Extra subroutine necessary file numbering code
%%%%%%%%%%%%%%%%%%%%%%%%%%%%%%%%%%%%%%%%%%%%%%%%%%%%%

function [impath]=imgnumberer(filename,increment,max,filetype)

%IMGNUMBERER    Adds zeros to file names
%   INPUT:
%       filename    file name
%       increment   increment
%       max         maximum possible value
%       filetype    file extension (e.g., '.tif', '.gif')
%
%   OUTPUT:
%       impath      file name, increment, and extension
%
%   This function adds zeros before an increment. For example, if there are
%   500 total images, image 1 will become 001, image 14 will become 014,
%   etc.  This makes images appear in the proper order within a folder.

if increment==0
    zeroamt=floor(log10(max))+1;
    img_num=num2str(10^zeroamt);
```

```
    impath=[filename img_num(2:numel(img_num)) filetype];
else
    zeroamt=floor(log10(max))+1;
    img_num=num2str(10^(zeroamt-ceil(log10(increment)+0.0001)));
    impath=[filename img_num(2:numel(img_num)) num2str(increment) filetype];
end

% % % % % % % % % % % % % % % % % % % % % % % % % % % % % % % % % % % % % % % % % % % % % % % % %
% % %  Offsetter
% % % Extra subroutine necessary image translating code
% % % % % % % % % % % % % % % % % % % % % % % % % % % % % % % % % % % % % % % % % % % % % % % % %

function [z] = offsetter(matA, offset)

%OFFSETTER      Moves an image around by an offset
%   INPUT:
%       matA        matrix with image data
%       offset      Two-component vector with translation information
%                       offset(1) > 0 --> translate right
%                       offset(1) < 0 --> translate left
%                       offset(2) > 0 --> translate down
%                       offset(2) < 0 --> translate up
%
%   OUTPUT:
%       z           matrix with new image data
%
%   OFFSETTER translates an image within a fixed 2D space, deleting the
%   portions that exceed the matrix and adding zeros (black color) to
%   maintain the original dimensions



% Initializations
[width length] = size(matA);
x=offset(1); y=offset(2);

% Performs horizontal translation
if x<0              % Left translation
    x=x*(-1);
    C = cat(2,matA,zeros(width,x));
    tempz = C(1:width,x+1:length+x);
elseif x>0          % Right translation
```

```
    C = cat(2,zeros(width,x),matA);
    tempz = C(1:width,1:length);
else, tempz=matA;   % No translation
end

% Performs vertical translation
if y<0      % Up translation
    y=y*(-1);
    C = [tempz;zeros(y,length)];
    z = C(y:width+y-1,:);
elseif y>0  % Down translation
    C = [zeros(y,length);tempz];
    z = C(1:width,:);
else z=tempz;      % No translation
end

% % % % % % % % % % % % % % % % % % % % % % % % % % % % % % % % % % % % % % % % % % % % % % % % %
% % % END
% % % % % % % % % % % % % % % % % % % % % % % % % % % % % % % % % % % % % % % % % % % % % % % % %
```

APPENDIX C

Femtosecond Laser Multipulse Machinining

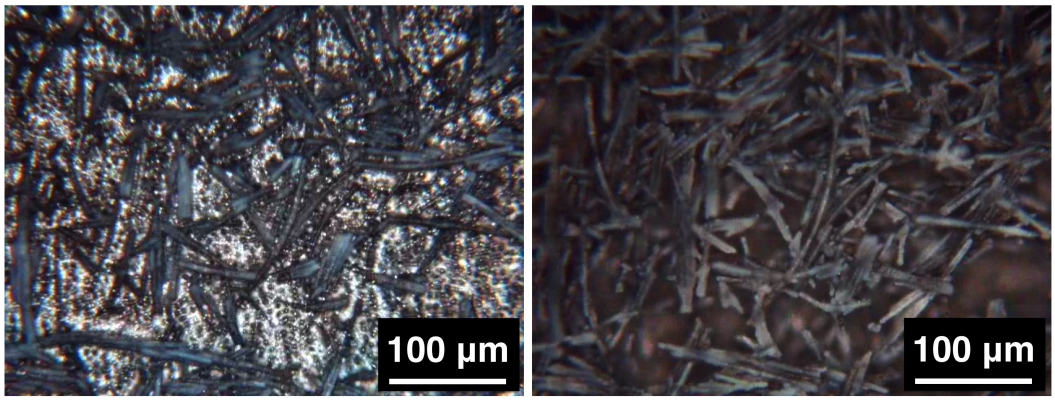

Figure C.**1:** Optical micrograph of laser machined magnesium sample with embedded alumina fibers before substantial ablation (left) and after ablation (right). Preferential ablation of the matrix is shown by the areas that are out of focus. The alumina fibers are exposed and are in focus.

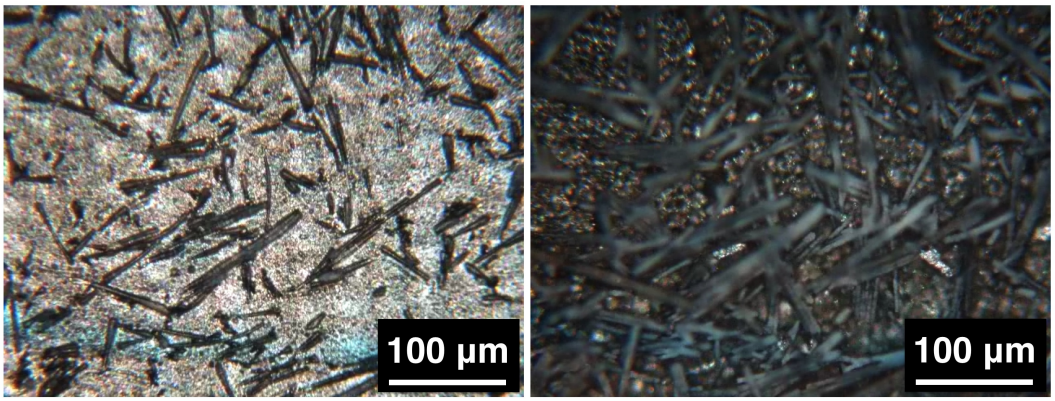

Figure C.**2:** Optical micrograph of laser machined magnesium sample with embedded alumina fibers before substantial ablation (left) and after ablation (right). Preferential ablation of the matrix is shown by the areas that are out of focus. The alumina fibers are exposed and are in focus.

BIBLIOGRAPHY

BIBLIOGRAPHY

[1] M.V. Kral and G. Spanos. Three-dimensional analysis of proeutectoid cementite precipitates. *Acta Materialia*, 47(2):711–724, January 1999.

[2] J. Alkemper and P. W. Voorhees. Quantitative serial sectioning analysis. *Journal of Microscopy*, 201(3):388–394, 2001.

[3] M.D. Uchic, M.A. Groeber, D.M. Dimiduk, and J.P. Simmons. 3D microstructural characterization of nickel superalloys via serial-sectioning using a dual beam FIB-SEM. *Scripta Materialia*, 55(1):23–28, July 2006.

[4] J. Spowart, H. Mullens, and B. Puchala. Collecting and analyzing microstructures in three dimensions: A fully automated approach. *Journal of the Minerals, Metals and Materials Society*, 55:35–37, 2003.

[5] J. Madison, J. Spowart, D.J. Rowenhorst, and T.M. Pollock. The three-dimensional reconstruction of the dendritic structure at the solid-liquid interface of a ni-based single crystal. *Journal of the Minerals, Metals and Materials Society*, 60:26–30, 2008.

[6] S. Hata, K. Kimura, H. Gao, S. Matsumura, M. Doi, T. Moritani, J.S. Barnard, J.R. Tong, J.H. Sharp, and P.A. Midgley. Electron tomography imaging and analysis of and domains in ni-based superalloys. *Advanced Materials*, 20(10):1905–1909, 2008.

[7] W. Treimer, M. Strobl, A. Hilger, C. Seifert, and U. Feye-Treimer. Refraction as imaging signal for computerized (neutron) tomography. *Applied Physics Letters*, 83(2):398–400, July 2003.

[8] A.B. Phillion, S.L. Cockcroft, and P.D. Lee. X-ray micro-tomographic observations of hot tear damage in an Al-Mg commercial alloy. *Scripta Materialia*, 55(5):489–492, September 2006.

[9] P.G. Kotula, M.R. Keenan, and J.R. Michael. Tomographic spectral imaging with multivariate statistical analysis: Comprehensive 3D microanalysis. *Microscopy and Microanalysis*, 12(01):36–48, 2006.

[10] A. Kumar, C.J. Torbet, J.W. Jones, and T.M. Pollock. Nonlinear ultrasonics for in situ damage detection during high frequency fatigue. *Journal of Applied Physics*, 106(2):024904–9, July 2009.

[11] M.N. Shabrov and A. Needleman. An analysis of inclusion morphology effects on void nucleation. *Modelling and Simulation in Materials Science and Engineering*, 10(2):163, 2002.

[12] Y. Huang. The role of nonuniform particle distribution in plastic flow localization. *Mechanics of Materials*, 16(3):265–279, September 1993.

[13] E.E. Underwood. *Quantitative stereology*. Addison-Wesley series in metallurgy and materials. Addison-Wesley Pub. Co., Reading, Mass., 1970.

[14] R.T. Dehoff. Quantitative serial sectioning analysis - preview. *Journal of microscopy*, 131(Sep):259–263, 1983.

[15] Y. Tjiptowidjojo, C. Przybyla, M. Shenoy, and D.L. McDowell. Microstructure-sensitive notch root analysis for dwell fatigue in ni-base superalloys. *International Journal of Fatigue*, 31(3):515–525, March 2009.

[16] P.J. Laz and B.M. Hillberry. Fatigue life prediction from inclusion initiated cracks. *International Journal of Fatigue*, 20(4):263–270, April 1998.

[17] J.G. Cowie, M. Azrin, and G.B. Olson. Microvoid formation during shear deformation of ultrahigh strength steels. *Metallurgical transactions. A, Physical metallurgy and materials science*, 20(1):143–153, 1989.

[18] A.S. Argon, J. Im, and R. Safoglu. Cavity formation from inclusions in ductile fracture. *Metallurgical transactions*, A 6(4):825–837, 1975.

[19] J.C. Russ and R.T. DeHoff. *Practical stereology*. Number v. 1. Kluwer Academic/Plenum, 2000.

[20] C.Y. Hung, G. Spanos, R.O. Rosenberg, and M.V. Kral. Three-dimensional observations of proeutectoid cementite precipitates at short isothermal transformation times. *Acta Materialia*, 50(15):3781 – 3788, 2002.

[21] K. Thornton and H.F. Poulsen. Three-dimensional materials science: An intersection of three-dimensional reconstructions and simulations. *MRS Bulletin*, 33(06):587–595, 2008.

[22] S. Torquato. *Random heterogeneous materials : microstructure and macroscopic properties*. Interdisciplinary applied mathematics. Springer, New York, 2002.

[23] R.T. DeHoff and F.N. Rhines. *Quantitative microscopy*. University of Florida, 1968.

[24] G.A. Mourou, C.P.J. Barty, and M.D. Perry. Ultrahigh-intensity lasers: Physics of the extreme on a tabletop. *Physics Today*, 51(1):22–28, 1998.

[25] C. Walter. Kryder's law. *Scientific American*, 293(2):32–33, 2005.

[26] S. Qidwai, A.B. Geltmacher, A.C. Lewis, D.J. Rowenhorst, and G. Spanos. High-fidelity reconstruction and computational modeling of metallic microstructure. *ASME Conference Proceedings*, 2007(43068):77–86, 2007.

[27] E. Mollick. Establishing moore's law. *Annals of the History of Computing, IEEE*, 28(3):62 –75, july-sept. 2006.

[28] O.F. Forsman. *Undersökning av ett kolstål av hypereutektoid sammansättning.* Meddelande från Stockholks högskolas fysiska insitut. Stockholm, Sweeden, 1918.

[29] L. Holzer, F. Indutnyi, P. Gasser, B. Munch, and M. Wegmann. Three-dimensional analysis of porous BaTiO3 ceramics using FIB nanotomography. *Journal of Microscopy*, 216(1):84–95, 2004.

[30] N. Chawla, V.V. Ganesh, and B. Wunsch. Three-dimensional (3D) microstructure visualization and finite element modeling of the mechanical behavior of SiC particle reinforced aluminum composites. *Scripta Materialia*, 51(2):161–165, 2004.

[31] M. De Graef, M.V. Kral, and M. Hillert. A modern 3-D view of an "Old" pearlite colony. *JOM Journal of the Minerals, Metals and Materials Society*, 58(12):25–28, 2006.

[32] S.G. Lee, A.M. Gokhale, and A. Sreeranganathan. Reconstruction and visualization of complex 3d pore morphologies in a high-pressure die-cast magnesium alloy. *Materials Science and Engineering: A*, 427(1-2):92 – 98, 2006.

[33] P. Li, S. Ghosh, and O. Richmond. An experimental-computational approach to the investigation of damage evolution in discontinuously reinforced aluminum matrix composite. *Acta Materialia*, 47(12):3515–3532, 1999.

[34] J. MacSleyne, M.D. Uchic, J.P. Simmons, and M. De Graef. Three-dimensional analysis of secondary gamma ' precipitates in rene-88 DT and UMF-20 superalloys. *Acta Materialia*, 57(20):6251–6267, 2009.

[35] D.J. Rowenhorst, A. Gupta, C.R. Feng, and G. Spanos. 3D crystallographic and morphological analysis of coarse martensite: Combining EBSD and serial sectioning. *Scripta Materialia*, 55(1):11–16, 2006.

[36] H. Sharma, S.M.C. van Bohemen, R.H. Petrov, and J. Sietsma. Three-dimensional analysis of microstructures in titanium. *Acta Materialia*, 58(7):2399–2407, 2010.

[37] G. Spanos, D.J. Rowenhorst, A.C. Lewis, and A.B. Geltmacher. Combining serial sectioning, EBSD analysis, and image-based finite element modeling. *MRS Bulletin*, 33(6):597–602, 2008.

[38] A. Tewari and A.M. Gokhale. Estimation of three-dimensional grain size distribution from microstructural serial sections. *Materials Characterization*, 46(4):329–335, 2001.

[39] W. Xu, M. Ferry, N. Mateescu, J.M. Cairney, and F.J. Humphreys. Techniques for generating 3-D EBSD microstructures by FIB tomography. *Materials Characterization*, 58(10):961–967, 2007.

[40] B. Gault, F. Vurpillot, A. Vella, M. Gilbert, A. Menand, D. Blavette, and B. Deconihout. Design of a femtosecond laser assisted tomographic atom probe. *Review of Scientific Instruments*, 77(4):043705–8, April 2006.

[41] G. Spanos, A.W. Wilson, and M.V. Kral. New insights into the widmanstatten proeutectoid ferrite transformation: Integration of crystallographic and three-dimensional morphological observations. *Metallurgical and Materials Transactions A*, 36A(5):1209–1218, 2005.

[42] M.A. Groeber, B.K. Haley, M.D. Uchic, D.M. Dimiduk, and S. Ghosh. 3D reconstruction and characterization of polycrystalline microstructures using a FIB-SEM system. *Materials Characterization*, 57(4-5):259–273, 2006.

[43] M. Groeber, B. Haley, M. Uchic, and S. Ghosh. Microstructural characterization using 3-D orientation data collected by an automated FIB-EBSD system. *Materials Processing and Design: Modeling, Simulation and Applications, Pts 1 and 2*, 712:1712–1718, 2004.

[44] G.D. West and R.C. Thomson. Combined EBSD/EDS tomography in a dual-beam FIB/FEG-SEM. *Journal of Microscopy-Oxford*, 233(3):442–450, 2009.

[45] M.D. Uchic. Fib serial sectioning of a ti-modified 4330 steel. AFRL, 2007.

[46] O. Brunke and D.K. Neuber, D.and Lehmann. NanoCT: visualizing of internal 3D-structures with submicrometer resolution. *Materials, Processes, Integration and Reliability in Advanced Interconnects for Micro and Nanoelectronics*, 990:325–331, 338., 2007.

[47] R. Cancedda, A. Cedola, A. Giuliani, V. Komlev, S. Lagomarsino, M. Mastrogiacomo, F. Peyrin, and F. Rustichelli. Bulk and interface investigations of scaffolds and tissue-engineered bones by x-ray microtomography and x-ray microdiffraction. *Biomaterials*, 28(15):2505–2524, 2007.

[48] R.C. Atwood, J.R. Jones, P.D. Lee, and L.L. Hench. Analysis of pore interconnectivity in bioactive glass foams using x-ray microtomography. *Scripta Materialia*, 51(11):1029–1033, 2004.

[49] J.R. Jones, G. Poologasundarampillai, R.C. Atwood, D. Bernard, and P.D. Lee. Non-destructive quantitative 3D analysis for the optimisation of tissue scaffolds. *Biomaterials Biomaterials*, 28(7):1404–1413, 2007.

[50] S. Chan and G.B. Olson. High lanthanum c-61 gear steel properties. Northwestern University, 2009.

[51] D. Fuloria, P.D. Lee, and D. Bernard. Microtomographic characterization of columnar al-cu dendrites for fluid flow and flow stress determination. *Materials Science and Engineering: A*, 494(1-2):3 – 9, 2008. Advances in microstructure-based modeling and characterization of deformation microstructures held at the TMS Annual Meeting 2007, Orlando, Florida.

[52] P. Li, P.D. Lee, T.C. Lindley, D.M. Maijer, G.R. Davis, and J.C. Elliott. X-ray microtomographic characterisation of porosity and its influence on fatigue crack growth. *Advanced Engineering Materials*, 8(6):476–479, 2006.

[53] B.P. Flannery, H.W. Deckman, W.G. Roberge, and K.L. Damico. 3-Dimensional X-Ray microtomography. *Science*, 237(4821):1439–1444, 1987.

[54] N.S. Husseini, D.P. Kumah, J.Z. Yi, C.J. Torbet, D.A. Arms, E.M. Dufresne, T.M. Pollock, J.W. Jones, and R. Clarke. Mapping single-crystal dendritic microstructure and defects in nickel-base superalloys with synchrotron radiation. *Acta Materialia*, 56(17):4715–4723, 2008.

[55] D.J. Jensen, E.M. Lauridsen, L. Margulies, H. F. Poulsen, S. Schmidt, H. O. Srensen, and G.B.M. Vaughan. X-ray microscopy in four dimensions. *Materials Today*, 9(1-2):18–25, 2006.

[56] H. Singh and A.M. Gokhale. Visualization of three-dimensional microstructures. *Materials Characterization*, 54(1):21 – 29, 2005.

[57] A. Tewari and A.M. Gokhale. Application of three-dimensional digital image processing for reconstruction of microstructural volume from serial sections. *Materials Characterization*, 44(3):259–269, 2000.

[58] D. J. Rowenhorst, A. C. Lewis, and G. Spanos. Three-dimensional analysis of grain topology and interface curvature in a beta-titanium alloy. *Acta Materialia*, 58(16):5511–5519, September 2010.

[59] J.G. Cowie, M. Azrin, and G.B. Olson. Shear strain localization in High-Strength steel. *Journal of the Minerals, Metals and Materials Society*, 37(11):A46–A46, 1985.

[60] M. Azrin, J.G. Cowie, and G.B. Olson. High-Strain rate deformation testing of High-Strength steels. *Journal of the Minerals, Metals and Materials Society*, 39(10):A18–A18, 1987.

[61] H. Yamamoto. Conditions for shear localization in the ductile fracture of void-containing materials. *International Journal of Fracture*, 14(4):347–365, 1978.

[62] W.A. Spitzig, R.E. Smelser, and O. Richmond. The evolution of damage and fracture in iron compacts with various initial porosities. *Acta Metallurgica*, 36(5):1201 – 1211, 1988.

[63] M. Saje, J. Pan, and A. Needleman. Void nucleation effects on shear localization in porous plastic solids. *International Journal of Fracture*, 19(3):163–182, 1982.

[64] R.T. Dehoff and V. Howard. Stereology. *Journal of Microscopy*, 138(May):113–113, 1985.

[65] P.G. Winchell and M. Cohen. *The Strength of Martensite*. Defense Technical Information Center, MIT, Cambridge, MA, 1962.

[66] S. Morito, H. Saito, T. Ogawa, T. Furuhara, and T. Maki. Effect of austenite grain size on the morphology and crystallography of lath martensite in low carbon steels. *ISIJ International*, 45(1):91–94, 2005.

[67] C.R. Brooks. *Principles of the heat treatment of plain carbon and low alloy steels*. ASM International, Materials Park, OH, 1996.

[68] R.N. Caron and G. Krauss. Tempering of fe-c lath martensite. *Metallurgical Transactions*, 3(9):2381–&, 1972.

[69] B.L. Bramfitt and S.J. Lawrence. *Metallography and Microstructures of Carbon and Low-Alloy Steels*, volume Vol 9 of *ASM Handbook*. ASM International, 2004.

[70] K.E. Puttick. Ductile fracture in metals. *Philosophical magazine*, 4(44), 1959.

[71] H.C. Rogers. The tensile fracture of ductile metals. *Transactions of the American Institute of Mining and Metallurgical Engineers*, 218(3):498–506, 1960.

[72] T.B. Cox and J.R. Low. Investigation of plastic fracture of alsl-4340 and 18 nickel-200 grae maraging steels. *Metallurgical Transactions*, 5(6):1457–1470, 1974.

[73] A.S. Argon and J. Im. Separation of second-phase particles in spheroidized 1045 steel, cu-0.6pct cr alloy, and maraging-steel in plastic straining. *Metallurgical Transactions*, A 6(4):839–851, 1975.

[74] C.N. Reid, A. Gilbert, and G.T. Hahn. Twinning slip and catastrophic flow in niobium. *Acta Metallurgica*, 14(8):975, 1966.

[75] R.E. Reed-Hill. *Physical metallurgy principles*. PWS-Kent Pub., Boston, 3rd ed. edition, 1992.

[76] A.S. Argon. Formation of cavities from nondeformable second-phase particles in low temperature ductile fracture. *Journal of Engineering Materials and Technology*, 98(1):60–68, 1976.

[77] K.E. Puttick. The shear component of ductile fracture. *Philosophical Magazine*, 5(55):759, 1960.

[78] J.R. Rice and D.M. Tracey. On ductile enlargement of voids in triaxial stress fields. *Journal of the Mechanics and Physics of Solids*, 17(3):201, 1969.

[79] W. Weibull. *The Phenomena of Rupture in Solids*. 1939.

[80] A.L. Schawlow and C.H. Townes. Infrared and optical masers. *Physics Review*, 112(6):1940–1949, 1958.

[81] B. Rethfeld, K. Sokolowski-Tinten, D. von der Linde, and S.I. Anisimov. Timescales in the response of materials to femtosecond laser excitation. *Applied Physics A-Materials Science & Processing*, 79(4-6):767–769, 2004.

[82] J.P. McDonald, S. Ma, T.M. Pollock, S.M. Yalisove, and J.A. Nees. Femtosecond pulsed laser ablation dynamics and ablation morphology of nickel based superalloy CMSX-4. *Journal of Applied Physics*, 103(9):093111–7, 2008.

[83] K. Konig. Multiphoton microscopy in life sciences. *Journal of Microscopy*, 200:83–104, 2000.

[84] J.P. McDonald, D.K. Das, J.A. Nees, T.M. Pollock, and S.M. Yalisove. Approaching non-destructive surface chemical analysis of CMSX-4 superalloy with double-pulsed laser induced breakdown spectroscopy. *Spectrochimica Acta Part B: Atomic Spectroscopy*, 63(5):561–565, May 2008.

[85] S. Nolte, C. Momma, H. Jacobs, A. Tunnermann, B.N. Chichkov, B. Wellegehausen, and H. Welling. Ablation of metals by ultrashort laser pulses. *J. Opt. Soc. Am. B*, 14(10):2716–2722, Oct 1997.

[86] D. Strickland and G. Mourou. Compression of amplified chirped optical pulses. *Optics Communications*, 55(6):447–449, 1985.

[87] http://en.wikipedia.org/wiki/Mode-locking, 2010.

[88] S. Ma, J.P. McDonald, B. Tryon, S.M. Yalisove, and T.M. Pollock. Femtosecond laser ablation regimes in a single-crystal superalloy. *Metallurgical and Materials Transactions A*, 38A(13):2349–2357, 2007.

[89] Y. Hirayama and M. Obara. Heat effects of metals ablated with femtosecond laser pulses. *Apllied Surface Science*, 197:741–745, 2002.

[90] C. Momma, B.N. Chichkov, S. Nolte, F. vonAlvensleben, A. Tunnermann, H. Welling, and B. Wellegehausen. Short-pulse laser ablation of solid targets. *Optics Communications*, 129(1-2):134–142, 1996.

[91] B. Rethfeld and S. Anisimov. On the stability of metal evaporation produced by an ultrashort laser pulse. *Letters to the Jounal of Experimental and Theoretical Physics*, 62(11):872–875, 1995.

[92] S. I. Anisimov, B.l. Kapeliov, and T. L. Perelman. Electron-Emission from surface of metals induced by ultrashort laser pulses. *Jounal of Experimental and Theoretical Physics*, 66(2):776–781, 1974.

[93] L. Jiang and H.L. Tsai. Improved two-temperature model and its application in ultrashort laser heating of metal films. *Journal of Heat Transfer*, 127(10):1167–1173, 2005.

[94] B. Torralva, K. Thornton, and S.M. Yalisove. Femtosecond laser pulse ablation and localized shock melting. 2010.

[95] X. Liu, D. Du, and G. Mourou. Laser ablation and micromachining with ultrashort laser pulses. *Ieee Journal of Quantum Electronics*, 33(10):1706–1716, 1997.

[96] J. Bonse, K.W. Brzezinka, and A.J. Meixner. Modifying single-crystalline silicon by femtosecond laser pulses: an analysis by micro raman spectroscopy, scanning laser microscopy and atomic force microscopy. *Applied Surface Science*, 221(1-4):215–230, 2004.

[97] G.L. Doll, G.L. Eesley, S.D. Brorson, M.S. Dresselhaus, G. Dresselhaus, A. Cassanho, H.P. Jenssen, and D.R. Gabbe. Electron-Phonon relaxation rate in Single-Crystal lanthanum cuprate. *Applied Physics Letters*, 55(4):402–404, 1989.

[98] S.D. Brorson, A. Kazeroonian, J.S. Moodera, D.W. Face, T.K. Cheng, E.P. Ippen, M.S. Dresselhaus, and G. Dresselhaus. Femtosecond Room-Temperature measurement of the Electron-Phonon coupling Constant-Lambda in metallic superconductors. *Physics Review Letters*, 64(18):2172–2175, 1990.

[99] Q. Feng, Y.N. Picard, H. Liu, S.M. Yalisove, G. Mourou, and T.M. Pollock. Femtosecond laser micromachining of a single-crystal superalloy. *Scripta Materialia*, 53(5):511–516, September 2005.

[100] E. Coyne, J.P. Magee, P. Mannion, G.M. O'Connor, and T.J. Glynn. Stem (scanning transmission electron microscopy) analysis of femtosecond laser pulse induced damage to bulk silicon. *Applied Physics A: Materials Science & Processing*, 81(2):371–378, July 2005.

[101] W. Perrie, M. Gill, G. Robinson, P. Fox, and W. O'Neill. Femtosecond laser micro-structuring of aluminium under helium. *Applied Surface Science*, 230(1-4):50–59, May 2004.

[102] J. Bonse, S. Baudach, J. Kruger, W. Kautek, and M. Lenzner. Femtosecond laser ablation of silicon-modification thresholds and morphology. *Applied Physics A-Materials Science & Processing*, 74(1):19–25, 2002.

[103] A. Kumar and T.M. Pollock. Mapping of femtosecond laser-induced collateral damage by electron mapping of femtosecond laser-induced collateral damage by electron mapping of femtosecond laser-induced collateral damage by electron backscatter diffraction. *Journal of Applied Physics*, In Press, 2011.

[104] Q. Feng, Y.N. Picard, J.P. McDonald, P.A. van Rompay, S.M. Yalisove, and T.M. Pollock. Femtosecond laser machining of single-crystal superalloys through thermal barrier coatings. *Materials Science and Engineering: A*, 430(1-2):203–207, 2006.

[105] N. Nedialkov, M. Sawczak, R. Jendrzejewski, P. Atanasov, M. Martin, and G. Sliwinski. Analysis of surface and material modifications caused by laser drilling of aln ceramics. *Applied Surface Science*, 254(4):893 – 897, 2007. Laser synthesis and processing of advanced materials - E-MRS-P Symposium.

[106] Q. Feng, Y.N. Picard, H. Liu, S.M. Yalisove, G. Mourou, and T.M. Pollock. Femtosecond laser micromachining of single-crystal superalloys. In K.A. Green, T.M. Pollock, H. Harada, T.E. Howson, R.C. Reed, J.J. Schirra, and S. Walston, editors, *Superalloys 2004*, pages 687–696, Warrendale, PA, 2004. TMS (The Minerals, Metals & Materials Society), TMS (The Minerals, Metals & Materials Society).

[107] R. Le Harzic, D. Breitling, M. Weikert, S. Sommer, C. Föhl, F. Dausinger, S. Valette, C. Donnet, and E. Audouard. Ablation comparison with low and high energy densities for cu and al with ultra-short laser pulses. *Applied Physics A: Materials Science & Processing*, 80(7):1589–1593, 2005.

[108] I.V. Cravetchi, M.T. Taschuk, Y.Y. Tsui, and R. Fedosejevs. Evaluation of femtosecond LIBS for spectrochemical microanalysis of aluminium alloys. *Analytical & Bioanalytical Chemistry*, 385(2):287–294, June 2006.

[109] D.K. Das, J.P. McDonald, S.M. Yalisove, and T.M. Pollock. Depth-profiling study of a thermal barrier coated superalloy using femtosecond laser-induced breakdown spectroscopy. *Spectrochimica Acta Part B: Atomic Spectroscopy*, 63(1):27–36, January 2008.

[110] S. Pandhija and A. Rai. In situ multielemental monitoring in coral skeleton by CF-LIBS. *Applied Physics B: Lasers and Optics*, 94(3):545–552, March 2009.

[111] T. Höche, D. Ruthe, and T. Petsch. Low-fluence femtosecond-laser interaction with a mo/si multilayer stack. *Applied Physics A: Materials Science & Processing*, 79:961–963, 2004. 10.1007/s00339-004-2583-4.

[112] Y. Jee, M.F. Becker, and R.M. Walser. Laser-induced damage on single-crystal metal surfaces. *J. Opt. Soc. Am. B*, 5(3):648–659, Mar 1988.

[113] X. Zhu. A new method for determining critical pulse width in laser material processing. *Applied Surface Science*, 167(3-4):230 – 242, 2000.

[114] J.P. McDonald. *Near threshold femtosecond laser interactions with materials: Ablation thresholds, morphologies, and dynamics*. PhD thesis, University of Michigan, Applied Physics, Ann Arbor, 2007. PhD.

[115] S.S. Wellershoff, J. Hohlfeld, J. Güdde, and E. Matthias. The role of electron-phonon coupling in femtosecond laser damage of metals. *Applied Physics A: Materials Science & Processing*, 69(7):S99–S107, 1999.

[116] H.K. Tönshoff, C. Momma, A. Ostendorf, S. Nolte, and G. Kamlage. Micro-drilling of metals with ultrashort laser pulses. *LIA*, 12(1):23–27, 2000.

[117] B.N. Chichkov, C. Momma, S. Nolte, vonAlvensleben F., and A. Tunnermann. Femtosecond, picosecond and nanosecond laser ablation of solids. *Applied Physics A-Materials Science & Processing*, 63(2):109–115, 1996.

[118] C. Momma, S. Nolte, B.N. Chichkov, F. vonAlvensleben, and A. Tunnermann. Precise laser ablation with ultrashort pulses. *Applied Surface Science*, 110:15–19, 1997.

[119] P.T. Mannion, J.P. Magee, E Coyne, G.M. O'Connor, and T.J. Glynn. The effect of damage accumulation behaviour on ablation thresholds and damage morphology in ultrafast laser micro-machining of common metals in air. *Applied Surface Science*, 233(1-4):275–287, June 2004.

[120] M. Hashida, M. Fujita, M. Tsukamoto, A.F. Semerok, O. Gobert, G. Petite, Y. Izawa, and J.F. Wagner. Femtosecond laser ablation of metals: precise measurement and analytical model for crater profiles. In *Third International Symposium on Laser Precision Microfabrication*, volume 4830, pages 452–457, Osaka, Japan, 2003. SPIE.

[121] A.A. Serafetinides, M.I. Makropoulou, C.D. Skordoulis, and A.K. Kar. Ultrashort pulsed laser ablation of polymers. *Applied Surface Science*, 180(1-2):42–56, August 2001.

[122] J. Ihlemann, A. Scholl, H. Schmidt, and B. Wolff-Rottke. Nanosecond and femtosecond excimer-laser ablation of oxide ceramics. *Applied Physics A: Materials Science & Processing*, 60(4):411–417, April 1995.

[123] M. Obara, H. Yabe, Y. Hirayama, K. Takahashi, K. Furusawa, F. Barnier, and Y.P. Kim. Functional material processing using intense femtosecond, nanosecond, and microsecond laser ablation. In Claude R. Phipps, editor, *High-Power Laser Ablation III*, volume 4065, pages 210–217, Santa Fe, NM, USA, 2000. SPIE.

[124] J. Bonse, J.M. Wrobel, J. Krüger, and W. Kautek. Ultrashort-pulse laser ablation of indium phosphide in air. *Applied Physics A: Materials Science & Processing*, 72(1):89–94, 2001.

[125] J.M. Liu. Simple technique for measurements of pulsed gaussian-beam spot sizes. *Optics Letters*, 7(5):196–8, May 1982.

[126] N. Yasumaru, K. Miyazaki, and J. Kiuchi. Fluence dependence of femtosecond-laser-induced nanostructure formed on TiN and CrN. *Applied Physics A: Materials Science & Processing*, 81(5):933–937, October 2005.

[127] R. Adams. Seeded region growing. *IEEE Transactions on Pattern Analysis and Machine Intelligence*, 16:641–647, 1994.

[128] B.R. Tull, J.E. Carey, E. Mazur, J.P. McDonald, and S.M. Yalisove. Silicon surface morphologies after femtosecond laser irradiation. *MRS Bulletin*, 31(08):626–633, 2006.

[129] Z Guosheng, P. M. Fauchet, and A. E. Siegman. Growth of spontaneous periodic surface structures on solids during laser illumination. *Phys. Rev. B*, 26(10):5366–5381, Nov 1982.

[130] J.E. Sipe, J.F. Young, J.S. Preston, and H.M. van Driel. Laser-induced periodic surface structure. i. theory. *Phys. Rev. B*, 27(2):1141–1154, Jan 1983.

[131] P. E. Dyer and R. J. Farley. Dynamics of laser-induced periodic surface structures in excimer laser ablation of polymers. *Journal of Applied Physics*, 74(2):1442 –1444, jul 1993.

[132] W.D. Callister. *Materials science and engineering: an introduction*. John Wiley & Sons, 2007.

[133] S. Chan. *Multi-scale Tomographic Analysis of Ductile Fracture in Ultrahigh Strength Steels*. PhD thesis, Northwestern University, Evanston, IL, August 2011.

[134] M.N. Shabrov, C.L. Briant, A. Needleman, S. Kim, E. Sylven, D.H. Sherman, and L. Chuzhoy. Void nucleation by inclusion cracking. *Metallurgical and Materials Transactions A*, 35(6):1745–1755, 2004.

[135] J Gurland. Observations on the fracture of cementite particles in a spheroidized 1.05 *Acta Metallurgica*, 20(5):735 – 741, 1972.

[136] F. Beremin. Cavity formation from inclusions in ductile fracture of a508 steel. *Metallurgical and Materials Transactions A*, 12:723–731, 1981. 10.1007/BF02648336.

[137] T. L Anderson. *Fracture mechanics: fundamentals and applications*. Taylor and Francis, Boca Raton, FL, 3rd ed edition, 2005.

[138] F.J. Vernerey, W.K. Liu, B. Moran, and G.B. Olson. A micromorphic model for the multiple scale failure of heterogeneous materials. *Journal of the Mechanics and Physics of Solids*, 56(4):1320 – 1347, 2008.

[139] D. Broek. *Elementary engineering fracture mechanics*. Martinus Nijhoff, The Hague, 3rd rev. ed edition, 1982.

[140] A. Gangulee and J. Gurland. On fracture of silicon particles in aluminum-silicon alloys. *Transactions of the Metallurgical Society of Aime*, 239(2):269, 1967.

[141] J.A. Psioda. *The effect of microstructure and strength on the fracture toughness of an 18 Ni, 300 grade maraging steel*. PhD thesis, Carnegie Mellon University, Pittsburgh, PA, 1977.

[142] British Steel Corporation. Corporate Laboratories, Iron, and Steel Institute. *Effect of second-phase particles on the mechanical properties of steel: proceedings of a conference organised by the Corporate Laboratories of the British Steel Corporation and the Iron and Steel Institute, held at the Royal Hotel, Scarborough, on 24-25 March 1971*. ISI publication. Iron and Steel Institute, 1971.

[143] T. C Lindley, G Oates, and C. E Richards. A critical of carbide cracking mechanisms in ferride/carbide aggregates. *Acta Metallurgica*, 18(11):1127–1136, 11 1970.

[144] A.S. Argon and J. Im. Separation of second phase particles in spheroidized 1045 steel, cu-0.6pct cr alloy, and maraging steel in plastic straining. *Metallurgical and Materials Transactions A*, 6(4):839–851, 1975.

[145] A.L. Gurson. Continuum theory of ductile rupture by void nucleation and growth .1. yield criteria and flow rules for porous ductile media. *Journal of Engineering Materials and Technology-Transactions of the Asme*, 99(1):2–15, 1977.

[146] F.J. Vernerey, W.K. Liu, B. Moran, and G.B. Olson. Multi-length scale micromorphic process zone model. *Computational Mechanics*, 44(3):433–445, August 2009.

[147] X. Yin, W. Chen, A. To, C. McVeigh, and W.K. Liu. Statistical volume element method for predicting microstructure-constitutive property relations. *Computer Methods in Applied Mechanics and Engineering*, 197(43-44):3516 – 3529, 2008. Stochastic Modeling of Multiscale and Multiphysics Problems.

[148] T. Pardoen and J. W. Hutchinson. Micromechanics-based model for trends in toughness of ductile metals. *Acta Materialia*, 51(1):133–148, 1 2003.

[149] C.J. Butcher and Z.T. Chen. Damage percolation modeling of void nucleation within heterogeneous particle distributions. *Modelling and Simulation in Materials Science and Engineering*, 17(7):075003, 2009.

[150] M.F. Ashby. Work hardening of dispersion-hardened crystals. *Philosophical Magazine*, 14:1157–1178, December 1966.

[151] F.A. McClintock. A criterion for ductile fracture by growth of holes. *Journal of Applied Mechanics*, 35:363–371, 1968.

[152] H. Liebowitz. *Fracture, an advanced treatise*. Number v. 3 in Fracture, an Advanced Treatise. Academic Press, 1971.

[153] J. Embury. Plastic flow in dispersion hardened materials. *Metallurgical and Materials Transactions A*, 16:2191–2200, 1985. 10.1007/BF02670418.

[154] M. Dighe, A. Gokhale, and M. Horstemeyer. Effect of loading condition and stress state on damage evolution of silicon particles in an al-si-mg-base cast alloy. *Metallurgical and Materials Transactions A*, 33:555–565, 2002. 10.1007/s11661-002-0117-2.

[155] G.C. Palmer, I.G. ; Smith. Fracture of internally oxidized copper alloys. volume 47 of *From Second Bolton Landing Conference*, pages 253–290. Met. Soc. Conf.,, Jan 1968.

[156] A.A. Griffith. The phenomena of rupture and flow in solids. *Philosophical Transactions of the Royal Society of London. Series A, Containing Papers of a Mathematical or Physical Character*, 221:163–198, 01 1921.

[157] A. Needleman. A continuum model for void nucleation by inclusion debonding. *Journal of Applied Mechanics*, 54(3):525–531, 1987.

[158] A. Needleman. Void growth in an elastic-plastic medium. *Journal of Applied Mechanics*, 39(4):964–970, 1972.

[159] W.M. Garrison and N.R. Moody. The influence of inclusion spacing and microstructure on the fracture-toughness of the secondary hardening steel af1410. *Metallurgical Transactions A-Physical Metallurgy and Materials Science*, 18(7):1257–1263, July 1987.

[160] N Ohno and J.W. Hutchinson. Plastic-flow localization due to non-uniform void distribution. *Journal of the Mechanics and Physics of Solids*, 32(1):63–85, 1984.

[161] J.R Rice and M.A. Johnson. *Inelastic behavior of solids*, page 641. McGraw-Hill series in materials science and engineering. McGraw-Hill, New York, 1970.

[162] W.M. Garrison Jr. A microstructural interpretation of the fracture strain and characteristics fracture distance. *Scripta Metallurgica*, 18(6):583–586, 6 1984.

[163] W. M. Garrison Jr. A micromechanistic interpretation of the influence of undissolved carbides on the fracture toughness of a low alloy steel. *Scripta Metallurgica*, 20(5):633–636, 5 1986.

[164] V. Tvergaard. On localization in ductile materials containing spherical voids. *International Journal of Fracture*, 18(4):237–252, 1982.

[165] V. Tvergaard. Material failure by void growth to coalescence. *Advances In Applied Mechanics*, 27:83–151, 1990.

[166] V. Tvergaard and J.W. Hutchinson. The relation between crack-growth resistance and fracture process parameters in elastic plastic solids. *Journal of the Mechanics and Physics of Solids*, 40(6):1377–1397, August 1992.

[167] J.W Hutchinson. Finite strain analysis of elastic-plastic solids and structures. In R.F. Hartung, editor, *Numerical Solution of Nonlinear Structural Problems*, volume 6 of *AMD Annual Meeting of ASME*, pages 17–29. ASME, 1973.

[168] J.R. Rice. *Fracture, an advanced treatise*, volume 2, page 191. Academic Press, New York, 1968.

[169] N. Aravas and R.M. McMeeking. Microvoid growth and failure in the ligament between a hole and a blunt crack tip. *International Journal of Fracture*, 29(1):21–38, 1985.

[170] V. Tvergaard and A. Needleman. Analysis of the cup-cone fracture in a round tensile bar. *Acta Metallurgica*, 32(1):157 – 169, 1984.

[171] V. Tvergaard and J.W. Hutchinson. Two mechanisms of ductile fracture: void by void growth versus multiple void interaction. *International Journal of Solids and Structures*, 39(13-14):3581 – 3597, 2002.

[172] D. L. McDowell, K. Gall, M.F. Horstemeyer, and J. Fan. Micro structure-based fatigue modeling of cast A356-T6 alloy. *Engineering Fracture Mechanics*, 70(1):49–80, 2003.

[173] M.F. Horstemeyer and A.M. Gokhale. A void-crack nucleation model for ductile metals. *International Journal of Solids and Structures*, 36(33):5029–5055, November 1999.

[174] F.J. Vernerey, C. McVeigh, W.K. Liu, B. Moran, D. Tewari, D.M. Parks, and G.B. Olson. The 3-d computational modeling of shear-dominated ductile failure in steel. *JOM*, 58(12):45–51, December 2006.

[175] M.P. Echlin, N.S. Husseini, J.A. Nees, and T.M. Pollock. A new femtosecond laser-based tomography technique for multiphase materials. *Advanced Materials*, 23(20):2339–2342, 2011.

[176] S. Hao, W.K. Liu, B. Moran, F. Vernerey, and G.B. Olson. Multi-scale constitutive model and computational framework for the design of ultra-high strength, high toughness steels. *Computer Methods in Applied Mechanics and Engineering*, 193(17-20):1865 – 1908, 2004. Multiple Scale Methods for Nanoscale Mechanics and Materials.

[177] A. Needleman and V. Tvergaard. An analysis of ductile rupture modes at a crack tip. *Journal of the Mechanics and Physics of Solids*, 35(2):151 – 183, 1987.

[178] H.J. Jou. Statistical measurement idl code. 2011.

[179] R. Hill. Elastic properties of reinforced solids: Some theoretical principles. *Journal of the Mechanics and Physics of Solids*, 11(5):357 – 372, 1963.

[180] D.L. McDowell, S. Ghosh, and S.R. Kalidindi. Representation and computational structure-property relations of random media. *JOM Journal of the Minerals, Metals and Materials Society*, 63(3):45–51, march 2011.

[181] M.A. Groeber, S. Ghosh, M.D. Uchic, and D.M. Dimiduk. A framework for automated analysis and simulation of 3d polycrystalline microstructures.: Part 1: Statistical characterization. *Acta Materialia*, 56(6):1257 – 1273, 2008.

[182] M.A. Groeber, S. Ghosh, M.D. Uchic, and D.M. Dimiduk. A framework for automated analysis and simulation of 3d polycrystalline microstructures. part 2: Synthetic structure generation. *Acta Materialia*, 56(6):1274 – 1287, 2008.

[183] M.A. Groeber, M.D. Uchic, D.M. Dimiduk, Y. Bhandari, and S. Ghosh. A framework for automated 3d microstructure analysis & representation. *Journal of Computer-Aided Materials Design*, 14:63–74, 2007.

[184] M. Ostoja-Starzewski. Material spatial randomness: From statistical to representative volume element. *Probabilistic Engineering Mechanics*, 21(2):112 – 132, 2006.

[185] A. Tewari, A.M. Gokhale, J.E. Spowart, and D.B. Miracle. Quantitative characterization of spatial clustering in three-dimensional microstructures using two-point correlation functions. *Acta Materialia*, 52(2):307 – 319, 2004.

[186] T.H. Courtney. *Mechanical Behavior of Materials*. Waveland Press, 2005.

[187] W.M. Garrison Jr. and N.R. Moody. Ductile fracture. *Journal of Physics and Chemistry of Solids*, 48(11):1035 – 1074, 1987.

[188] C. Ruggieri, X. Gao, and R.H. Dodds Jr. Transferability of elastic-plastic fracture toughness using the weibull stress approach: significance of parameter calibration. *Engineering Fracture Mechanics*, 67(2):101 – 117, 2000.

[189] C.S. Wiesner and M.R. Goldthorpe. The effect of temperature and specimen geometry on the parameters of the "local approach" to cleavage fracture ". *Le Journal de Physique IV*, 06(C6):10, 1996.

[190] E.B. Gulsoy, J.P. Simmons, and M. De Graef. Application of joint histogram and mutual information to registration and data fusion problems in serial sectioning microstructure studies. *Scripta Materialia*, 60(6):381 – 384, 2009.

[191] J.I. Goldstein, C.E. Lyman, D.E. Newbury, E. Lifshin, P. Echlin, L. Sawyer, D.C. Joy, and J.R. Michael. *Scanning electron microscopy and x-ray microanalysis*. Springer Science, New York, NY, 3rd ed edition, 2003.

[192] Tetsuo Sakamoto, Zhaohui Cheng, Masanori Takahashi, Masanori Owari, and Yoshimasa Nihei. Development of an ion and electron dual focused beam apparatus for three-dimensional microanalysis. *Japanese Journal of Applied Physics*, 37(Part 1, No. 4A):2051–2056, 1998.

[193] P.P. Pronko, S.K. Dutta, J. Squier, J.V. Rudd, D. Du, and G. Mourou. Machining of sub-micron holes using a femtosecond laser at 800 nm. *Optics Communications*, 114(1-2):106–110, January 1995.

[194] Y. Hirayama and M. Obara. Heat-affected zone and ablation rate of copper ablated with femtosecond laser. *Journal of Applied Physics*, 97(6), 2005.

[195] R.C. Reed. *The superalloys : fundamentals and applications*. Cambridge University Press, Cambridge, UK ; New York, 2006.

[196] T.M. Pollock and A.S. Argon. Creep resistance of cmsx-3 nickel base superalloy single crystals. *Acta Metallurgica et Materialia*, 40(1):1 – 30, 1992.

[197] A.G. Evans, D.R. Mumm, J.W. Hutchinson, G.H. Meier, and F.S. Pettit. Mechanisms controlling the durability of thermal barrier coatings. *Progress in Materials Science*, 46(5):505 – 553, 2001.

[198] H. E. Evans and M. P. Taylor. Diffusion cells and chemical failure of mcraly bond coats in thermal-barrier coating systems. *Oxidation of Metals*, 55:17–34, 2001.

[199] R.W. Jackson, T.M. Pollock, and C Levi. Thermal barrier coating analysis of pt-aluminides bond coats. 2011.

[200] J. Sato, T. Omori, K. Oikawa, I. Ohnuma, R. Kainuma, and K. Ishida. Cobalt-base high-temperature alloys. *Science*, 312(5770):90–91, 2006.

[201] M. Titus. Cobalt-base high-temperature alloy research. June 2011.

[202] J. Wang and A. Misra. An overview of interface-dominated deformation mechanisms in metallic multilayers. *Current Opinion in Solid State and Materials Science*, 15(1):20 – 28, 2011.

[203] A. Misra, M. J. Demkowicz, X. Zhang, and R. G. Hoagland. The radiation damage tolerance of ultra-high strength nanolayered composites. *JOM Journal of the Minerals, Metals and Materials Society*, 59(9):62–65, 2007.

[204] A. Misra, R.G. Hoagland, and H. Kung. Thermal stability of self-supported nanolayered cu/nb films. *Philosophical Magazine*, 84(10):1021–1028, 2004.

[205] T. Nizolek and T.M. Pollock. Cu-nb nanolaminate characterization and fabrication. September 2011.

[206] J.C. Williams. *Titanium Alloys: Processing, Properties, and Applications*. John Wiley & Sons, Ltd, 2010.

[207] C.J. Szczepanski. *The Role of Microstructural Variability on the Very High Cycle Fatigue Lifetime Variability of the + Titanium Alloy, Ti-6Al-2Sn-4Zr-6Mo*. PhD thesis, University of Michigan, Ann Arbor, 2008.